

Spring 2011

Fusion of Visual and Thermal Images Using Genetic Algorithms

Sertan Erkanli
Old Dominion University

Follow this and additional works at: https://digitalcommons.odu.edu/ece_etds



Part of the [Electrical and Computer Engineering Commons](#), and the [Theory and Algorithms Commons](#)

Recommended Citation

Erkanli, Sertan. "Fusion of Visual and Thermal Images Using Genetic Algorithms" (2011). Doctor of Philosophy (PhD), dissertation, Electrical/Computer Engineering, Old Dominion University, DOI: 10.25777/ad8f-5t84
https://digitalcommons.odu.edu/ece_etds/69

This Dissertation is brought to you for free and open access by the Electrical & Computer Engineering at ODU Digital Commons. It has been accepted for inclusion in Electrical & Computer Engineering Theses & Dissertations by an authorized administrator of ODU Digital Commons. For more information, please contact digitalcommons@odu.edu.

**FUSION OF VISUAL AND THERMAL IMAGES
USING GENETIC ALGORITHMS**

by

Sertan Erkanlı

B A August 1995, Turkish Air Force Academy, Turkey

M S August 2003, Turkish Air Force Academy, Turkey

A Dissertation Submitted to the Faculty of
Old Dominion University in Partial Fulfillment of the
Requirement for the Degree of

DOCTOR OF PHILOSOPHY

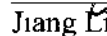
ELECTRICAL AND COMPUTER ENGINEERING

OLD DOMINION UNIVERSITY

May 2011


Approved by

 (Director deceased)

 (Acting Director)

Sacharia Albin (Member)

Yuzhong Shen (Member)

Dimitrie  Popescu (Member)

Volkan Pehlivanoglu (Member)

ABSTRACT

FUSION OF VISUAL AND THERMAL IMAGES USING GENETIC ALGORITHMS

Sertan Erkanlı

Old Dominion University, 2011

Director Dr Zia-ur Rahman (Deceased)

Demands for reliable person identification systems have increased significantly due to highly security risks in our daily life. Recently, person identification systems are built upon the biometrics techniques such as face recognition. Although face recognition systems have reached a certain level of maturity, their accomplishments in practical applications are restricted by some challenges, such as illumination variations. Current visual face recognition systems perform relatively well under controlled illumination conditions while thermal face recognition systems are more advantageous for detecting disguised faces or when there is no illumination control. A hybrid system utilizing both visual and thermal images for face recognition will be beneficial.

The overall goal of this research is to develop computational methods that improve image quality by fusing visual and thermal face images. First, three novel algorithms were proposed to enhance visual face images. In those techniques, specific nonlinear image transfer functions were developed and parameters associated with the functions were determined by image statistics, making the algorithms adaptive. Second, methods were developed for registering the enhanced visual images to their corresponding thermal images. Landmarks in the images were first detected and a subset of those landmarks were selected to compute a transformation matrix for the registration.

Finally, A Genetic algorithm was proposed to fuse the registered visual and thermal images. Experimental results showed that image quality can be significantly improved using the proposed framework.

To my lovely advisor Dr Zia-ur RAHMAN,
I thank you for your guidance and support May you rest in peace

ACKNOWLEDGEMENTS

First of all, I would like to express my sincere condolences on the recent passing of my advisor, Dr Zia-ur Rahman. I am very thankful to Dr Zia-ur Rahman for his sincere willingness to support my work and his guidance throughout my studies that allowed me to develop my skills. I heartily acknowledge his constant encouragements during my research. I benefited greatly from his knowledge and personality. His advice over the years has been of equal importance.

I additionally thank my dissertation advisor Dr Jiang Li for his guidance, encouragement and patience that made the subject study worthwhile.

My sincere acknowledgements to Dr Sacharia Albin, Yuzhong Shen, Dimitrie C Popescu and Volkan Pehlivanoglu for serving on my dissertation committee.

I extend my thanks to Dr Oktay Baysal, Dr Osman Akan and Dr Sefer Kurnaz for initiating the collaborative masters and doctoral programs between the Old Dominion University and the Aeronautics and Space Technologies Institute.

Finally, I want to acknowledge the support of my daughter, Doga, and my wife, Selda, during my stay in Norfolk. Although they are geographically far away, they are close in my mind.

TABLE OF CONTENTS

	Page
LIST OF TABLES	vii
LIST OF FIGURES	viii
Chapter	
1 INTRODUCTION	1
1.1 Research Question and Motivation	2
1.2 Research Objective	3
1.3 Thesis Contribution	3
1.4 Thesis Outline	3
2 LITERATURE SURVEY	4
2.1 Introduction	4
2.2 IR Technology	5
2.3 Non Linear Enhancement Techniques	9
2.4 Registration	23
2.5 Genetic Algorithm	30
2.6 Image Fusion	39
3 ENHANCING POOR VISIBILITY IMAGES	41
3.1 Introduction	41
3.2 Enhancement Technique for Nonuniform and Uniform-Dark Images (ETNUD)	43
3.3 A Wavelet Based Enhancement Technique for Non-Uniform and Uniform-Dark Images (WBNUDE)	54
3.4 Conclusion	64
4 ENTROPY-BASED IMAGE FUSION WITH CONTINUOUS GENETIC ALGORITHM	65
4.1 Introduction	65
4.2 The Techniques of GA and Image Fusion	66
4.3 Evaluation Criteria	70
4.4 Experimental Results	71
4.5 Conclusion	73

	Page
5 EXPERIMENTAL RESULTS	75
5 1 Introduction	75
5 2 IR Images	77
5 3 Enhancement of Visual Images	82
5 4 Harris Corner Detection	87
5 5 IR and Visual Images Registration	88
5 6 Fusion of Two Visual Images	90
5 7 Fusion of Visual and IR Images	96
5 8 Discussion	102
6 CONCLUSIONS AND FUTURE WORK	122
REFERENCES	124
VITA	133

LIST OF TABLES

TABLE	Page
2 1 Registration	31
3 1 The Results of Evaluation Criteria for Figure 3 3	50
3 2 The Results of Evaluation Criteria for Figure 3 4	53
3 3 The Results of Evaluation Criteria for Figure 3 5	54
3 4 The Results of Evaluation Criteria for Figure 3 8	61
3 5 The Results of Evaluation Criteria for Figure 3 9	61
4 1 Performance Comparision of Image Fusion Methods	74
5 1 The Statistics of Figures 5 5-5 8	79
5 2 The Statistics of Figures 5 9 -5 13	80
5 3 The Statistics of Figures 5 26	93
5 4 The Statistics of Figures 5 28	95
5 5 The Statistics of Figures 5 30	97
5 6 The Statistics of Figures 5 32	105
5 7 The Statistics of Figures 5 33	106
5 8 The Statistics of Figures 5 34	107
5 9 The Statistics of Figures 5 35	108
5 10 The Statistics of Figures 5 36	109
5 11 The Statistics of Figures 5 37	110
5 12 The Statistics of Figures 5 38	111
5 13 The Statistics of Figures 5 39	112
5 14 The Statistics of Figures 5 40	113
5 15 The Statistics of Figures 5 41	114
5 16 The Statistics of Figures 5 42	115
5 17 The Statistics of Figures 5 43	116
5 18 The Statistics of Figures 5 44	117
5 19 The Statistics of Figures 5 45	118
5 20 The Statistics of Figures 5 46	119
5 21 The Statistics of Figures 5 47	120
5 22 The Statistics of Figures 5 32 to 5 47	121

LIST OF FIGURES

FIGURE	Page
2 1 Electromagnetic Spectrum Wavelengths	8
2 2 Log Transform	10
2 3 Gamma Transform	12
2 4 Original and Gamma Enhanced Images	13
2 5 Original and Enhanced Image with Retinex	18
2 6 Original and Enhanced Image with AINDANE	20
2 7 Original and Enhanced Image with IRME	25
2 8 Three Steps of Image Registration	27
2 9 Registration	28
2 10 Flowchart of CGA	34
3 1 I_n^{drc} for Different Ranges r_i	45
3 2 I_n^{drc} for Different Ranges r_i	46
3 3 The Results of Enhancement	51
3 4 Comparisons of Enhancement Techniques	52
3 5 Comparisons of Enhancement Techniques	53
3 6 A_n^{drc} for Different Ranges r_i	57
3 7 A_{en}^{drc} for Different Ranges r_i	59
3 8 The Results of Enhancement	62
3 9 Comparisons of Enhancement Techniques	63
4 1 Visual and IR Images	72
4 2 The Result of Fusion	73
4 3 The Result of Continuous Genetic Algorithm	73
4 4 Fusion Results	74
5 1 Database Images	76
5 2 Research Approach Overview	77
5 3 IR Image Statistics	78

FIGURE	Page
5 4 Histogram equalized IR Image Statistics	78
5 5-5 8 IR Images from Different Distances	79
5 9-5 12 IR Images without their Background from Different Distances	80
5 13 The Background	80
5 14 Visual Database Enhancement for Images 1 and 2	83
5 15 Visual Database Enhancement for Images 3 and 4	83
5 16 Visual Database Enhancement for Images 5 and 6	84
5 17 Visual Database Enhancement for Images 7 and 8	84
5 18 Visual Database Enhancement for Images 9 and 10	85
5 19 Visual Database Enhancement for Images 11 and 12	85
5 20 Visual Database Enhancement for Images 13 and 14	86
5 21 Visual Database Enhancement for Images 15 and 16	86
5 22 Diagram of Harris Corner Detection for Registration	87
5 23 The Corners of Visual and IR images	89
5 24 The Corners of Visual and IR images	89
5 25 Visual, IR Image and Combined Image	90
5 26 Fusion Results	92
5 27 The Result of Continuous Genetic Algorithm of Table 5 3	94
5 28 Fusion Results	95
5 29 The Result of Continuous Genetic Algorithm of Table 5 4	95
5 30 Fusion Results	97
5 31 The Result of Continuous Genetic Algorithm of Table 5 5	98
5 32 Fusion Results for image 1	105
5 33 Fusion Results for image 2	106
5 34 Fusion Results for image 3	107
5 35 Fusion Results for image 4	108
5 36 Fusion Results for image 5	109
5 37 Fusion Results for image 6	110
5 38 Fusion Results for image 7	111
5 39 Fusion Results for image 8	112

FIGURE

5 40 Fusion Results for image 9	113
5 41 Fusion Results for image 10	114
5 42 Fusion Results for image 11	115
5 43 Fusion Results for image 12	116
5 44 Fusion Results for image 13	117
5 45 Fusion Results for image 14	118
5 46 Fusion Results for image 15	119
5 47 Fusion Results for image 16	120

1. INTRODUCTION

Biometric technologies such as fingerprint, hand geometry, face and iris recognition are widely used to identify a person's identity. The face recognition system is currently one of the most important biometric technologies, which identifies a person by comparing individually acquired face images with a set of pre-stored face templates in a database.

Though the human perception system can identify faces relatively easily, face reorganization using computer techniques is challenging and remains an active research field. Illumination and pose variations are currently the two obstacles limiting performances of face recognition systems. Various techniques have been proposed to overcome those limitations in recent years. For instance, a three dimensional face recognition system has been investigated to solve the illumination and pose variations simultaneously [1, 2]. The illumination variation problem can also be mitigated by additional sources such as infrared (IR) images [3]. The proposed work in this dissertation will be focusing on fusing optical and infrared images to further improve the image quality for mitigating the illumination challenges.

Thermal face recognition systems have received little attention in comparison with recognition in visible spectra partially due to the high cost associated with IR cameras. Recent technological advances of IR cameras make it practical for face recognition. While thermal face recognition systems are advantageous for detecting disguised faces or when there is no control over illumination, it is challenging to recognize faces in IR images because 1) it is difficult to segment faces from background in low resolution IR images and 2) intensity values in IR images are not consistent due to

the fact that different body temperatures result in different intensity values in IR images. As a remedy, a system is presented for image enhancement by fusing thermal and visual images. The primary objective of this research is to provide improved images, which include more information.

1.1 Research Question and Motivation

The main goal of face recognition is to identify or verify one or more persons in the scene using a stored database of faces. The first step in face recognition is to detect face in images. Face detection systems usually work well for optical images if illumination condition is controlled. However, the performance degrades significantly if the lighting is dim or if it is not uniformly illuminating the scene. Because Thermal IR imagery is invariant to those types of distortions, identifying faces from thermal IR images becomes an active research area. Recent technical advances significantly reduced the cost in the instrumentation of IR cameras, making face recognition based on IR images possible. A combination of visual and thermal face images for face recognition is very promising because it can alleviate the problems caused by the two systems.

Fusing optical and IR images requires an image registration step that aligns one image source to another. The registration step consists of finding a transformation that brings an optical image into the best possible spatial correspondence with its IR counterpart. A common method for registration is to treat it as a mathematical optimization problem, using a similarity measure to quantify the quality of the alignment between the two image sources. A Genetic algorithm is also proposed for fusing the registered images in this dissertation.

1.2 Research Objective

The overall goal of this research is to develop computational methods for obtaining efficiently improved images. The research objective will be accomplished by integrating enhanced visual images with IR Images through the following steps

- 1 Enhance optical images,
- 2 Register the enhanced optical images with IR images,
- 3 Fuse the optical and IR images

1.3. Thesis Contribution

The contribution of this thesis is the development of novel techniques for image enhancement and image fusion as listed below

- 1 Two new algorithms that enhance the uniformity of luminance and image details in optical images,
- 2 A genetic algorithm that fuses the enhanced optical images with IR images

1.4. Thesis Outline

Chapter 2 surveys related work for IR imaging, image enhancement, image registration and image fusion

Chapter 3 discusses the proposed nonlinear image enhancement methods

Chapter 4 presents the proposed image fusion algorithm

Chapter 5 reports the experimental results of the proposed algorithm

Chapter 6 concludes this dissertation

2. LITERATURE SURVEY

2.1 Introduction

The term “biometrics” is derived from the Greek words bio (life) and metric or metry (to measure) and is used to describe technologies that include face, fingerprint, hand geometry, iris, vein and voice recognition systems. Interestingly, the term “biometrics” was not used to describe these technologies until the 1980s, the first reference being in a 1981 article in *The New York Times*. When used for personal identification, biometric technologies measure and analyze human biological and behavioral characteristics. Identifying a person’s biological characteristics is based on direct measurement of a part of the body—fingerprints, hand structure, facial features, iris patterns, and others. The corresponding biometric technologies include fingerprint recognition, hand geometry, facial, and iris recognition, among others. Face recognition systems are currently one of the most important biometric technologies. Facial recognition is used to identify people by comparing sample images with stored templates, using mathematical analysis of the groups of acquired data.

While face recognition techniques have reached a considerable level of maturity, the overall problem still poses a significant challenge due to the large variations in face images of the same person resulting from the impact of changes in illumination and different types of cameras. In this study, we present a new framework for improving the quality of fused images, which takes advantages of both visual and thermal images.

In this chapter, we will present related work in IR Image technology, nonlinear image enhancement algorithms, image registration and image fusion.

2.2 IR Technology

2.2.1 Introduction

Most face detection and recognition research is based on visual images but visual face recognition-based systems perform poorly under poor illumination conditions. An alternative approach for illumination invariant face detection and recognition tasks is to utilize the thermal infrared (IR) imagery.

2.2.2 Theoretical IR Background

Visible light is one of the few types of radiation that can penetrate our atmosphere and be detected on the Earth's surface. Figure 2.1 shows the electromagnetic spectrum ranging from gamma rays, X rays, ultraviolet, visible, infrared, microwaves to radio waves with ascending wavelength and descending frequency. All of these forms of radiation travel at the speed of light (186,000 miles or 300,000,000 meters per second in a vacuum). In addition to visible light, radio, some infrared and very small amount of ultraviolet radiations can also reach the Earth's surface from space. Fortunately, our atmosphere blocks out the rest, much of which is very hazardous, if not deadly, for life on Earth [4].

One type of electromagnetic radiation that has received a lot of attention recently is Infrared (IR) radiation. IR refers to the region beyond the red end of the visible color spectrum, a region located between the visible and the microwave regions of the electromagnetic spectrum [5]. Infrared is usually divided into three spectral regions: short, medium and long-wave infrared, which are listed below.

Short-wave Wavelength between 0.76 to 1.1 microns. The infrared light that we observe in this region is not thermal. Many do not even consider this range as part of

infrared astronomy Beyond about 1.1 microns, infrared emission is primarily heat or thermal radiation

Medium-wave As entering to the medium-wave region of the spectrum, the cool stars begin to fade out and cooler objects such as planets, comets and asteroids come into view Planets absorb light from the sun and heat up They then re-radiate the heat energy as infrared light The emitted infrared light is different from the visible light from planets, which is reflected sunlight The planets in our solar system have temperatures ranging from about 53 to 573 Kelvin degrees Objects in this temperature range emit mostly the medium-wave IR For example, the Earth itself radiates most strongly at about 10 microns wavelength Asteroids also emit most of their light in the medium-wave region making this wavelength band the most efficient for locating dark asteroids Infrared data can help to determine the surface composition and diameters of asteroids

Long-wave In the long-wave region, huge, cold clouds of gas and dust in our galaxy, as well as in nearby galaxies, glow in the long-wave light In some of these clouds, new stars are just beginning to form In the wavelength region, we can detect those protostars long before they 'turn on' visibly by sensing the heat they radiate

2.2.3 Discussion

The primary source of infrared radiation is heat or thermal radiation This is the radiation produced by the motion of atoms and molecules in an object The higher the temperature, the more atoms and molecules move and the more infrared radiation they produce Any object having a temperature above absolute zero (0 degrees Kelvin or 273.15 degrees Celsius) radiates infrared Absolute zero is the temperature at which all atomic and molecular motion ceases Even objects that we think as being very cold, such

as an ice cube, emit infrared. When an object is not quite hot enough to radiate visible light, it will emit most of its energy as infrared. For example, hot charcoal may not give off light but it does emit radiation that we feel as heat. The warmer the object, the more infrared radiation it emits.

Today, infrared technology has many exciting and useful applications. In the field of infrared astronomy, new and fascinating discoveries are being made about the Universe and medical imaging as a diagnostic tool. Infrared cameras are used for police and security as well in fire fighting and in the military. Infrared satellites have been used to monitor the Earth's weather, to study vegetation patterns, and to study geology and ocean temperatures. In addition, Infrared imaging is used to detect heat loss in buildings and in testing electronic system [4].

IR sensors have been applied to face detection in some applications such as night-vision, and military applications. They can detect warm objects. However, IR sensors are much more expensive compared to optical cameras with comparable resolutions, making it less affordable for many applications.

Humans, at normal body temperature, radiate most strongly in the infrared, at a wavelength of about 10 microns [4]. The area of the skin that is directly above a blood vessel is, on average, 0.1 degrees Celsius warmer than the adjacent skin. Moreover, the temperature variation for a typical human face is in the range of about 8 degrees Celsius [7]. Recent improvements in IR-sensors making them be able to capture the temperature variations with a relatively high sensitivity.

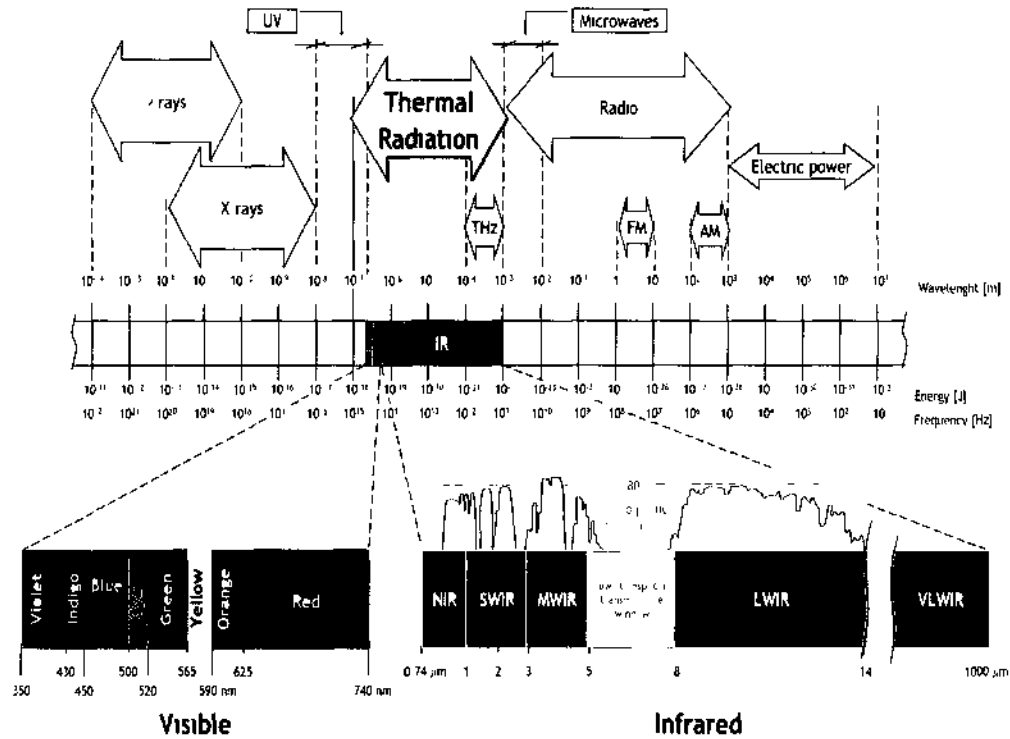


Figure 2.1. Electromagnetic Spectrum Wavelengths [6]

In fact, variations among images from the same face due to changes in illumination, viewing direction, facial expressions, and pose are typically larger than variations introduced when different faces are considered. Thermal IR imagery is invariant to variations introduced by illumination facial expressions since it captures the anatomical information. However, thermal imaging has limitations in identifying a person wearing glasses because glass is a material of low emissivity, or when the thermal characteristics of a face have changed due to increased body temperature (e.g., physical exercise) [8]. Combining the IR and visual techniques will benefit face detection and recognition.

2.3 Nonlinear Image Enhancement Techniques

2.3.1 The Nonlinear Log Transform

The non-linear log transform converts an original image g into an adjusted image g' by applying the log function to each pixel $g[m, n]$ in the image,

$$g'[m, n] = k \log(g[m, n]), \quad (2.1)$$

where $k=L/\log(L)$ is a scaling factor that preserve the dynamic range and L is intensity

The log transform (Fig. 2.2) is typically applied either to dark images where the overall contrast is low, or to images that contain specular reflections or glints. In the former case, the brightening of the dark pixels leads to an overall increase in brightness. In the latter case, the glints are suppressed thus increasing the effective dynamic range of the image.

The log function as defined in equation 2.1 is not parameterized, i.e. it is a single input/output transfer function. A modified parameterized function was proposed by Schreiber in [9] as

$$g'(l) = (L-1) \left[\frac{\log(1 + \alpha g(l)) - \log(\alpha + 1)}{\log(1 + \alpha L) - \log(\alpha + 1)} \right] + 1 \quad (2.2)$$

where, α parameterizes the non-linear transfer function

2.3.2 The Gamma Transform

Most display devices, e.g., monitors, and printers, have a non-linear transfer function. This means that the input and output gray levels are not linearly related,

$$g'[l] \neq ag[l] + b \quad (2.3)$$

where a and b are some constants. The relationship between the input and output gray levels display devices is typically defined as the Gamma transform

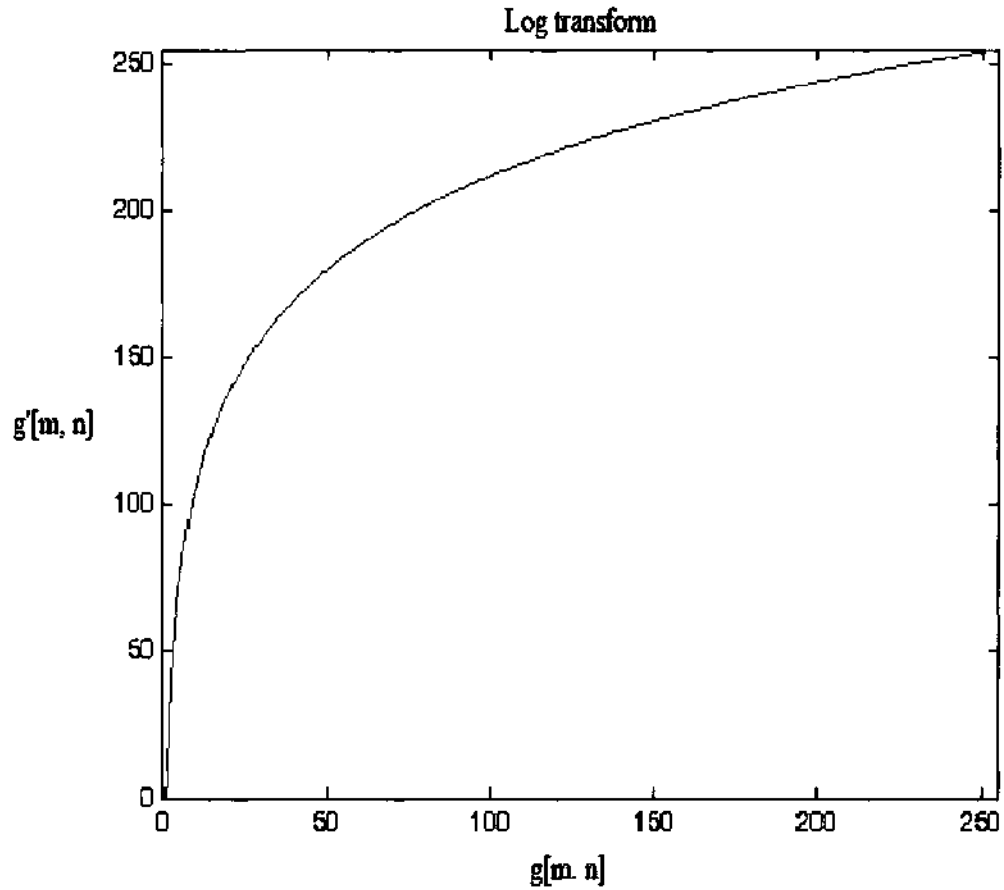


Figure 2.2. Log Transform

$$g'[l] = (L-1) \left(\frac{g(l)}{L-1} \right)^{1/\gamma} \quad (2.4)$$

where the value of γ is display device dependent. Figure 2.3 shows the relationship between input and output gray level distributions for several values of $\gamma = 0.5, 0.75, 1, 1.25, 1.75$ and 2 . As γ increases from 1.0 to 2.0 , the transfer function becomes more and more like the log function. However, the non-linearity at the dark pixels is not as severe as it was in the log function. These values produce supra-linear responses. For values of

$\gamma < 1.0$, the transfer function is sub-linear. The result is to make dark pixels darker. Figure 2.4 shows the enhanced Gamma Image for $\gamma = 2.0$.

2.3.3 The Retinex Theory

The problem of enhancing images automatically is really twofold. In the first instance, all the details in the image need to be preserved, and in the second, all the details need to be made visible. These two problems often require opposing solutions: to preserve all the details, the gray-level distribution needs to be preserved. To enhance the detail in the dark, the dark gray level values need to be boosted. For automatic processing, this is often done with the application of a gray level transformation such as histogram equalization, but the results are often severely disappointing, satisfying neither the first requirement nor the second.

The problem stated above can be thought of as the problem of surrounding the large naturally occurring dynamic range of scenes by limited-dynamic-range digital or film cameras. The range for the former is restricted by the analog-to-digital conversion that occurs when the signal amplitude is quantized and for the latter by the linear region of film response.

A new non-linear image-enhancement technique, Retinex, was developed as a solution to this problem [10, 11]. A retinex employs as much of the structure and function of the retina and cortex as is necessary for producing an image in terms of a correlate of reflectance for a band of wavelengths, an image as nearly independent of flux as is biologically possible. Land's theory is based on computing the product of the ratios between a pixel's values along a set of paths in the image. The first and second

components are the illumination $l(m,n)$ and the reflectance component $r(m,n)$ of an image $I(m,n)$, and [12,13]

The luminance is very hard to distinguish and the latter component can be separated if the former component is known. In this case, if the intensity value at a pixel is divided by its weighted average value, we get [14,15]

$$R_i(m,n) = \frac{I(m,n)}{\bar{I}(m,n)} = \frac{l(m,n)r(m,n)}{\bar{l}(m,n)\bar{r}(m,n)} \quad (2.6)$$

where the bars denote the spatially weighted average value at a pixel. Then for compressing the dynamic range, the logarithm has been applied to each pixel as follows, enlarging low intensity pixel values with respect to higher intensity pixel values [14],

$$R_i(m,n) = \log \left(\frac{I(m,n)}{\bar{I}(m,n)} \right) = \log \left(\frac{l(m,n)r(m,n)}{\bar{l}(m,n)\bar{r}(m,n)} \right) \quad (2.7)$$

$$I(m,n) = l(m,n)r(m,n) \quad (2.5)$$

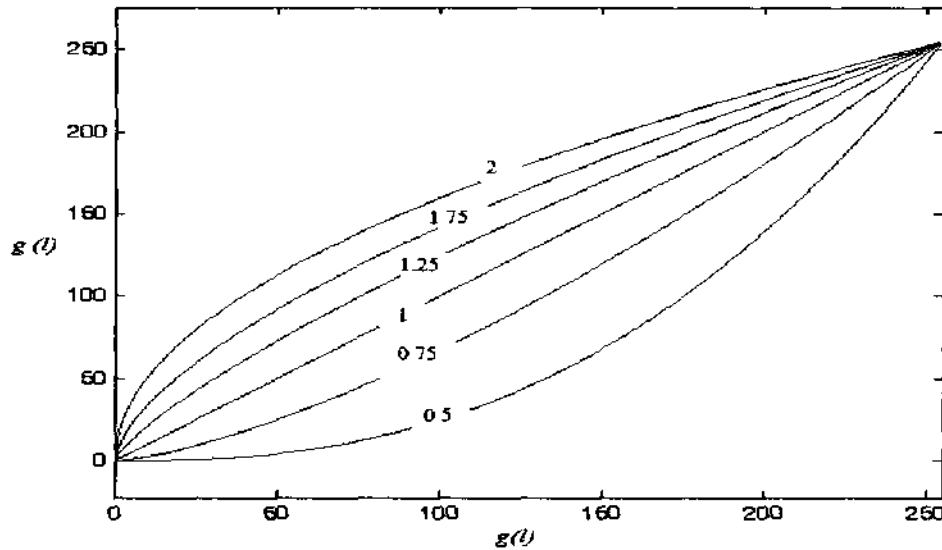


Figure 2.3. Gamma Transform



Figure 2.4. Original and Gamma Enhanced Images Left Image Original Image, Right Image Gamma Transformed Image with $\gamma=2.0$

The general form of the center/surround retinex system models both the receptive fields of individual neurons and perceptual processes. The only extensions required are 1) to greatly enlarge and weaken the surround Gaussian (as determined by its space and amplitude constants) and 2) to include a logarithmic function to make subtractive inhibition into a shunting inhibition. The Gaussian surround form has been chosen as [14]

$$R_i(m,n) = \log I_i(m,n) - \log [F(m,n) * I_i(m,n)] \quad (2.8)$$

where $I_i(m,n)$ is the image distribution in the i th spectral band, “*” represents the convolution and $F(m,n)$ is the surround function. Land proposed an inverse square spatial surround function defined as

$$F(m,n) = \frac{1}{r^2} \quad (2.9)$$

where $r = \sqrt{x^2 + y^2}$ and can be modified to be dependent on a space constant as

$$F(m,n) = \frac{1}{\left(1 + \frac{r^2}{c^2}\right)} \quad (2.10)$$

Hulbert investigated the Gaussian form of the surround function as

$$F(m,n) = \exp\left(-\frac{r^2}{c^2}\right) \quad (2.11)$$

The single scale retinex is defined by the Equation (2.8) and the surround function of SSR is given by [13]

$$F(m,n) = K \exp\left(-\frac{r^2}{c^2}\right) \quad (2.12)$$

c is the Gaussian surround space constant and K is determined such that

$$\iint F(m,n) dx dy = 1 \quad (2.13)$$

The MSR output is then simply a weighted sum of the outputs of several different SSR outputs such that [13]

$$R_{MSR_i} = \sum_{n=1}^N w_n R_{n_i} \quad (2.14)$$

where N is the number of scales, R_{n_i} is the i th spectral component of the MSR output and w_n is the weight associated with the n th scale. The scales have been selected with the help of some experimentation. Experimental results showed that equal weighting $w_n = 1/3$ of the scales was sufficient for most applications.

A new set of design issues emerges for the design of the MSR in addition to those for the SSR [14]. A series of tests are conducted starting with only two scales and adding further scales as needed. It was performed initially with a very small value of scale constant ($c < 15$) and with a very large value of scale constant ($c > 200$) since the small

scale produced good dynamic range compression and fine details at the expense of poorer color rendition while the bigger scale produced high global tonal rendition but at the expense of dynamic range compression. By doing this the choice of an intermediate value $c = 80$ was determined. The three scales produced good dynamic range compression and global tonal rendition [13].

SSR provides dynamic range compression (DRC) and color/lightness constancy. However, SSR can provide either good DRC or good tonal rendition but not both simultaneously. For the conventional 8-bit digital image range, the MSR algorithm performs well in terms of dynamic range compression, but it fails to handle all the images effectively—proposed images possessing notable, and often serious, defects in color rendition. The general effect of retinex processing on images with regional or global gray-world violations is a “graying out” of the image, either globally or in specific regions. This desaturation of color can, in some cases, be severe. More rarely, the gray-world violations can simply produce an unexpected color distortion. Therefore, a color restoration scheme is considered, which called as the Multi-Scale Retinex with Color Restoration (MSRCR), that was developed for providing good color rendition for images that contain gray-world violations. The starting point is analogous to the computation of chromaticity coordinates [13].

$$I_i'(m, n) = \frac{I_i(m, n)}{\sum_{i=1}^S I_i(m, n)} \quad (2.15)$$

For the i th color band, and S is the number of spectral channels. Generally, $S = 3$ of the RGB color space. The modified MSR is mathematically represented as [13].

$$R_{MSRCR_i} = C_i(m, n) R_{MSR_i}(m, n) \quad (2.16)$$

where

$$C_i(m, n) = f[I_i(m, n)] \quad (2.17)$$

is the i th band of the color restoration function (CRF) in the chromaticity space and R_{MSRCR_i} is the i th spectral band of the multiscale retinex with color restoration. The nonlinear color restoration function that provided the best color restoration is defined as [13]

$$C_i(m, n) = \beta \left\{ \log[\alpha I_i(m, n)] - \log \left[\sum_{t=1}^S I_t(m, n) \right] \right\} \quad (2.18)$$

where β is a gain constant and α is a constant that controls the strength of the nonlinearity. The final MSRCR output is obtained by using a “canonical” gain constant and gain/offset adjustment to transition from the logarithmic domain to the display domain. The canonical gain/offset values are independent of spectral channels and image content. The final version of the MSRCR can be written as [13]

$$R_{MSRCR_i} = G[C_i(m, n) \{ \log_i(m, n) - \log[F(m, n) * I_i(m, n)] + b \}] \quad (2.19)$$

where G is the final gain value and b is the final offset value. The chromatics of the original image are used to restore the color which stands in direct contrast to the color constancy objectives of the retinex. It is observed that the stronger the color restoration, the weaker the color constancy, and the MSRCR produces far more visual information and is more “true-to-life” than the unprocessed image as shown in Figure 2.5.

2.3.4 Adaptive and Integrated Neighborhood-Dependent Approach for Nonlinear Enhancement (AINDANE)

There are two parts of AINDANE algorithm, which are adaptive luminance enhancement and adaptive contrast enhancement [16]. In the luminance enhancement

part, intensity values are transformed by a nonlinear transfer function and in the second part image contrast is enhanced based on the local statistics of the image, tuning the intensity of each pixel based on its relative magnitude with respect to the neighboring pixels. First, the color image is converted as follows [16]

$$I(m, n) = (76.245R + 149.685G + 29.07B) / 255 \quad (2.20)$$

where R, G and B are the values of the red, green and blue color band of a pixel

After converting the color image into intensity image, the image intensity is normalized as

$$I_{nor}(m, n) = I(m, n) / 255 \quad (2.21)$$

Then, the dynamic range compression (DRC) has been done with a specially determined nonlinear transfer function for enhancing the dark region in the image [16]

$$I_{nor}(m, n) = \left\{ I_{nor}(m, n)^{(0.75z+0.25)} + (1 - I_{nor}(m, n))^{0.4(1-z)} + I_{nor}(m, n)^{(2-z)} \right\} / 2 \quad (2.22)$$

where z provides the transfer function's curve and is related to the image histogram defined as

$$z = \begin{cases} 0 & \text{for } L \leq 50 \\ (L - 50) / 100 & \text{for } 50 < L \leq 150 \\ 1 & \text{for } L > 150 \end{cases} \quad (2.23)$$

where L is the intensity level corresponding to a cumulative distribution function (CDF) of 0.1. L is used as an indication to determine how dark the 10% of pixels in an image are. If the z value is 0, the pixel will be a maximally enhanced level and if the z value is 1, no pixel will be enhanced.



Figure 2.5. Original and Enhanced Image with Retinex Left Image Original Image, Right Image Enhanced Image with Retinex

Once the darker region has been enhanced, the second part of AINDANE algorithm is applied to achieve sufficient contrast for the image. The luminance information of surrounding pixels is obtained by using the 2D discrete spatial convolution of the image with a Gaussian kernel, where the Gaussian function $G(m,n)$ is defined as

$$G(m,n) = Ke^{\left(\frac{-(m^2+n^2)}{c^2}\right)} \quad (2.24)$$

and K is given by

$$\iint Ke^{\left(\frac{-(m^2+n^2)}{c^2}\right)} dx dy = 1 \quad (2.25)$$

where c is the Gaussian surround space constant. The 2D discrete convolution is carried out on the original intensity image $I(m,n)$ of size $M \times N$ as

$$I_{\text{cov}}(m,n) = \sum_{u=0}^{U-1} \sum_{v=0}^{V-1} I(u,v) G(u+m, v+n) \quad (2.26)$$

Finally, the center-surround contrast enhancement is carried out as defined in the following equation

$$S(m, n) = 255 I_n(m, n)^{E(m, n)} \quad (2.27)$$

The AINDANE algorithm performs the adaptive contrast enhancement by using a power function with a parameter P as

$$E(m, n) = \left[\frac{I_{conv}(m, n)}{I(m, n)} \right]^P \quad (2.28)$$

where the parameter P is related to the global standard deviation of the input intensity image, $I(m, n)$, and can be determined as

$$P = \begin{cases} 3 & \text{for } \sigma \leq 3 \\ (27 - 2\sigma)/7 & \text{for } 3 < \sigma \leq 10 \\ 1 & \text{for } \sigma > 10 \end{cases} \quad (2.29)$$

where σ is the indication of the contrast level of the original intensity image. If σ is less than 3, the image has poor contrast and the contrast of the image will be increased. If σ is more than 10, the image has sufficient contrast and the contrast will not be changed. Finally, the enhanced image as shown in Figure 2.6 can be obtained by a linear color restoration based on chromatic information contained in the original image

$$S_j(m, n) = S(m, n) \frac{I_j(m, n)}{I(m, n)} \lambda_j \quad (2.30)$$

where j represents the RGB spectral band and λ_j is a parameter, which adjusts the color hue

2.3.5 An Illuminance-Reflectance Model for Nonlinear Enhancement of Color Images (IRME)

The IRME algorithm consists of four steps, which are illuminance estimation and reflectance extraction, adaptive dynamic range compression of illuminance, adaptive mid-tone frequency components enhancement and image restoration by combining illuminance and reflectance to recover the intensity image and then performing color recovery [17]

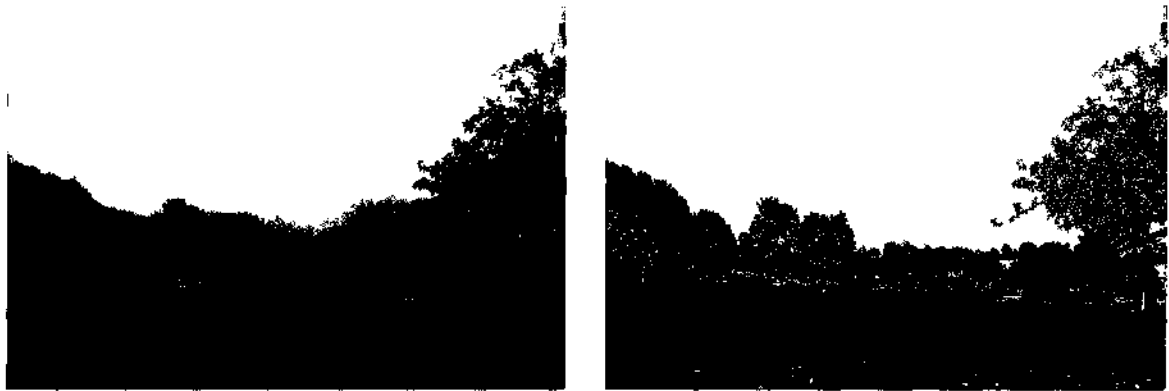


Figure 2.6. Original and Enhanced Image with AINDANE Left Image Original Image, Right Image Enhanced Image with AINDANE

For color images, the intensity image $I(m,n)$ can be obtained using either one of the following two methods

$$I(m,n) = \max[r(m,n), g(m,n), b(m,n)] \quad (2.31)$$

The latter method is used in this algorithm. Then, the image intensity $I(m,n)$ is formulated with following equation

$$I(m, n) = L(m, n)R(m, n) \quad (2.32)$$

where $L(m, n)$ is the illuminance and $R(m, n)$ is the reflectance at each point (m, n) . The luminance is supposed to contain low frequency component and reflectance includes the high frequency component of the image. Afterwards, the illuminance estimation is the low-pass filtered result of intensity image through a Gaussian filter described in Equation 2.24. The 2D discrete convolution is carried out on the original intensity image $I(m, n)$ of size $M \times N$ as

$$L(m, n) = \sum_{u=0}^{U-1} \sum_{v=0}^{V-1} I(u, v)G(u + m, v + n) \quad (2.33)$$

and the illuminance is normalized as

$$L_{nor}(m, n) = L(m, n) / 255 \quad (2.34)$$

It is observed that the determined illumination is composed of not only the real illuminance but also the mid-tone and low-frequency components of reflectance.

Afterwards, the windowed Inverse Sigmoid function is used for enhancing the dark region of the image as

$$f(v) = 1 / (1 + e^{-av}) \quad (2.35)$$

This function can also be used by performing the computational step described by Equation 2.36

$$L_n = L_n[f(v_{max}) - f(v_{min})] + f(v_{min}) \quad (2.36)$$

$$L_n = (1/a) \left((1/L_n) - 1 \right) \quad (2.37)$$

$$L_{enh} = (L_n - v_{min}) / (v_{max} - v_{min}) \quad (2.38)$$

where Equation 2 37 is the inverse sigmoid function and Equation 2 36 is used for linearity mapping normalized illuminance defined in Equation 2 34 to the input range [0 1] Here the sigmoid function can be used to pull down the intensity of the overly lighted pixels The value for v_{\max} is always set to 3 for all images and v_{\min} , depending on the global mean of the intensity image, is defined by

$$v_{\max} = \begin{cases} -6 & \text{for } I_m \leq 70 \\ ((27-70)/80)x3-6 & \text{for } 70 < I_m < 100 \\ -3 & \text{for } I_m \geq 100 \end{cases} \quad (2 39)$$

The above steps will introduce a degradation for dynamic compression because the illuminance includes low frequency and mid tone components To overcome this degradation, a center-surround type of contrast enhancement method is applied as

$$L_{n\text{ enh}}(m,n) = L_{n\text{ enh}}(m,n)^{E(m,n)} \quad (2 40)$$

$$E(m,n) = R(m,n)^P = \left[\frac{I_{\text{conv}}(m,n)}{I(m,n)} \right]^P \quad (2 41)$$

where $L_{n\text{ enh}}(m,n)$ is the illuminance after mid-tone frequencies enhancement and $R(m,n)$ is the ratio of $I(m,n)$ to its low-pass version $I_{\text{conv}}(m,n)$ computed through the same operations as in Equations 2 24, 2 25 and 2 33 P is determined by the global standard deviation of the input intensity image $I(m,n)$ as

$$P = \begin{cases} 2 & \text{for } \sigma \leq 30 \\ -0.03\sigma + 2.9 & \text{for } 30 < \sigma \leq 80 \\ 1/2 & \text{for } \sigma > 80 \end{cases} \quad (2 42)$$

Following the dynamic range compression and contrast enhancement, the final illuminance $L_{n\text{ enh}}(m,n)$ and reflectance R are combined using Equation 2 32 to produce an intensity image I' with compressed dynamic range For color images, a color

restoration process based on the chromatic information of the original image is applied to I' to recover the RGB color as

$$r' = \frac{I'}{I} r \quad g' = \frac{I'}{I} g \quad b' = \frac{I'}{I} b \quad (2.43)$$

such that the color information (hue and saturation) in the original image is preserved in the enhanced image as shown in Figure 2.7

2.4 Registration

2.4.1 Introduction

Image registration is a basic task in image processing to align two or more images, usually refereed as a reference, and a sensed image [18]. Registration is typically a required process in remote sensing [19], medicine [20, 21] and computer vision. Registration can be classified into four main categories according to the manner how the image is obtained [22]

- Different viewpoints: Images of the same scene taken from different viewpoints
- Different times: Images of the same scene taken at different times
- Different sensors: Images of the same scene taken by different sensors
- Scene to model registration: Images of a scene taken by sensors and images of the same scene but from a model (digital elevation model)

It is impossible to implement a comprehensive method useable to all registration tasks and there are many different registration algorithms. The focus is on the feature based registration techniques in the dissertation and they usually consist of the following three steps [22]

- **Feature detection** The step tries to locate a set of control points such as edges, line intersections and corners in the image. They could be manually or automatically detected.
- **Feature matching** The second step is to establish the correspondence between the features detected in the sensed image and those detected in the reference image.
- **Transform model estimation, Image resampling and Geometric transformation** The sensed image is transformed and resampled to match the reference image by proper interpolation techniques [22].

Each registration step has its specific problems. In the first step, features that can be used for registration must spread over the images and be easily detectable. The determined feature sets in the reference and sensed images must have enough common elements, even though the both images do not cover exactly the same scene. Ideally, the algorithm should be able to detect the same features [22].

In the second step, known as feature matching, physically corresponded features can be dissimilar because of the different imaging conditions and/or the different spectral sensitivities of the sensors. The choice of the feature description and measuring of similarity has to take into account of these factors. The feature descriptors should be efficient and invariant to the assumed degradations. The matching algorithm should be robust and efficient. Single features without corresponding counterparts in the other image should not affect its performance [22].

In the last step, the selection of an appropriate resampling technique is restricted by the trade-off between the interpolation accuracy and the computational complexity. In

the literature, there are popular techniques such as the nearest-neighbor and bilinear interpolation [22]



Figure 2.7. Original and Enhanced Image with IRME Left Image Original Image, Right Image Enhanced Image with IRME

2.4.2 The Steps of Image Registration

The three steps of image registration are defined as follows and shown in Figure 2 8 and Figure 2 9

2 4 2 1 Feature detection

An expert selects manually the features in the objects There are two main approaches of feature detection

2 4 2 1 1 Area-based methods

In these approaches, the first step of image registration is omitted because there is no need to detect features [22]

In the second approach, points (region corners, line intersections, points on curves with high curvature), lines (region boundaries, coastlines, roads, rivers) or significant

regions (forests, lakes, and fields) are classified as features. The features should be unique, spread all over the images and efficiently detectable in sensed and reference images. They are expected to be steady in time [22].

2.4.2.2 Feature matching

The detected features in both images can be matched with the help of the image intensity values in their neighborhoods, the feature spatial distribution. Two main approaches to feature matching have been formed [23].

2.4.2.2.1 Area-based methods

2.4.2.2.1.1 Cross-correlation

Without any structural analysis, classical area-based methods like cross-correlation (CC) depend on matching directly image intensities. As a result, they are sensitive to the intensity changes, introduced for example by using different sensor types and/or by noise, varying illumination. This method is based on a statistical similarity. First, the windows pairs are established based on similarity, which is computed for window pairs from both images as follows,

$$CC(i, j) = \frac{\sum_w (W - E(W))(I_{(i, j)} - E(I_{(i, j)}))}{\sqrt{\sum_w (W - E(W))^2} \sqrt{\sum_{I_{(i, j)}} (I_{(i, j)} - E(I_{(i, j)}))^2}} \quad (2.44)$$

Then, equation's maximum is searched and the window pairs for which the maximum is achieved are set as the corresponding ones [22, 23, 24].

2.4.2.2.1.2 Optimization methods

The aim of this method is to find the maximum or minimum of a similarity measure between the reference and sensor images, generally involving the geometrical transformation. Therefore, the problem of registration is converted into a

multidimensional optimization problem where the number of dimensions corresponds to the degrees of freedom of the expected geometrical transformation. The only method for finding global solution is an exhaustive search over the entire image. Although it is computationally demanding, it is often used if only translations are to be estimated [22, 25]

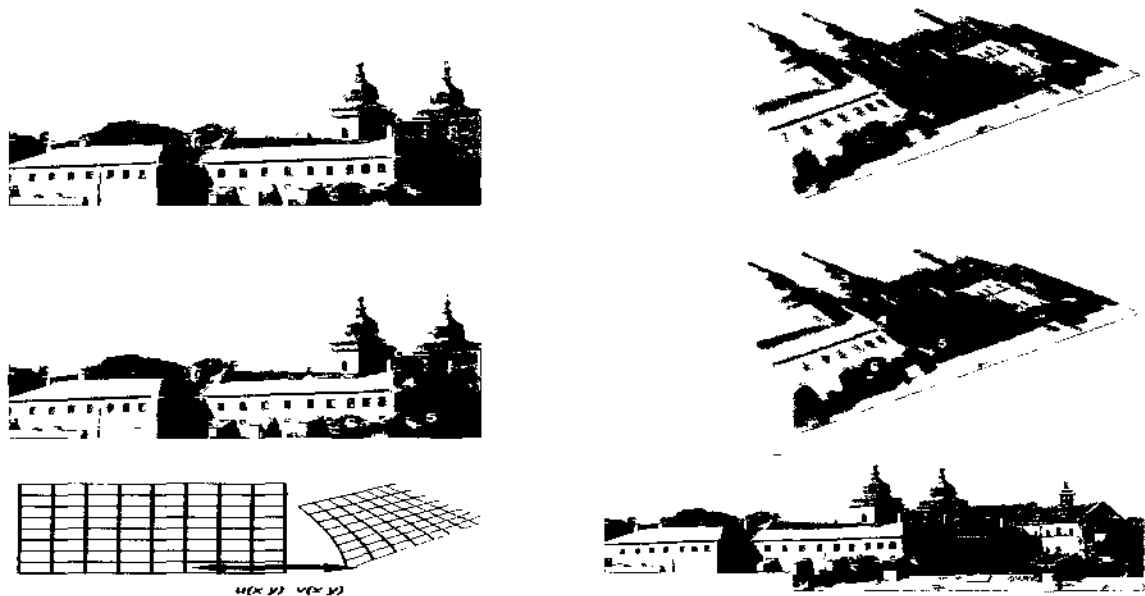


Figure 2.8. Three Steps of Image Registration. Top row—feature detection, Middle row—feature matching by invariant descriptors, Bottom left—transforms model estimation exploiting the established correspondence. Bottom right—image resampling and transformation uses appropriate interpolation technique [22]

2.4.2.2.1.3 Fourier methods

If time is a significant factor and an acceleration of the computational speed is needed, Fourier methods are preferred rather than correlation methods [22, 26]. This step can also be achieved by the feature-based method, which aims to find the correspondence between the two images to be registered [22].

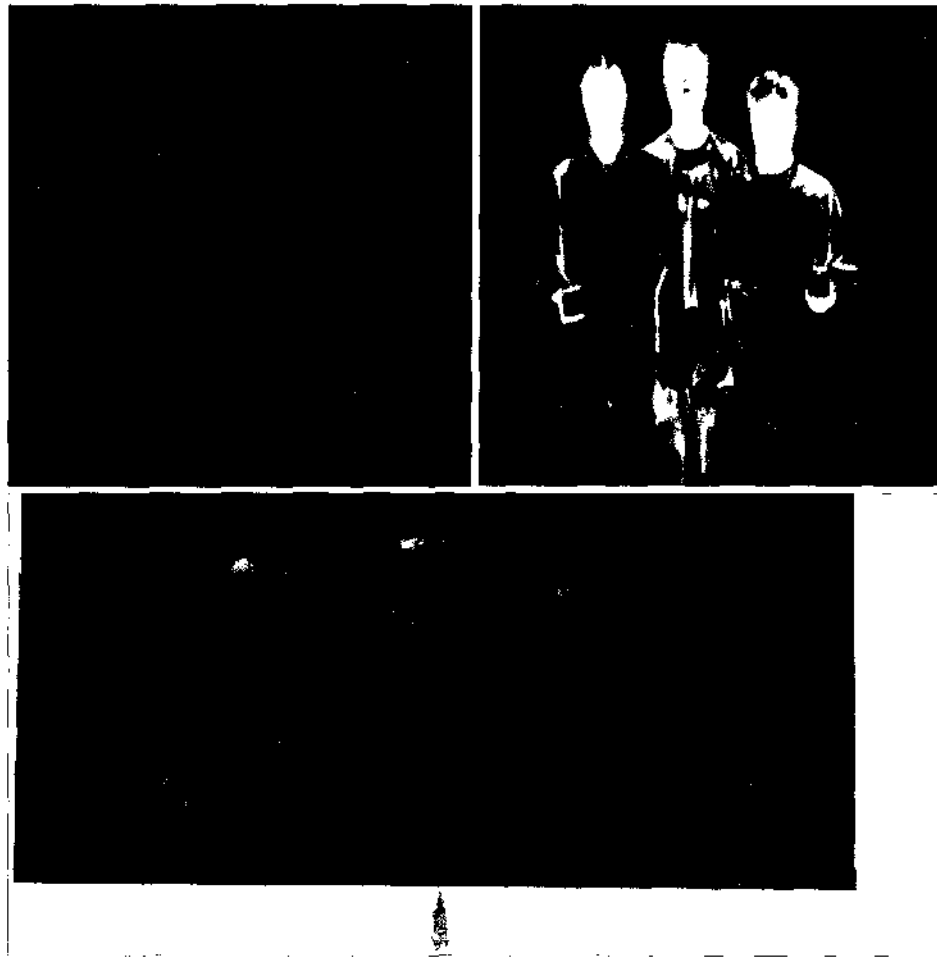


Figure 2.9. Registration top row — Original Visual and IR Images, Second Row — Registered Image

2.4.2.3 Transform Model Estimation, Image Resampling and Geometric Spatial Transformation

After the feature correspondence has been determined, a mapping function is constructed and is used to transform the sensed image to match the reference image. Several useful transformations, including image resizing, rotation, cropping, stretching, shearing, and image projections, could be utilized. There are three interpolation methods

popularly used in image registration and they differ primarily in how many neighbors are considered [18]

The simplest interpolation method is the nearest neighbor method in which the output pixel is assigned the value of the closest pixel in the transformed image. In the bilinear interpolation method, the output pixel is the weighted average of transformed pixels in the nearest 2x2 neighborhood, and in bicubic interpolation, the weighted average is taken over a 4x4 neighborhood [18]

Computational accuracy and complexity increase with the number of pixels under consideration. For most cases, the nearest neighbor interpolation method is sufficient. The method is also the most appropriate for binary images. For RGB and intensity image types, the bilinear or bicubic interpolation method is recommended [18]

Two types of transformation can be defined: the affine transformation and the projective transformation. In affine transformations, straight lines remain straight and parallel lines remain parallel but rectangles may become parallelograms. In projective transformations, straight lines still remain straight but parallel lines often converge toward vanishing points [18]

Suppose an image, f , defined over a (w, z) coordinate system undergoes geometric distortion to produce an image, g , defined over a (x, y) coordinate system, the affine transform can be expressed as

$$(x, y) = T\{(w, z)\} \quad (2.45)$$

or in matrix form as [15]

$$\begin{bmatrix} x & y & 1 \end{bmatrix} = \begin{bmatrix} w & z & 1 \end{bmatrix} T = \begin{bmatrix} w & z & 1 \end{bmatrix} \begin{bmatrix} t_{11} & t_{12} & 0 \\ t_{21} & t_{22} & 0 \\ t_{31} & t_{32} & 1 \end{bmatrix} \quad (2.46)$$

This transformation can scale, rotate, translate, or shear a set of points, depending on the values chosen for the parameters as shown in Table 2.1. The forward mapping functions are [18]

$$\begin{aligned} x &= t_{11}w + t_{21}z + t_{31} \\ y &= t_{12}w + t_{22}z + t_{32} \end{aligned} \quad (2.47)$$

2.5 Genetic Algorithm

2.5.1 Introduction

Optimization can be distinguished by either discrete or continuous variables. Discrete variables have only a finite number of possible values, whereas continuous variables have an infinite number of possible ones. Discrete variable optimization is also known as combinatorial optimization, because the optimum solution consists of a certain combination of variables from the finite pool of all possible variables. However, when trying to find the minimum value of $f(x)$ on a number line, it is more appropriate to view the problem as continuous [27,28,29,30].

Genetic algorithms manipulate a population of potential solutions for the problem to be solved. Usually, each solution is coded as a binary string, equivalent to the genetic material of individuals in nature. Each solution is associated with a *fitness value* that reflects how good it is, compared with other solutions in the population. The higher the fitness value of an individual, the higher its chances of survival and reproduction in the subsequent generation. Recombination of genetic material in genetic algorithms is simulated through a crossover mechanism that exchanges portions between strings.

Table 2.1. Registration

Type	Affine matrix	Coordinate Equations
Identity	$\begin{bmatrix} 1 & 0 & 0 \\ 0 & 1 & 0 \\ 0 & 0 & 1 \end{bmatrix}$	$x = w$ $y = z$
Scaling	$\begin{bmatrix} s_x & 0 & 0 \\ 0 & s_y & 0 \\ 0 & 0 & 1 \end{bmatrix}$	$x = s_x w$ $y = s_y z$
Rotation	$\begin{bmatrix} \cos \theta & \sin \theta & 0 \\ -\sin \theta & \cos \theta & 0 \\ 0 & 0 & 1 \end{bmatrix}$	$x = w \cos \theta - z \sin \theta$ $y = w \sin \theta + z \cos \theta$
Shear(Horizontal)	$\begin{bmatrix} 1 & 0 & 0 \\ \alpha & 1 & 0 \\ 0 & 0 & 1 \end{bmatrix}$	$x = w + \alpha z$ $y = z$
Shear(Vertical)	$\begin{bmatrix} 1 & \beta & 0 \\ 0 & 1 & 0 \\ 0 & 0 & 1 \end{bmatrix}$	$x = w$ $y = \beta w + z$
Translation	$\begin{bmatrix} 1 & 0 & 0 \\ 0 & 1 & 0 \\ \delta_x & \delta_y & 1 \end{bmatrix}$	$x = w + \delta_x$ $y = z + \delta_y$

Another operation, called mutation, causes sporadic and random alteration of the bits in strings. Mutation has a direct analogy in nature and plays the role of regenerating lost genetic material [31]. GAs have found applications in many fields including image processing [32,33,34].

2.5.2 Continuous Genetic Algorithm (CGA):

GAs typically represent solution as binary strings. For many applications, it is more convenient to denote solutions as real numbers known as continuous Genetic algorithms (CGA). CGAs have the advantage of requiring less storage and are faster than the binary counterparts. Figure 2.10 shows the flowchart of simple CGA [35].

2.5.2.1 Components of a Continuous Genetic Algorithm

The various elements in the flowchart are described below [36].

2.5.2.1.1 Cost Function

The goal of GAs is to solve an optimization problem defined as a cost function with a set of parameters involved. In CGA, the parameters are organized as a vector known as a chromosome. If the chromosome has N_{var} variables (an N -dimensional optimization problem) given by $p_1, p_2, p_3, \dots, p_{N_{var}}$, then the chromosome is written as an array with $1 \times N_{var}$ elements as [27]

$$\text{chromosome} = [p_1, p_2, p_3, \dots, p_{N_{var}}] \quad (2.48)$$

In this case, the variable values are represented as floating-point numbers. Each chromosome has a cost found by evaluating the cost function f at the variables

$$p_1, p_2, p_3, \dots, p_{N_{var}},$$

$$\text{cost} = f(\text{chromosome}) = f(p_1, p_2, p_3, \dots, p_{N_{var}}) \quad (2.49)$$

Equations (2.48) and (2.49) along with applicable constraints constitute the problem to be solved. Since the GA is a search technique, it must be limited to exploring a reasonable region of variable space. Sometimes this is done by imposing a constraint on the problem. If one does not know the initial search region, there must be enough diversity in the

initial population to explore a reasonably sized variable space before focusing on the most promising regions

2.5.2.1.2 Initial Population

To begin the CGA process, an initial population of N_{pop} must be defined, a matrix represents the population, with each row being a $1 \times N_{var}$ chromosome of continuous values [36]. Given an initial population of N_{pop} chromosomes, the full matrix of $N_{pop} \times N_{var}$ random values is generated by

$$pop = rand(N_{pop}, N_{var}) \quad (2.50)$$

All variables are normalized to have values between 0 and 1. If the range of values is between p_{lo} and p_{hi} , then the normalized values are given by

$$p = (p_{hi} - p_{lo})p_{norm} + p_{lo} \quad (2.51)$$

where

p_{lo} = highest number in the variable range

p_{hi} = lowest number in the variable range

p_{norm} = normalized value of variable

This society of chromosomes is not a democracy the individual chromosomes are not all created equal. Each one's worth is assessed by the cost function. So at this point, the chromosomes are passed to the cost function for evaluation [35].

2.5.2.1.3 Natural Selection

Now is the time to decide which chromosomes in the initial population are good enough to survive and possibly reproduce offspring in the next generation. As done for the binary version of the algorithm, the N_{pop} costs and associated chromosomes are

ranked from lowest cost to highest cost. This process of natural selection occurs in each iteration to allow the population of chromosomes to evolve. Of the N_{pop} chromosomes in a given generation, only the top N_{keep} are kept for mating and the rest are discarded to make room for the new offspring [35].

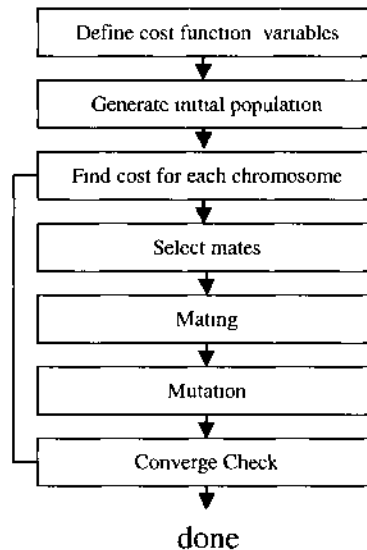


Figure 2.10. Flowchart of CGA

2.5.2.1.4 Pairing

A set of eligible chromosomes is randomly selected as parents to generate next generation. Each pair produces two offspring that contain traits from each parent. The more similar the two parents, the more likely are the offspring to carry the traits of the parents [35].

2.5.2.1.5 Mating

As for the binary algorithm, two parents are chosen to produce offsprings. Many different approaches have been tried for crossing over in continuous GAs. The simplest

method is to mark a crossover points first, then parents exchange their elements between the marked crossover points in the chromosomes. Consider two parents

$$\begin{aligned} parent_1 &= [p_{m1}, \dots, p_{mN}] \\ parent_2 &= [p_{d1}, \dots, p_{dN}] \end{aligned} \quad (2.52)$$

two offspring's might be produced as

$$\begin{aligned} offspring_1 &= [p_{m1}, p_{m2}, p_{d3}, p_{d4}, p_{m5}, p_{m6}, \dots, p_{mN}] \\ offspring_2 &= [p_{d1}, p_{d2}, p_{m3}, p_{m4}, p_{d5}, p_{d6}, \dots, p_{dN}] \end{aligned} \quad (2.53)$$

The extreme case is selecting N_{var} points and randomly choosing which of the two parents will contribute its variable at each position. Thus one goes down the line of the chromosomes and, at each variable, randomly chooses whether or not to swap information between the two parents. This method is called uniform crossover [35]

$$\begin{aligned} offspring_1 &= [p_{m1}, p_{d2}, p_{d3}, p_{d4}, p_{d5}, p_{m6}, \dots, p_{dN}] \\ offspring_2 &= [p_{d1}, p_{m2}, p_{m3}, p_{m4}, p_{m5}, p_{d6}, \dots, p_{mN}] \end{aligned} \quad (2.54)$$

The problem with these point crossover methods is that no new information is introduced. Each continuous value that was randomly initiated in the initial population is propagated to the next generation, only in different combinations. Although this strategy worked fine for binary representations, in case of continuous variables, we are merely interchanging two data points. These approaches totally rely on mutation to introduce new genetic material. The blending methods remedy this problem by finding ways to combine variable values from the two parents into new variable values in the offspring [35]. A single offspring variable value, p_{new} , comes from a combination of the two corresponding offspring variable values

$$p_{new} = \beta p_{mn} + (1 - \beta) p_{dn} \quad (2.55)$$

where

β = random number in the interval $[0, 1]$

p_{mn} = the n th variable in the mother chromosome

p_{dn} = the n th variable in the father chromosome

The same variable of the second offspring is merely the complement of the first (i.e., replacing β by $1 - \beta$). If $\beta = 1$, then p_{mn} propagates in its entirety and p_{dn} dies. In contrast, if $\beta = 0$, then p_{dn} propagates in its entirety and p_{mn} dies. When $\beta = 0.5$, the result is an average of the variables of the two parents. This method is demonstrated to work well on several interesting problems in [35].

Choosing which variables to blend is the next issue to be solved. Sometimes, this linear combination process is done for all variables to the right or to the left of some crossover point. Any number of points can be chosen to blend, up to N_{var} values where all variables are linear combinations of those of the two parents. The variables can be blended by using the same β for each variable or by choosing different β 's for each variable. These blending methods effectively combine the information from the two parents and choose values of the variables between the values bracketed by the parents, however, they do not allow introduction of values beyond the extremes already represented in the population. The simplest way is the linear crossover [35], where three offspring are generated from two parents by

$$\begin{aligned} p_{\text{new}_1} &= 0.5 p_{mn} + 0.5 p_{dn} \\ p_{\text{new}_2} &= 1.5 p_{mn} - 0.5 p_{dn} \\ p_{\text{new}_3} &= -0.5 p_{mn} + 1.5 p_{dn} \end{aligned} \quad (2.56)$$

Any variable outside the bounds is discarded. Then the best two offspring are chosen to propagate. Of course, the factor 0.5 is not the only one that can be used in such

a method Heuristic crossover [35] is a variation where some random number, β , is chosen on the interval $[0, 1]$ and the variables of the offspring are formed by

$$p_{new} = \beta(p_{mn} - p_{dn}) + p_{mn} \quad (2.57)$$

Variations on this theme include choosing any number of variables to modify and generate different β for each variable. This method also allows generations of offspring outside the value ranges of the two parent variables. If this happens, the offspring is discarded and the algorithm tries to use another b . The blend crossover (BLX- α) method [35] begins by choosing some parameters that determine the distance outside the bounds of the two parent variables that the offspring variable may lay. This method allows new values outside of the range of the parents without letting the algorithm stray too far.

The algorithm is a combination of an extrapolation method with a crossover method. The goal was to find a way to closely mimic the advantages of the binary GA mating scheme. It begins by randomly selecting a variable in the first pair of parents to be the crossover point.

$$\alpha = \text{roundup}\{\text{random} * N_{\text{var}}\} \quad (2.58)$$

Let

$$\begin{aligned} \text{parent}_1 &= [p_{m1}, \dots, p_{m\alpha}, \dots, p_{mN_{\text{var}}}] \\ \text{parent}_2 &= [p_{d1}, \dots, p_{d\alpha}, \dots, p_{dN_{\text{var}}}] \end{aligned} \quad (2.59)$$

where the m and d subscripts discriminate between the *mom* and the *dad* parent. Then the selected variables are combined to form new variables that will appear in the children [35]

$$\begin{aligned} p_{new_1} &= p_{m\alpha} - \beta[p_{m\alpha} - p_{d\alpha}] \\ p_{new_2} &= p_{d\alpha} + \beta[p_{m\alpha} - p_{d\alpha}] \end{aligned} \quad (2.60)$$

where β is a random value between 0 and 1. The final step is to complete the crossover with the rest of chromosome

$$\begin{aligned} offspring_1 &= [p_{m1}, p_{m2}, p_{new1}, p_{dN_{ac}}] \\ offspring_2 &= [p_{d1}, p_{d2}, p_{new2}, p_{mN}] \end{aligned} \quad (2.61)$$

where β is also a random value between 0 and 1. The final is to complete the crossover with the rest of the chromosome as before

If the first variable of the chromosomes is selected, then only the variables to the right of the selected variable are swapped. If the last variable of the chromosomes is selected, then only the variables to the left of the selected variable are swapped. This method does not allow offspring variables outside the bounds set by the parent unless $\beta > 1$.

2.5.2.1.6 Mutation

If care is not taken, the GA can converge too quickly into one region on the cost surface. If this area is in the region of the global minimum, there is no problem. However, some functions have many local minima. To avoid overly fast convergence, other areas on the cost surface must be explored by randomly introducing changes, or mutations, in some of the variables. Random numbers are used to select the row and columns of the variables that are to be mutated [35].

2.5.2.1.7 Next Generation

After all these steps, the chromosomes in the starting population are ranked and the bottom ranked chromosomes are replaced by offspring from the top ranked parents to produce the next generation. Some random variables are selected for mutation from the

bottom ranked chromosomes. The chromosomes are then ranked from lowest cost to highest cost. The process is iterated until a global solution is achieved.

2.6 Image Fusion

In last decades, the rapid developments of image sensing technologies make multisensory systems popular in many applications. Researchers have begun to work on the fields of these systems such as medical imaging, remote sensing and the military applications [36, 37, 38, 39]. The outcome of using these techniques is a great increase of the amount of diversity data available. Multi-sensor image data often present complementary information about the region surveyed so that image fusion provides an effective method to enable comparison and analysis of such data [40]. Image fusion is defined as the process of combining information in two or more images of a scene to enhance viewing or understanding of the scene. The fusion process must preserve all relevant information in the fused image [41, 42].

Image fusion can be done at pixel, feature and decision levels [43]. Out of these, the pixel level fusion method is the simplest technique, where average/weighted averages of individual pixel intensities are taken to construct a fused image [44, 45]. Despite their simplicity, these methods are not used nowadays because of some serious disadvantages they possess. For instance, the contrast of the fused information is reduced and also redundant information is introduced in the fused image, which may mask the useful information. These disadvantages are overcome by feature level and decision level fusion methods. Feature and decision level fusion methods are based on human vision system. Decision level fusion combines the results from multiple algorithms to yield a final fused image. Several pyramid transform methods for feature level fusion have been

suggested [45]. Recently, developed methods based on the wavelet transform become popular [45]. In the method source images are decomposed into subimages of different resolutions and in each subimage different features become prominent. To fuse the original source images, the corresponding subimages of different source images are combined based on some criteria to form composite subimages. Inverse pyramid transform of composite transform gives the final fused image.

3. ENHANCING POOR VISIBILITY IMAGES

3.1 Introduction

The human visual system (HVS) allows individuals to assimilate information from their environment. The act of seeing starts when the lens of the eye focuses an image of its surroundings onto a light-sensitive membrane in the back of the eye, called the retina. All vertebrate retina contain at least two types of photoreceptors—rods and cones. Rods are generally used for low-light vision and cones for daylight and color vision. The photoreceptive cells of the retina produce neural impulses in response to photons. These signals are processed in a hierarchical fashion by different parts of the brain for further processing and visual perception [46,47].

The HVS perceives colors and detail across a wide range of photometric intensity levels much better than electronic cameras. The perceived color of an object, additionally, is almost independent of the type of illumination, i.e., the HVS is color constant. Electronic cameras suffer, by comparison, from limited dynamic range and the lack of color constancy and current imaging and display devices such as CRT monitors and printers have limited dynamic range of about two orders of magnitude, while the best photographic prints can provide contrast up to $10^3:1$. However, real world scenes can have a dynamic range of six orders of magnitude [48,49]. This can result in overexposure that causes saturation in high contrast images, or underexposure in dark images [50,51,52,53]. The idea behind enhancement techniques are to bring out details in images that are otherwise too dim to be perceived either due to insufficient brightness or insufficient contrast [54,55,56]. A large number of image enhancement methods have been developed, like log transformations, power law transformations, piecewise-linear

transformations and histogram equalization. However, these enhancement techniques are based on global processing which results in a single mapping between the input and the output intensity space. These techniques are thus not sufficiently powerful to handle images that have both very bright and very dark regions. Other image enhancement techniques are local in nature, i.e., the output value depends not only on the input pixel value but also on pixel values in the neighborhood of the pixel. These techniques are able to improve local contrast under various illumination conditions.

Single-Scale Retinex (SSR) [50,57], is a modification of the Retinex algorithm introduced by Edwin Land [58,59]. It provides dynamic range compression (DRC), color constancy, and tonal rendition. SSR gives good results for DRC or tonal rendition but does not provide both simultaneously [54]. Therefore, the Multi-Scale Retinex (MSR) was developed by Rahman et al. [52,54]. The MSR combines several SSR outputs with different scale constants to produce a single output image, which has good DRC, color constancy and good tonal rendition. The outputs of MSR display most of the detail in the dark pixels but at the cost of enhancing the noise in these pixels and the tonal rendition is poor in large regions of slowly changing intensity. As a result, Multi-Scale Retinex with Color Restoration (MSRCR) was developed by Jobson et al. [54], for synthesizing local contrast improvement, color constancy and lightness/color rendition. Other non-linear enhancement models include the Illuminance Reflectance Model for Enhancement (IRME) proposed by Tao et al. [51], and the Adaptive and Integrated Neighborhood-Dependent Approach for Nonlinear Enhancement (AINDANE) described by Tao [60]. Both use a nonlinear function for luminance enhancement and tune the intensity of each pixel based on its relative magnitude with respect to the neighboring pixels.

In this section, a two new image enhancement approach is described Enhancement Technique for Nonuniform and Uniform-Dark Images (ETNUD) and a Wavelet Based Enhancement Technique for Non-Uniform and Uniform-Dark Images (WBNUDE) The details of the new algorithms are given in Section 3.2 and in Section 3.3, respectively Sections 3.2 and 3.3 describe experimental results and compare our results with other techniques for image enhancement Finally in Section 3.4, conclusions are presented

3.2 Enhancement Technique for Nonuniform and Uniform-Dark Images (ETNUD)

The major innovation in ETNUD is in the selection of the transformation parameters for DRC, and the surround scale and color restoration parameters The following sections describe the selection mechanisms

3.2.1 Selection of transformation parameters for DRC

The intensity I of the color image I_c can be determined by

$$I(m,n)=0.2989r(m,n)+0.587g(m,n)+0.114b(m,n) \quad (3.1)$$

where r , g , b are the red, green, and blue components of I_c respectively, and m and n are the row and column pixel locations respectively Assuming I to be 8-bits per pixel, I_n is the normalized version of I , such that

$$I_n(m,n) = I(m,n) / 255 \quad (3.2)$$

Using linear input-output intensity relationships typically does not produce a good visual representation compared with direct viewing of the scene [54] Therefore, nonlinear transformation for DRC is used, which is based on some information extracted from the image histogram To do this, the histogram of the intensity images is subdivided into four ranges

$r_1 = 0-63$, $r_2 = 64-127$, $r_3 = 128-191$ and $r_4 = 192-255$ I_n is mapped to I_n^{drc} using the following

$$I_n^{drc} = \begin{cases} (I_n)^x + \alpha & 0 < x < 1 \\ (0.5 + (0.5 I_n)^x) + \alpha & x \geq 1 \end{cases} \quad (3.3)$$

The first mapping pulls out the details in the dark regions, and the second suppresses the bright overshoots. The value of x is given by

$$x = \begin{cases} 0.2, & \text{if } (f(r_1 + r_2) \geq f(r_3 + r_4)) \wedge (f(r_1) \geq f(r_2)) \\ 0.5, & \text{if } (f(r_1 + r_2) \geq f(r_3 + r_4)) \wedge (f(r_1) < f(r_2)) \\ 3.0, & \text{if } (f(r_1 + r_2) < f(r_3 + r_4)) \wedge (f(r_1) \geq f(r_4)) \\ 5.0, & \text{if } (f(r_1 + r_2) < f(r_3 + r_4)) \wedge (f(r_1) < f(r_4)) \end{cases} \quad (3.4)$$

where $f(a)$ refers to number of pixels between the range (a) , $f(a_1 + a_2) = f(a_1) + f(a_2)$, and \wedge is the logical AND operator. α is the offset parameter, helping to adjust the brightness of image. The curves for the two ranges of x are shown in Figures 3.1 and 3.2. The determination of the x values and their association with the range-relationships as given in Equation 3.4 was done experimentally using a large number of non-uniform and uniform dark images and x value can be also determined manually.

The DRC mapping of the intensity image performs a visually dramatic transformation. However, it tends to have poor contrast, so a local, pixel dependent contrast enhancement method is used to improve the contrast.

3.2.2 Selection of surround parameter and color restoration

Many local enhancement methods rely on center/surround ratios [50], [60]. Hurlbert [61] investigated the Gaussian as the optimal surround function. Other surround functions proposed by Land [59] were compared with the performance of the Gaussian proposed by Jobson et al. [50]. Both investigations determined that the Gaussian form

produced good dynamic range compression over a range of space constants. Therefore, the luminance information of surrounding pixels is obtained by using 2D discrete spatial convolution with a Gaussian kernel, $G(m, n)$ defined as

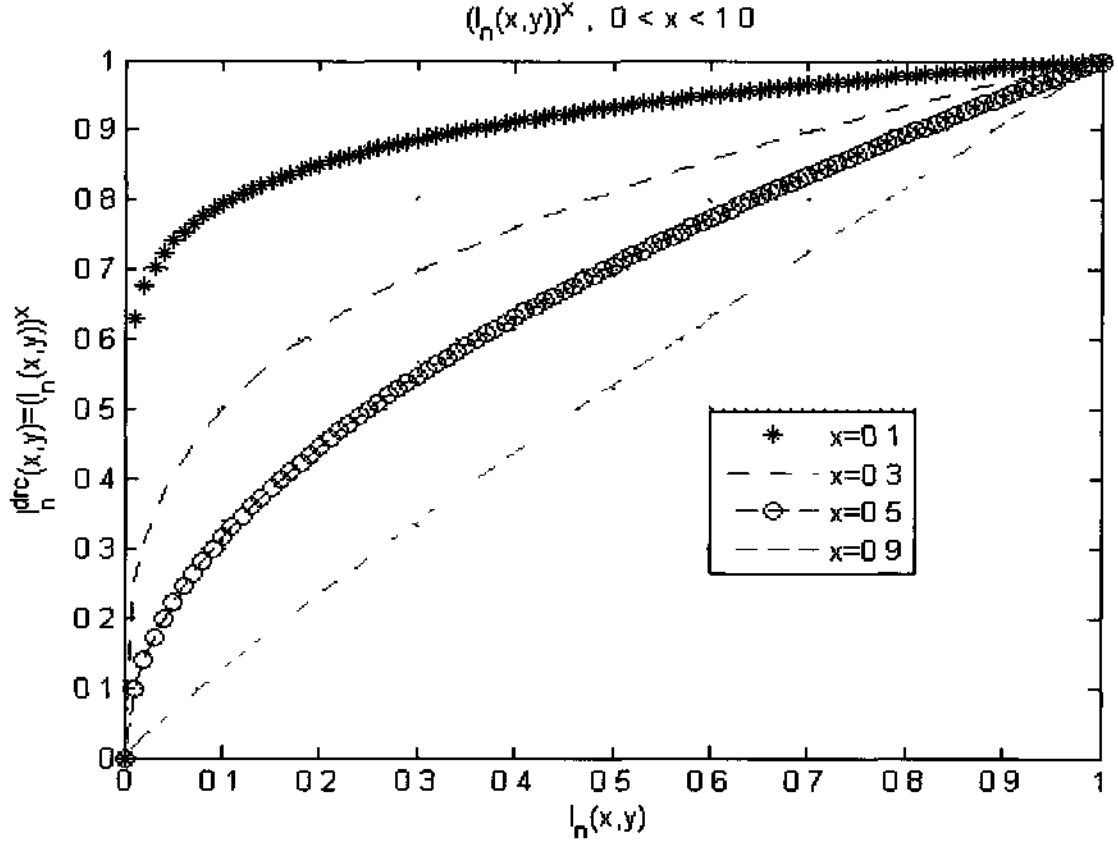


Figure 3.1. I_n^{drc} for Different Ranges r_i

$$G(m, n) = K \exp\left(-\frac{m^2 + n^2}{\sigma_s^2}\right) \quad (3.5)$$

where σ_s is the surround space constant equal to the standard deviation of $G(m, n)$, and

K is determined under the constraint that $\sum_{m, n} G(m, n) = 1$

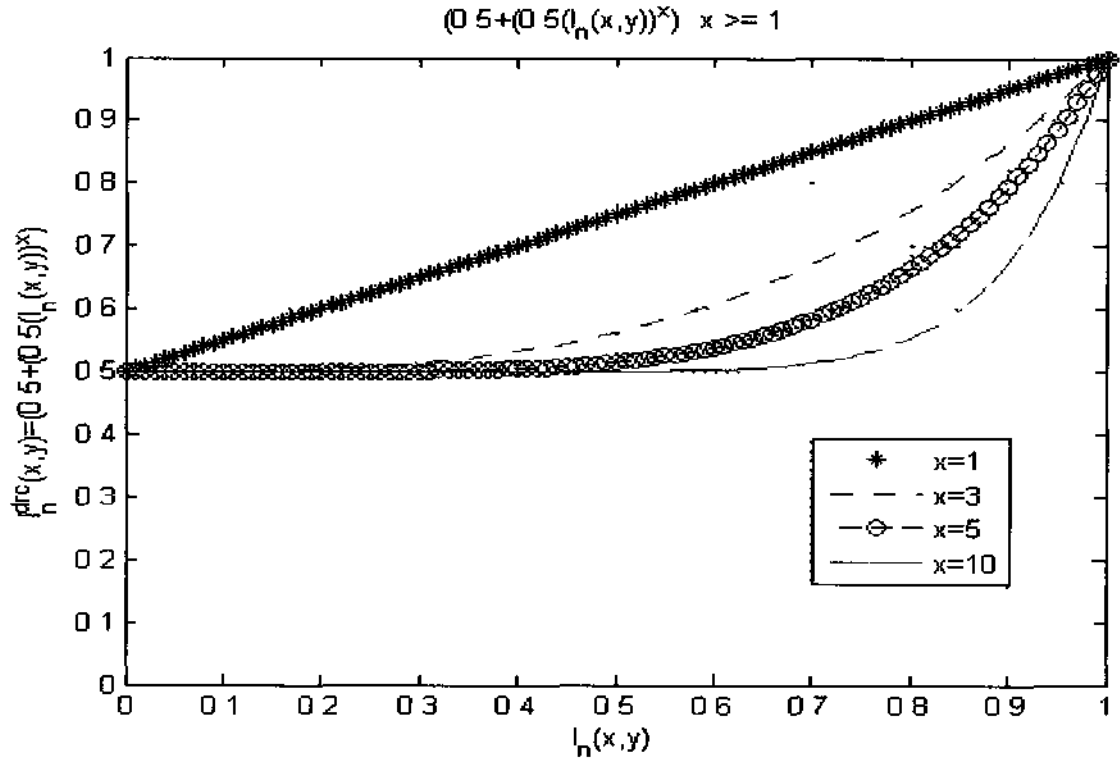


Figure 3.2. I_n^{drc} for Different Ranges r_t

The center-surround contrast enhancement is defined as

$$I_{enh}(m, n) = 255(I_n^{drc}(m, n))^{E(m, n)} \quad (3.6)$$

where, $E(m, n)$ is given by

$$E(m, n) = \left[\frac{I_{filt}(m, n)}{I(m, n)} \right]^S \quad (3.7)$$

where,

$$I_{filt}(m, n) = I(m, n) * G(m, n) \quad (3.8)$$

S is an adaptive contrast enhancement parameter related to the global standard deviation of the input intensity image, $I(m, n)$, and $*$ is the convolution operator, $I(m, n)$ is defined by

$$S = \begin{cases} 3 & \text{for } \sigma \leq 7 \\ 1.5 & \text{for } 7 < \sigma \leq 20 \\ 1 & \text{for } \sigma \geq 20 \end{cases} \quad (3.9)$$

σ is the contrast—standard deviation—of the original intensity image. If $\sigma < 7$, the image has poor contrast and the contrast of the image will be increased. If $\sigma \geq 20$, the image has sufficient contrast and the contrast will not be changed. Finally, the enhanced image can be obtained by linear color restoration based on chromatic information contained in the original image as

$$S_j(x, y) = I_{enh}(x, y) \frac{I_j(x, y)}{I(x, y)} \lambda_j \quad (3.10)$$

where $j \in \{r, g, b\}$ represents the RGB spectral band and λ_j is a parameter which adjusts the color hue.

3.2.3 Evaluation Criteria

In this work, following evaluation criteria was used

3.2.3.1 A new metric

There are some metrics such as brightness and contrast to characterize an image. Another such metric is sharpness. Sharpness is directly proportional to the high-frequency content of an image. So the new metric is defined as [62]

$$S = \sqrt{\|h \otimes I\|^2} = \sqrt{\sum_{v_1=0}^{M_1-1} \sum_{v_2=0}^{M_2-1} \left| \hat{h}[v_1, v_2] \hat{I}[v_1, v_2] \right|} \quad (3.11)$$

where h is a high-pass filter, periodic with period $M_1 \times M_2$ and \hat{h} is its direct Discrete Fourier Transform (DFT). I is also DFT of Image I . The role of \hat{h} (or h) is to weight the energy at the high frequencies relative to the low frequencies, thereby emphasizing the

contribution of the high frequencies to S . The larger the value of S , the greater the sharpness of I and conversely

Equation 3.11 defines how the sharpness should be computed and defined as

$$\hat{h}[v_1, v_2] = 1 - \exp\left(-\frac{v_1^2 + v_2^2}{\sigma^2}\right) \quad (3.12)$$

where σ is the parameter at which the attenuation coefficient $= 1 - e^{-1} \approx 2/3$. A smaller value of σ implies that fewer frequencies are attenuated and vice versa. For this dissertation $\sigma = 0.15$.

3.2.3.2 Image Quality Assessment

The overall quality of images can be measured by using the brightness μ , contrast σ and sharpness S , where brightness and contrast are assumed to be the mean and the standard deviation. However, instead of using global statistics, it is used regional statistics. In order to do this [62]

- 1) Divide the $M_1 \times M_2$ image I into $(M_1/10) \times (M_2/10)$ non-overlapping blocks, $I_t, t=1, \dots, 100$, such that $I \approx \cup_{t=1}^N I_t$, (Total Number of Regions are 100)
- 2) For each block compute the measures, μ , σ and S ,
- 3) Classify the block as either GOOD or POOR based on the computed measure (will be discussed with the following)
- 4) Classify the image as a whole as GOOD or POOR based upon the classification of regions (will be discussed with the following)

The following criteria are used for brightness, contrast and sharpness [62]

- 1) Let μ_n be normalized brightness parameter, such that

$$\mu_n = \begin{cases} \mu/255 & \mu < 154 \\ 1 - \mu/255 & \text{otherwise} \end{cases} \quad (3.13)$$

A region is considered to have sufficient brightness when $0.4 \leq \mu_n \leq 0.6$

2) Let σ_n be normalized contrast parameter, such that

$$\sigma_n = \begin{cases} \sigma/128 & \mu \leq 64 \\ 1 - \sigma/128 & \text{otherwise} \end{cases} \quad (3.14)$$

A region is considered to have sufficient contrast when $0.25 \leq \sigma_n \leq 0.5$. When $\sigma_n < 0.25$, the region has poor contrast, and when $\sigma_n > 0.5$, the region has too much contrast.

3) Let S_n be normalized sharpness parameter, such that $S_n = \min(2.0, S/100)$. When $S_n > 0.8$, the region has sufficient sharpness. Image Quality is evaluated using by

$$Q = 0.5\mu_n + \sigma_n + 0.1S_n \quad (3.15)$$

where $0 < Q < 1.0$ is the quality factor. A region is classified as good when $Q > 0.55$, and poor when $\sigma_n \leq 0.5$. An image is classified as GOOD when the total number of regions classified as GOOD, $N_G > 0.6N$.

3.2.4 Experimental Result

The image samples for ETNUD were selected to be as diverse as possible so that the result would be as general as possible. MATLAB was used for AINDANE and IRME algorithms and their codes were developed by the author and research team. MSRCR enhancement was done with commercial software, Photo Flair. From visual experience, the following statements are made about the proposed algorithm.

- 1) In the Luminance enhancement part it has been shown that ETNUD works well for darker images and the technique adjusts itself to the image (Figure 3.3)
- 2) In the contrast enhancement part it is clear that unseen or barely seen features of low contrast images are made visible
- 3) In Figure 3.4 and 3.5 Gamma Correction with $\gamma = 1.4$ does not provide good visual enhancement. IRME and MSRCR bring out the details in the dark but have some enhancement of noise in the dark regions, which can be considered objectionable. AINDANE does not bring out the finer details of the images including the regions in the face and in the sign. The ETNUD algorithm gives good result (in Table 3.1) and outperforms the other algorithms if the results are compared (in Table 3.2 and Table 3.3) due to the Evaluation Criteria. The ETNUD provides better visibility enhancement the best sharpness can be adjusted by the α parameter in Equation 3.3

Table 3.1. The Results of Evaluation Criteria for Figure 3.3

Figure 3.3	ORIGINAL IMAGE		ETNUD	
	NUMBER OF REGIONS		NUMBER OF REGIONS	
	GOOD	POOR	GOOD	POOR
TOP ROW IMAGE	60	40	100	-
SECOND ROW IMAGE	49	51	84	16
THIRD ROW IMAGE	36	64	72	28
LAST ROW IMAGE	32	68	99	1



Figure 3.3. The Results of Enhancement Left Column Original Images, Right Columns Enhanced Images

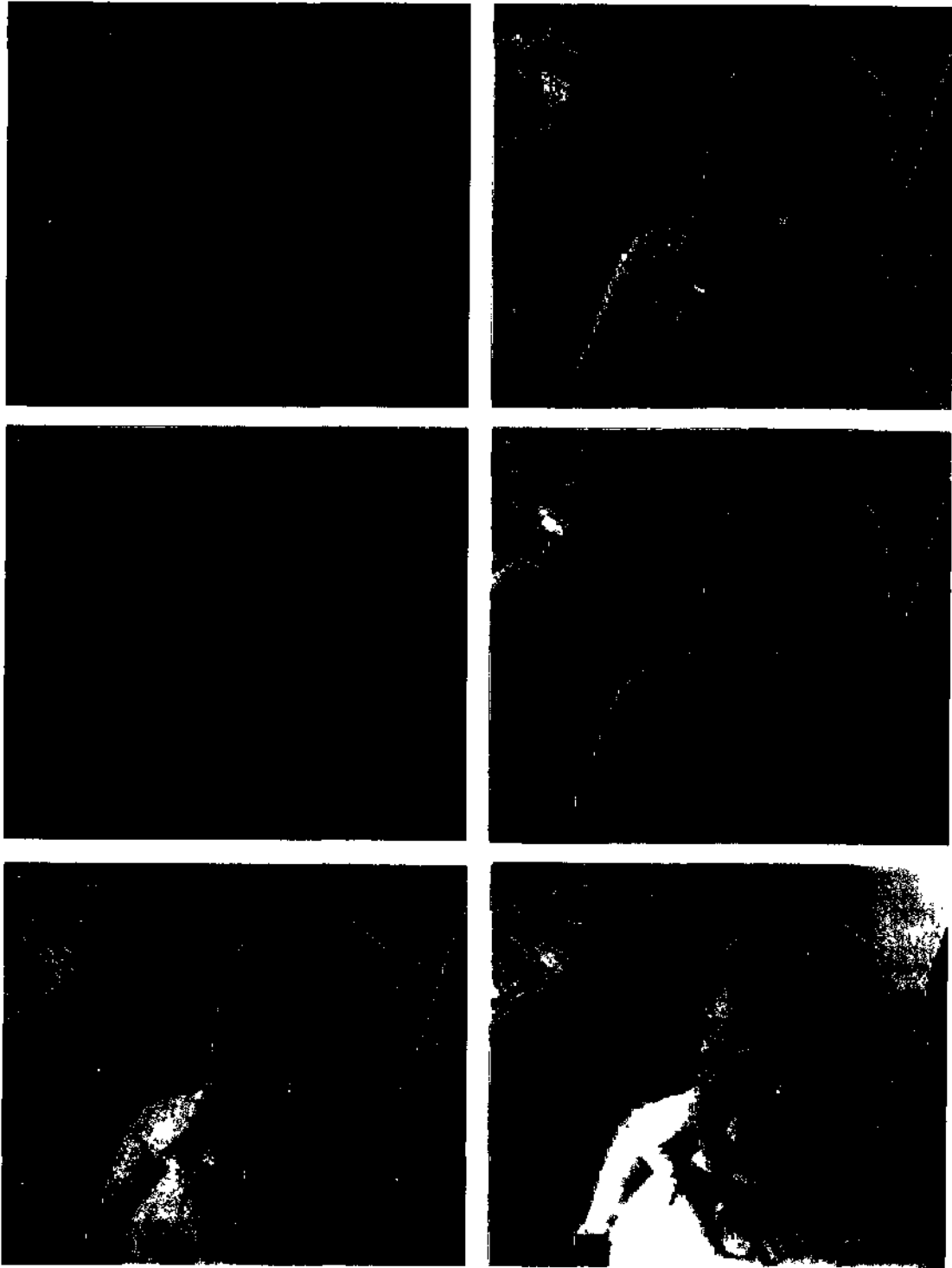


Figure 3.4. Comparisons of Enhancement Techniques (top-left) Original, (top-right) IRME, (middle-left) Gamma correction, $\gamma = 1.4$, (middle-right) MSR, (bottom-left) AINDANE, (bottom-right) ETNUD

Table 3.2. The Results of Evaluation Criteria for Figure 3 4

Figure 3 4	Original Image	Gamma	Irme	Aindane	Msr	Etnud
Number of Good Regions	51	64	93	72	89	98
Numberof Poor Regions	49	36	7	28	11	2

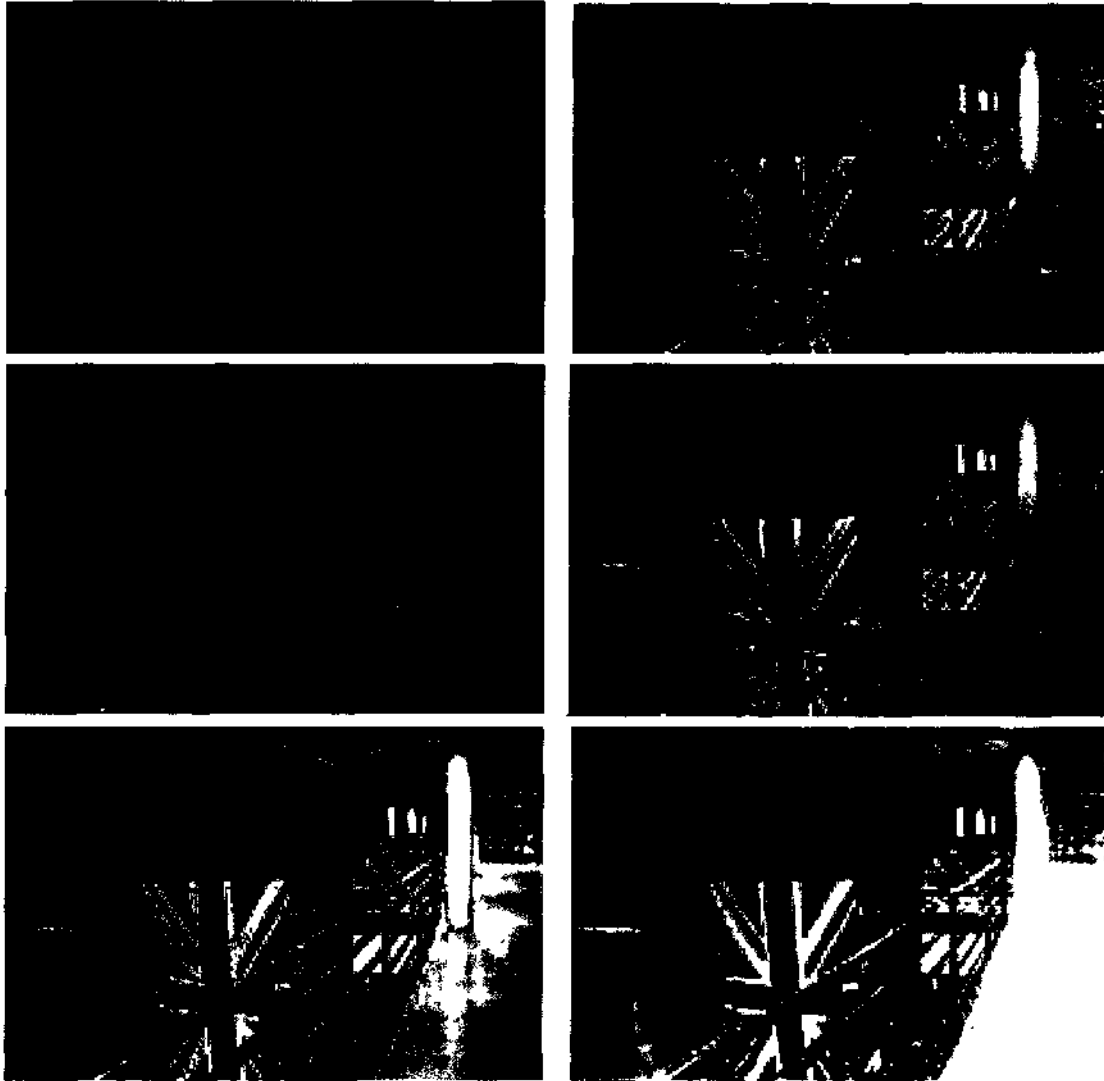


Figure 3.5. Comparisons of Enhancement Techniques (top-left) Original, (top-right) IRME, (middle-left) Gamma correction, $g = 1.4$, (middle-right) MSR, (bottom-left) AINDANE,(bottom-right) ETNUD

Table 3.3. The Results of Evaluation Criteria for Figure 3 5

Figure 3 5	Original Image	Gamma	Irme	Aindane	Msr	Etnud
Number of Good Regions	32	52	95	90	90	99
Number of Poor Regions	68	48	5	10	10	1

3.3 A Wavelet Based Enhancement Technique for Non-Uniform and Uniform-Dark Images (WBNUDE):

A new wavelet based image enhancement technique is proposed for non-uniform and uniform-dark image enhancement technique (WBNUDE) based on the principles of MSRCR, IRME and AINDANE. In this proposed technique, the discrete wavelet transform (DWT) is used for dimension reduction and the DRC and contrast enhancement algorithms are applied to the approximation coefficients. The detail coefficients are multiplied with a constant. After the inverse DWT (IDWT), the enhanced image is obtained by linear color restoration such that it tunes the intensity of each pixel magnitude based on its surrounding pixels. By using the process described above, WBNUDE can compress the bright regions and enhance the dark regions at the same time.

The new image enhancement algorithm is composed of four major parts: DWT, DRC, Contrast enhancement, and Color restoration. The DRC and the contrast enhancement are both applied in the DWT domain. The major innovation is in the selection of the transformation functions for DRC, and the selection of the surround scale

for contrast enhancement and color restoration. The algorithm is described in the following sections.

3.3.1 Discrete Wavelet Transform

The DWT has been widely used in image processing [63,64,65] for myriad applications. The DWT decomposes the luminance into approximation and detail coefficients. The WBNUDE is applied for gray-level images to these coefficients and the image is reconstructed by applying the inverse DWT. The WBNUDE process can be summarized as follows:

- Apply DWT decomposition for J levels and find the approximation coefficients, A , and detail coefficients H , V , and D
- Normalize A to get A_n in the range [0-1]
- Apply the non-linear DRC transfer function to A_n to produce modified coefficient A_m . This provides DRC and neighborhood dependent contrast enhancement
- De-normalize A_m *
- Perform the IDWT

Haar filters were used for the DWT. Each pass of the DWT decomposes the input into the four lower resolution approximation, horizontal, vertical and diagonal detail coefficients respectively (Step 1), so that

$$I(m, n) = \sum_{k \in \mathbb{Z}} A_{j,k,l} \Phi_{j,k,l}(m, n) + \sum_{j \geq J} \sum_{k \in \mathbb{Z}} d_{j,k,l}^h \Psi_{j,k,l}^h(m, n) + \sum_{j \geq J} \sum_{k \in \mathbb{Z}} d_{j,k,l}^v \Psi_{j,k,l}^v(m, n) + \sum_{j \geq J} \sum_{k \in \mathbb{Z}} d_{j,k,l}^d \Psi_{j,k,l}^d(m, n) \quad (3.16)$$

where $A_{j,k,l}$ are the approximation coefficients at scale j with the corresponding scaling functions $\Phi_{j,k,l}(m, n)$. And $d_{j,k,l}$ are the vertical, horizontal and diagonal detail coefficients

at scale j with the corresponding wavelet functions $\Psi_{j,k,l}(m,n)$. The normalized coefficients in Step 2 are obtained by

$$A_n(m,n) = A_{j,k,l}(m,n) / 255 \quad (3.17)$$

In the third step, the two transfer functions are applied, as described in Section 3.2.3.2 to $A_n(m,n)$

3.3.2 The Placement of Function for DRC:

RGB color images $I_c(m,n)$ can be converted to intensity images $I(m,n)$ using Equation 3.1. The DWT is applied to the intensity image rather than to each component of the color image. The transfer functions for DRC and local contrast enhancement are based on some information extracted from the histogram of $I(m,n)$. To do this, the histogram is divided into four ranges: $r_1 = 0-63$, $r_2 = 64-127$, $r_3 = 128-191$ and $r_4 = 192-255$. A_n is mapped to A_n^{drc} using the following relationships

$$A_n^{drc} = \left\{ (A_n)^x \quad 0 < x \leq 1 \right\} \quad (3.18)$$

$$x = \begin{cases} 0.1, & \text{if } (f(r_1 + r_2) \geq f(r_3 + r_4)) \wedge (f(r_1) \geq f(r_2)) \\ 0.3, & \text{if } (f(r_1 + r_2) \geq f(r_3 + r_4)) \wedge (f(r_1) < f(r_2)) \\ 3, & \text{if } (f(r_1 + r_2) < f(r_3 + r_4)) \wedge (f(r_3) \geq f(r_4)) \\ 5, & \text{if } (f(r_1 + r_2) < f(r_3 + r_4)) \wedge (f(r_3) < f(r_4)) \end{cases} \quad (3.19)$$

$f(r_1 + r_2) = f(r_1) + f(r_2)$ and \wedge is the logical AND operator. The first transformation pulls out the details in the dark regions for $x < 1$, where the values of x are obtained from Equation 3.19. The curves for the ranges are shown in Figure 3.6. The determination of the x values in Equation 3.19 was done experimentally using a large number of non-uniform

and uniform dark images but it can be also determined manually based on the image information

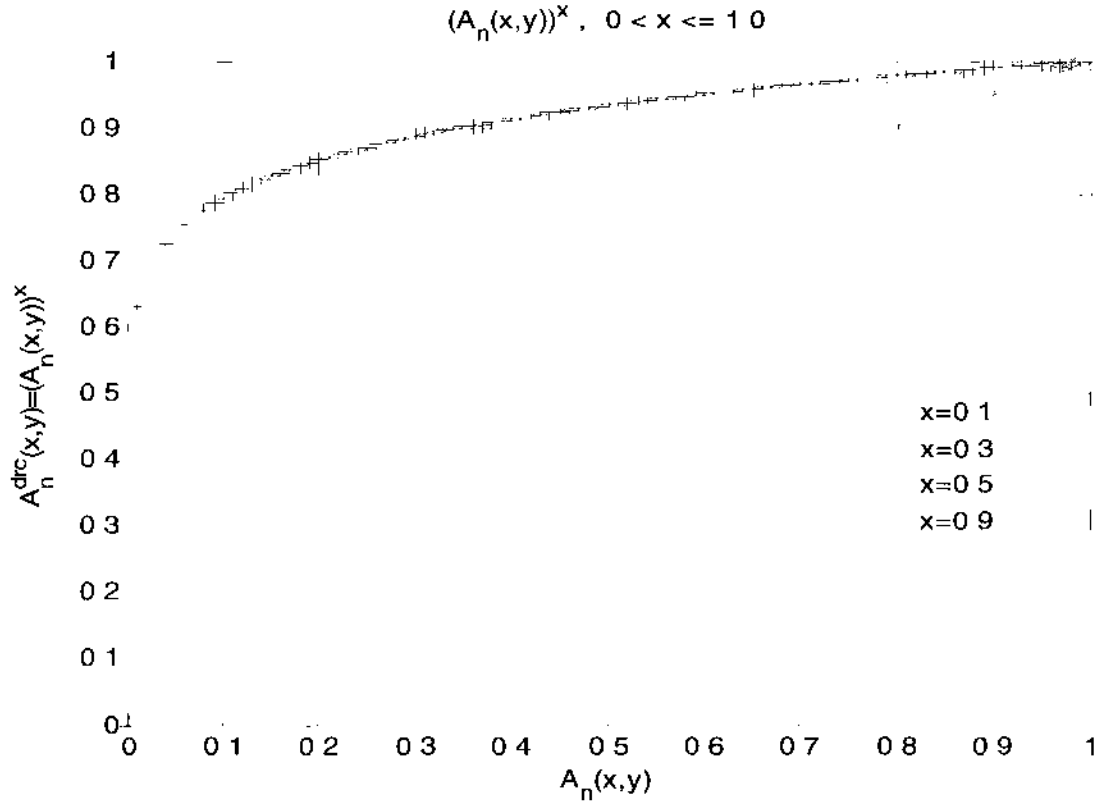


Figure 3.6. A_n^{drc} for Different Ranges r_i

The second transfer function is used for mapping A_n^{drc} to A_{en}^{drc} using the following process

First, A_n^{drc} is mapped to $T(m,n)$ using

$$T(m,n) = \log \frac{A_n^{\text{drc}}(m,n) - \min(A_n^{\text{drc}}(m,n)) - 1}{\max(A_n^{\text{drc}}(m,n)) + 1 - A_n^{\text{drc}}(m,n)} \quad (3.20)$$

Then $T(m,n)$ is normalized

$$T_n(m,n) = \frac{T(m,n) - \min(T(m,n))}{\max(T(m,n)) - \min(T(m,n))} \quad (3.21)$$

$T_n(m, n)$ is mapped to A_{en}^{drc} , the new enhanced approximation coefficients, using the following equation

$$\begin{aligned} A_{en}^{drc} &= (T_n(m, n)(\alpha - \beta) + \beta)^r \\ \alpha &= \max(A_n^{drc}), \quad \beta = \min(A_n^{drc}) \end{aligned} \quad (3.22)$$

where r is the curvature parameter for adjusting the shape of the transfer function. With this transformation, the details can be pulled out in the dark regions while suppressing the bright overshoots. The curve can be adjusted with r as shown in Figure 3.7.

The fourth step is A_{en}^{drc} is de-normalized by multiplying it with 255. Then, in the last step, the image is reconstructed from the de-normalized approximation coefficients A_{en}^{drc} by applying the IDWT. The DRC enhancements were experimentally determined alone result in an image that typically has poor contrast. So a local, neighborhood dependent, contrast enhancement method was applied to improve the contrast before the image is reconstructed.

3.3.3 Selection of surround parameter for contrast enhancement

A center/surround ratio was proposed, proposed by Hulbert [61], who showed that the Gaussian is the optimal surround for center-surround natural vision operations. The surround for the approximation coefficient is obtained by using a 2D discrete convolution with a Gaussian kernel, $G(m, n)$ defined as in Equation 3.5. The kernels for improved rendition use $\sigma_s = 15, 80$ and 220 for the surround space constant. The center-surround contrast enhancement is carried out as shown below and the approximation coefficients A_{en}^{drc} are replaced with coefficients A_{enh} using

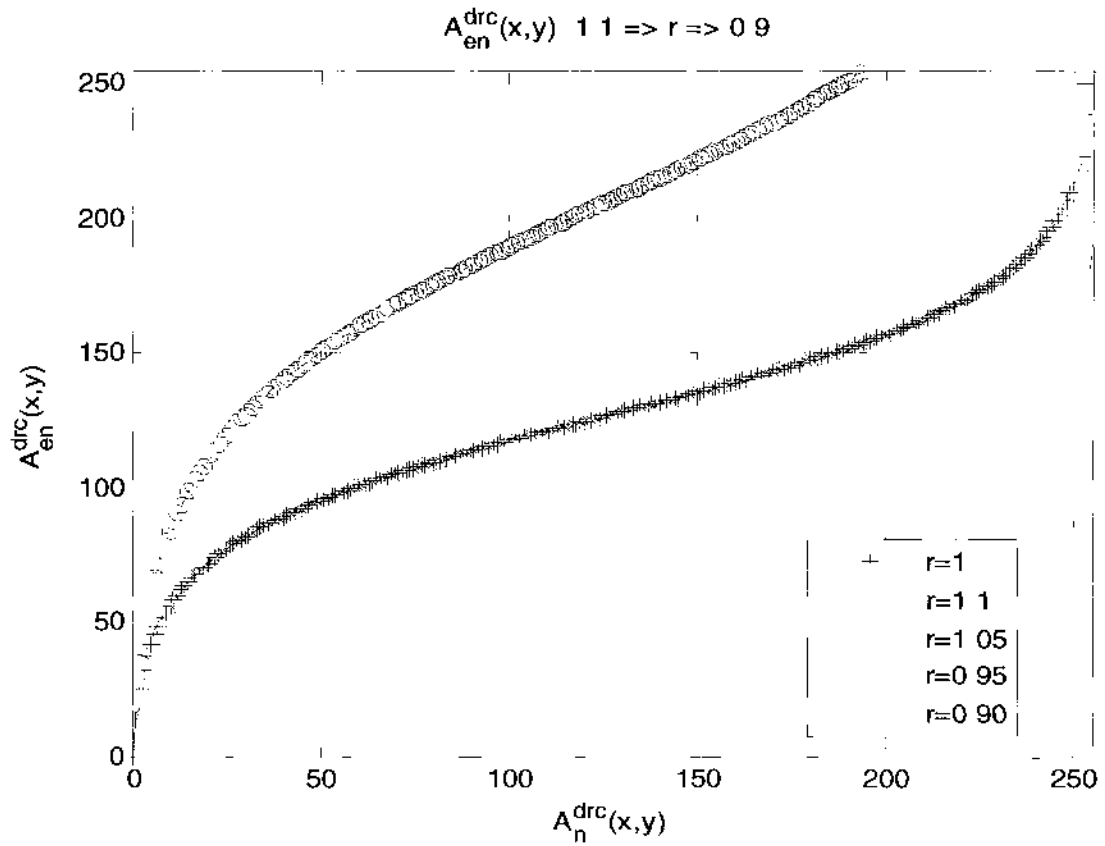


Figure 3.7. A_{en}^{drc} for Different Ranges r_i

$$A_{enh}(m, n) = 255 A_{enh}^{drc}(m, n)^{E(m, n)} \quad (3.23)$$

where, $E(m, n)$ is obtained by the same Equations between 3.7-3.9 such as

$$E(m, n) = \left[\frac{A_{filt}(m, n)}{A(m, n)} \right]^S \quad (3.24)$$

$$A_{filt}(m, n) = A(m, n) * G(m, n) \quad (3.25)$$

‘*’ is the convolution operator, and S is the adaptive contrast enhancement parameter. S is related to the global standard deviation and same procedure has been applied here as in Section 3.2.2. The approximation coefficients $A_{j_k l_i}(m, n)$ are replaced with the enhanced

coefficients $A_{enh}(m, n)$, before reconstruction. Additionally, the detail coefficients are multiplied with a constant before applying the IDWT.

3.3.4 Color restoration

Finally, the enhanced image can be obtained by the same procedure, applied in Section 3.2.2. Linear color restoration based on chromatic information contained in the original image as

$$S_j(m, n) = A_{enh}(m, n) \frac{I_j(m, n)}{I(m, n)} \lambda_j \quad (3.26)$$

3.3.5 Evaluation Criteria

In this work, the same evaluation criteria were used as discussed in Section 3.2.3.

3.3.6 Experimental Result

The proposed algorithm was tested with many non-uniform and uniform-dark images. MATLAB codes for AINDANE and IRME were used that were developed by research team. MSRCR enhancements were done with the commercial software, PhotoFlair. Figure 3.8 shows the original and the enhanced images by WBNUDE. Figure 3.9 shows original enhanced images by Gamma Correction, MSRCR, AINDANE, IRME and WBNUDE. From our own visual experience, the following statements can be made about the proposed algorithm.

- 1) WBNUDE works well for non-uniform and uniform dark images for the luminance enhancement, bringing out the details in the dark regions (Figure 3.8).
- 2) WBNUDE algorithm gives good results for contrast enhancement. The number of good regions in the images increased with the application of WBNUDE (Table 3.4).

3) In Figure 3 9 Gamma Correction (middle-left) does not provide good visual enhancement IRME (top-right), AINDANE (bottom-left) and MSRCR (middle-right) bring out the details in the dark regions but also enhance noise, which can be considered objectionable The WBNUDE algorithm outperforms the other algorithms and if the results are compared in Table 3 5 WBNUDE provides better visibility enhancement but does not necessarily provide the best sharpness

Table 3.4. The Results of Evaluation Criteria for Figure 3 8

Figure 3 8	ORIGINAL IMAGE		WBNUDE	
	NUMBER OF REGIONS		NUMBER OF REGIONS	
	GOOD	POOR	GOOD	POOR
TOP ROW IMAGE	60	40	100	-
SECOND ROW IMAGE	49	51	98	2
THIRD ROW IMAGE	100	-	100	-
LAST ROW IMAGE	100	-	100	-

TABLE 3.5. The Results of Evaluation Criteria for Figure 3 9

Figure 3 9	ORIGINAL IMAGE	GAMMA	IRME	AINDANE	MSR	WBNUDE
Number of Good Regions	60	60	98	99	82	100
Number of Poor Regions	40	40	2	1	18	-

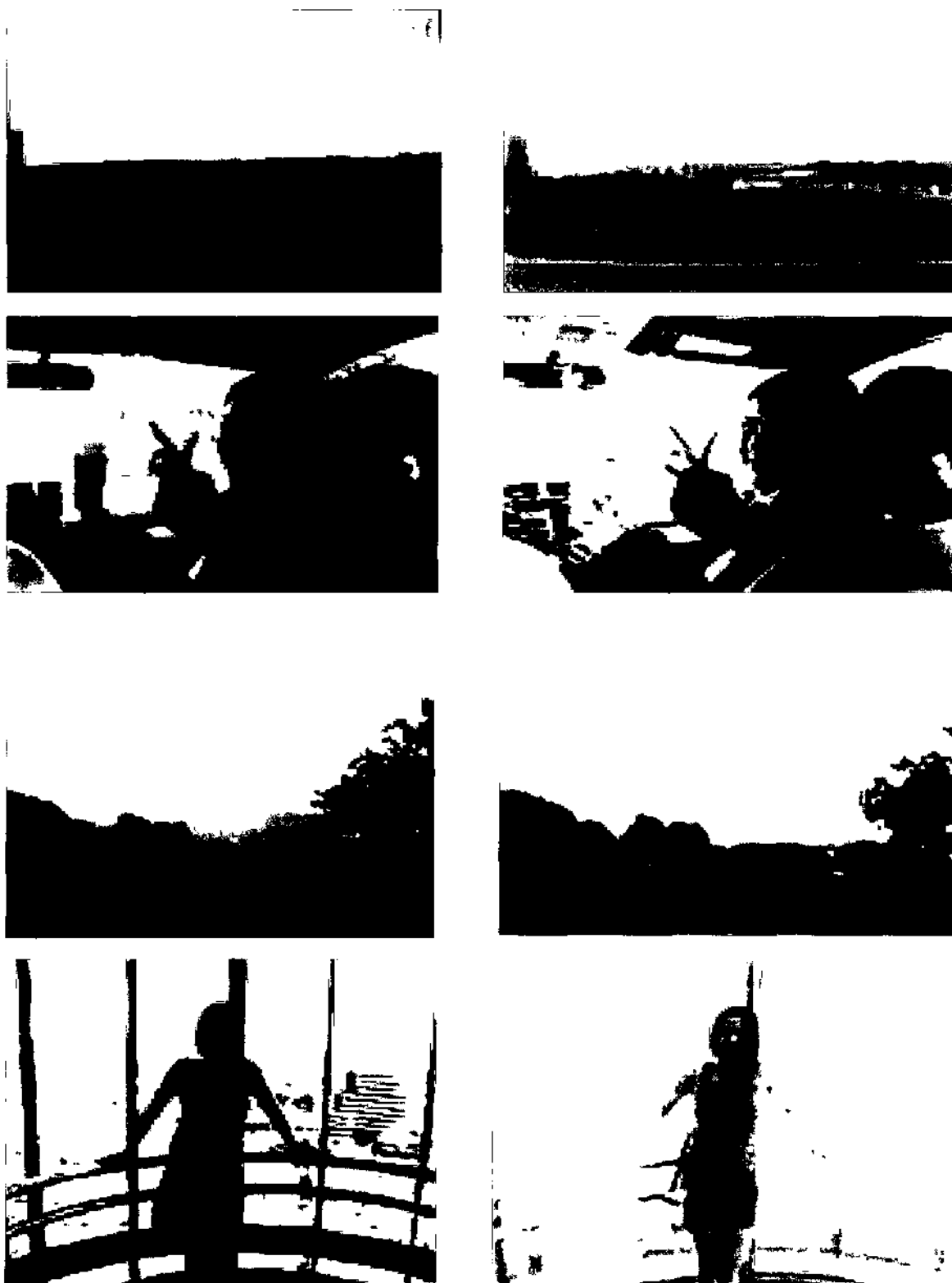


Figure 3.8. The Results of Enhancement Left Column Original Images, Right Columns
Enhanced Images (WBNUDE)

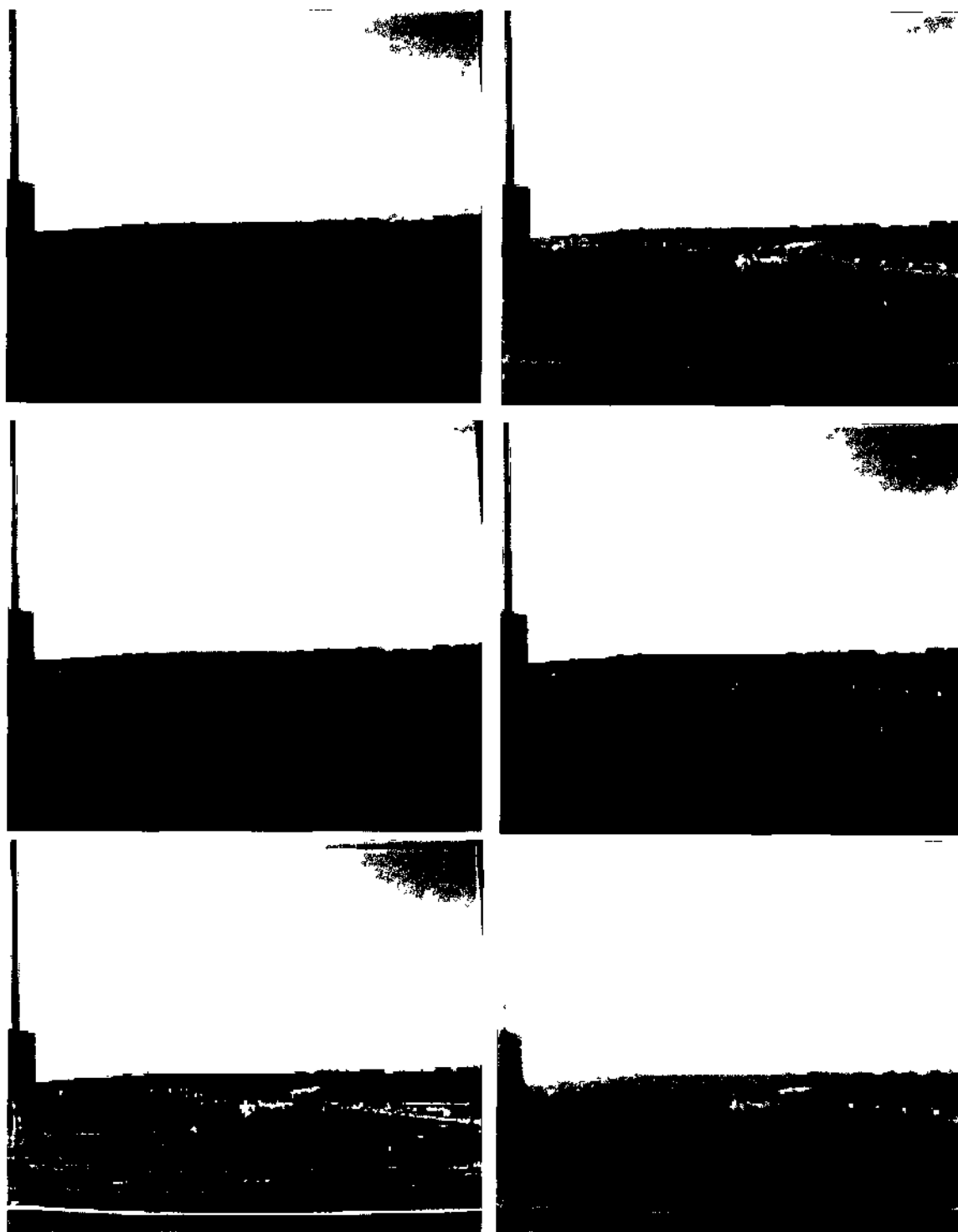


Figure 3.9. Comparisons of Enhancement Techniques (top-left) Original, (top-right) IRME, (middle-left) Gamma correction, $g = 1.4$, (middle-right) MSRCR, (bottom-left) AINDANE, (bottom-right) WBNUDE

3.4 Conclusion

The ETNUD and WBNUDE image enhancement algorithms provide high color accuracy and better balance between the luminance and contrast in images

4. ENTROPY-BASED IMAGE FUSION WITH A CONTINUOUS GENETIC ALGORITHM

4.1 Introduction

Image fusion is defined as the process of combining information from two or more images of a scene to enhance the viewing or understanding of that scene [66]. The images that are to be fused can come from different sensors, or have been acquired at different times, or from different locations. Hence, the first step in any image fusion process is the accurate registration of the image data. This is relatively straightforward if parameters such as the instantaneous field-of-view (IFOV), and locations and orientations from which the images are acquired are known, especially when the sensor modalities produce images that use the same coordinate space. This is more of a challenge when sensor modalities differ significantly and registration can only be accomplished at the information level. Hence, the goal of the fusion process is to preserve all relevant information in the component images and place it in the fused image (FI). This requires that the process minimize the noise and other artifacts in the FI. Because of this, the fusion process can be also regarded as an optimization problem [44]. In recent years, image fusion has been applied to a number of diverse areas such as remote sensing [67, 68], medical imaging [69, 70, 71], and military applications [39, 72].

Image fusion can be divided into three processing levels: pixel, feature and decision. These methods increase in abstraction from pixel to feature to decision levels. In the pixel-level approach, simple arithmetic rules like average of individual pixel intensities or more sophisticated combination schemes are used to construct the fused image. At the feature-level, the image is classified into regions with known labels, and

these labeled regions from different sensor modalities are used to combine the data. At the decision level, a combination of rules can be used to include part of the data or not.

Genetic algorithms (GA) are an optimization technique that seeks the optimum solution of a function based on the Darwinian principles of biological evolution [29]. Even though there are several methods of performing and evaluating image fusion, there are still many open questions. In this dissertation, a new measure of image fusion quality is provided and compared with many existing ones. The focus is on pixel-level image fusion (PLIF) and a new image fusion technique that uses GA is proposed.

The GA is used to optimize the parameters of the fusion process to produce an FI that contains more information than either of the individual images. The main purpose of this section is in finding the optimum weights that are used to fuse images with the help of CGA.

The techniques for GA and image fusion are given in Section 4.2. Section 4.3 describes the evaluation criteria. Section 4.4 describes the experimental results, and compares our results with other image fusion techniques. In Section 4.5, conclusion is provided.

4.2 The Techniques of GA and Image Fusion

4.2.1 Genetic Algorithm

As stated earlier, GA is a non-linear optimization technique that seeks the optimum solution of a function via a non-exhaustive search among randomly generated solutions [29]. GAs use multiple search points instead of searching one point at a time and attempt to find global, near-optimal solutions without getting stuck at local optima. Because of these significant advantages, GAs reduce the search time and space [30].

However, there are disadvantages of using GAs as well they are not generally suitable for real-time applications since the time to converge to an optimal solution cannot be predicted. The convergence time depends on the population size, and the GA crossover and mutation operators [29]

In this fusion process, a continuous genetic algorithm has been selected

4.2.2 Continuous Genetic Algorithm (CGA)

GAs typically operates on binary data. For many applications, it is more convenient to work in the analog, or continuous, data space rather than in the binary space of most GAs. Hence, CGA is used because they have the advantage of requiring less storage and are faster than binary. CGA inputs are represented by floating-point numbers over whatever range is deemed appropriate. Figure 2.15 shows the flowchart of a simple CGA [35]

The various elements in the flowchart are described below

(i) *Definition of the cost function and the variables* The variable values are represented as floating point numbers (p_i). In each chromosome, the basic GA processing vector, there are number of value depending on the parameters ($p_1, \dots, p_{N_{var}}$). Each chromosome has a cost determined by evaluating the cost function [35]

(ii) *Initial Population* To begin the CGA process, an initial population must be defined. A matrix represents the population, with each row being a $1 \times N_{var}$ chromosome of continuous values. The chromosomes are passed to the cost function for evaluation [35]

(iii) *Natural Selection* The chromosomes are ranked from the lowest to highest cost. Of the total of chromosomes in a given generation, only the top N_{keep} are kept for mating and the rest are discarded to make room for the new offspring [35]

(iv) *Mating* Many different approaches have been tried for crossover in continuous GAs. In crossover, all the genes to the right of the crossover point are swapped. Variables are randomly selected in the first pair of parents to be the crossover point $\alpha = \lfloor U(0,1)N_{var} \rfloor$, where $U(0,1)$ is the uniform distribution. The parents are given by [35]

$$\begin{aligned} parent_1 &= [P_{m1}, \dots, P_{mN}] \\ parent_2 &= [P_{d1}, \dots, P_{dN}] \end{aligned} \quad (4.1)$$

where subscripts m and d represent the mom and dad parent. Then the selected variables are combined to form new variables that will appear in the children

$$\begin{aligned} pnew_1 &= p_{m\alpha} - \beta[P_{m\alpha} - P_{d\alpha}] \\ pnew_2 &= p_{d\alpha} + \beta[P_{m\alpha} - P_{d\alpha}] \end{aligned} \quad (4.2)$$

where β is a random value between 0 and 1. The final step is to complete the crossover with the rest of chromosome

$$\begin{aligned} offspring_1 &= [P_{m1}, P_{m2}, \dots, pnew_1, \dots, P_{dN_{var}}] \\ offspring_2 &= [P_{d1}, P_{d2}, \dots, pnew_2, \dots, P_{mN_{var}}] \end{aligned} \quad (4.3)$$

(v) *Mutation* If care is not taken, the GA can converge too quickly into one region of the cost surface. If this area is in the region of the global minimum, there is no problem. However, some functions have many local minima. To avoid overly fast convergence, other areas of the cost surface must be explored by randomly introducing changes, or mutations, in some of the variables. Multiplying the mutation rate by the total number of variables that can be mutated in the population gives the amount of mutation

Random numbers are used to select the row and columns of the variables that are to be mutated [35]

(vi) *Next Generation* After all these steps, the starting population for the next generation is ranked. The bottom ranked chromosomes are discarded and replaced by offspring from the top ranked parents. Some random variables are selected for mutation from the bottom ranked chromosomes. The chromosomes are then ranked from lowest cost to highest cost. The process is iterated until a global solution is achieved.

4.2.3 Image Fusion

A set of input images of a scene, captured at a different time or captured by different kinds of sensors at the same time, reveals different information about the scene. The process of extracting and combining data from a set of input images to form a new composite image with extended information content is called image fusion [73]. The image fusion process must satisfy the following requirements [74,75]

- The FI must preserve the complementary information in the input images
- The redundant information must be taken account in the FI
- The location of the input images should not depend on the fusion process
- The most recent and advanced methods used for image fusion are wavelet-based

In these methods, the discrete wavelet transform (DWT) is performed on each of input images. The corresponding approximation and detail coefficients are fused based on some optimization criteria. Finally, the inverse DWT is utilized to produce the fused image [36].

4.3 Evaluation Criteria

In this section, the following criteria were defined to evaluate the performance of the image fusion algorithm

4.3.1 Image Quality Assessment

This evaluation criterion was discussed in Section 3.2.3.2

4.3.2 Entropy

Entropy is often defined as the amount of information contained in an image. Mathematically, entropy is usually given as [42]

$$E = -\sum_{i=0}^{L-1} p_i \log_2 p_i \quad (4.4)$$

where L is the total number of grey levels, and $p = \{p_0, \dots, p_{L-1}\}$ is the probability of occurrence of each level. An increase in entropy after fusion can be interpreted as an overall increase in the information content. Hence, one can assess the quality of fusion by assessing entropy of the original data, and the entropy of the fused data.

4.3.3 Mutual Information Indices

Mutual Information Indices are used to evaluate the correlative performances of the fused image and the source images. Let A and B be random variables with marginal probability distributions $p_A(a)$ and $p_B(b)$ and the joint probability distribution $p_{AB}(a,b)$. The mutual information is then defined as [42]

$$I_{AB} = \sum p_{AB}(a,b) \log[p_{AB}(a,b)/(p_A(a)p_B(b))] \quad (4.5)$$

A higher value of Mutual Information (MI) indicates that the fused image, F , contains fairly good quantity of information present in both the source images, A and B .

The MI can be defined as $MI = I_{AF} + I_{BF}$

A high value of MI does not imply that the information from the both images is symmetrically fused. Therefore, information symmetry (IS) is introduced. IS is the indication of how symmetrically distributed is the information in the fused image, with respect to input images. The higher the value of IS, the better the fusion result. IS is given by [42]

$$IS = 2 - abs[I_{AF} / (I_{AF} + I_{BF}) - 0.5] \quad (4.6)$$

4.4 Experimental Results

The goal of this experiment is to fuse visual and IR images. To minimize registration issues, it is important that the visual and the thermal images are captured at the same time. Pinnacle software was used to capture the visual and the thermal images simultaneously. Although radiometric calibration is important, the thermal camera can not always be calibrated in field conditions because of constraints on time. Figure 4.1 shows an example where the IR and visual image were captured at the same time. It is obvious from the figure that the images need to be registered before they can be fused since the field-of-view and the pixel resolution are obviously different.

The performance of the proposed algorithm was tested and compared with different PLIF methods. The IR and visual images were not previously registered as shown in Figure 4.1. The registered image, base image (IR Image) and fused image with CGA are shown in Figure 4.2. The cost function is very simple and defined as

$$Entropy(F = w_a V + w_b IR) \quad (4.7)$$

where V and IR are the visual and IR images, w_a and w_b are the respective associated weights, and F is the fused image. The initial population size is 100×3 . The first and second columns in population matrix represent $w_a V$, and $w_b IR$ and the last column

represents the cost function which is the entropy of F . Then initial population has been ranked based on the cost. In each iteration of the GA, 20 of the 100 rows are kept for mating and the rest are discarded. The crossover has been applied based on the Equation 4.2. The mutation rate was set to 0.20, hence the total number of mutated variables is 40. The value of a mutated variable is replaced by a new random value in the same range.

Figure 4.3 shows the CGA results after 50 iterations of the GA such that the CGA maximizes the cost and finds optimum weights of images. In the 2nd, 8th, and 25th iterations, the cost increased but was not associated with the global solution. The optimum solution was determined in the 45th iteration and remained unchanged because it is the optimum solution. Figure 4.4 shows the fusion results of point-rules based PLIF. After registering IR and visual data, we determined that $w_a = 0.9931$ and $w_b = 0.0940$ provide the optimum values for maximizing the entropy cost function for the F specified in Equation 4.7. The evaluation of these weights results is shown in Table 4.1. Table 4.1 shows that CGA based fusion method gives better results (optimum weights for maximizing the entropy of F) for entropy and IS from which it can be concluded that CGA performs better than other PLIFs.



Figure 4.1. Visual and IR Images. Left: Visual Image, Right: IR Image

4.5 Conclusion

In this dissertation, CGA based image fusion algorithm was introduced and compared with other classical PLIFs. The results show that CGA based image fusion gives better result than other PLIFs.

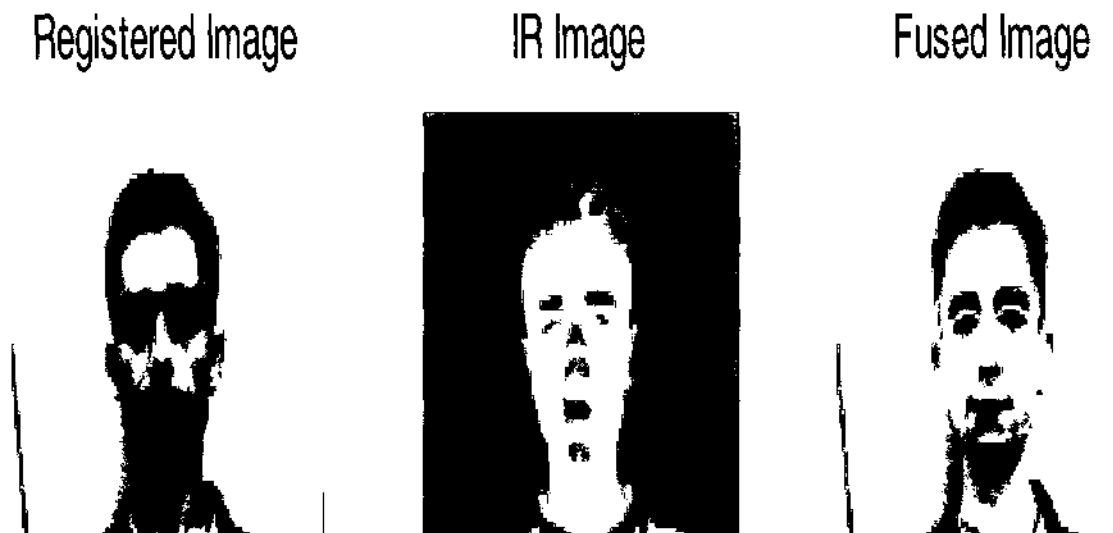


Figure 4.2. The Result of Fusion Left Registered Images, Middle IR Image Right Fused Image with GA

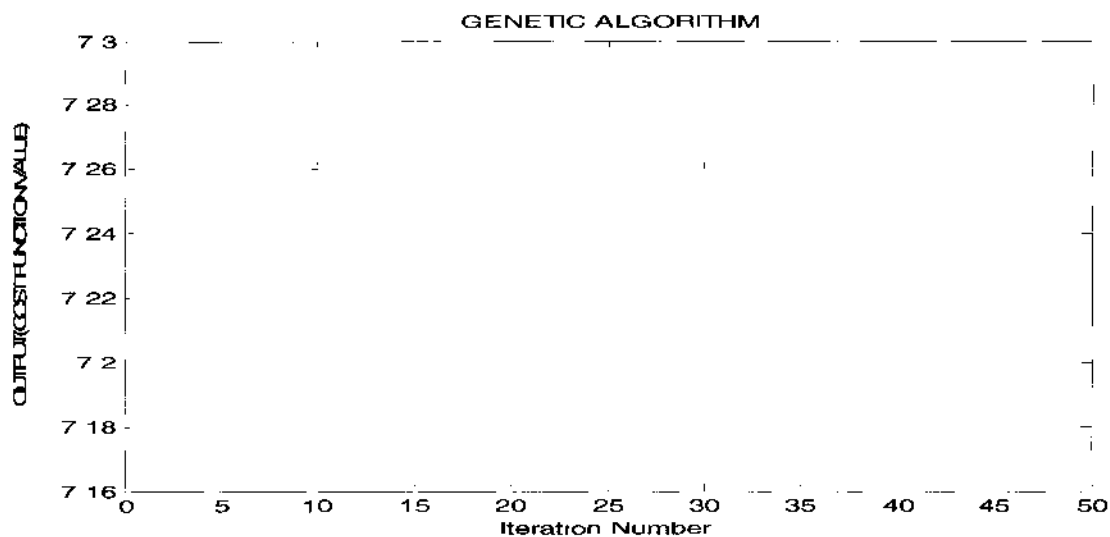


Figure 4.3. The Result of Continuous Genetic Algorithm

Table 4.1. Performance Comparison of Image Fusion Methods for Figure 4 2 and Figure 4 4

	Highest (Fig 4 4)	Lowest (Fig 4 4)	Average (Fig 4 4)	Threshold (Fig 4 4)	GA_based (Fig 4 2)
Entropy	6.91	3.14	6.56	6.93	7.28
Image Quality (Number of Good Regions)	100	70	100	100	100
IS	1.90	1.63	1.96	1.91	1.96



Fig. 4.4. Fusion Results (top-left) highest value from IR or Visual Images, (top-right) lowest value from IR or Visual Images, (bottom-left) average of IR and Visual Images, (bottom-right) threshold value

5. EXPERIMENTAL RESULTS

5.1 Introduction

With face recognition, a database usually exists that stores a group of human faces with known identities. In a testing image, once a face is detected, the face is cropped from the image or video as a probe to check with the database for possible matches. The matching algorithm produces a similarity measure for each of the comparing pairs.

Variations among images from the same face due to changes in illumination are typically larger than variations from a change of face identity. In an effort to address the illumination and camera variations, a database was created, considering these variations to evaluate the proposed techniques.

Besides the regular room lights, four additional spot lights are located in the front of the person that can be turned off and on in sequence to obtain face images under different illumination conditions. Note that it is important to capture visual and thermal images at the same time in order to see the variations in the facial images. Visual and thermal images are captured almost at the same time. Although radiometric calibration is important, the thermal camera can not be calibrated because of current IR camera characteristics.

The Pinnacle (Pinnacle Systems Ltd.) software has been implemented to capture visual and thermal images at the same time. Figure 5.1 shows an example of visual and thermal images taken at the same time.

In this dissertation, the focus is on visual image enhancement. Then the visual images will be registered with the IR images based landmark registration algorithm.

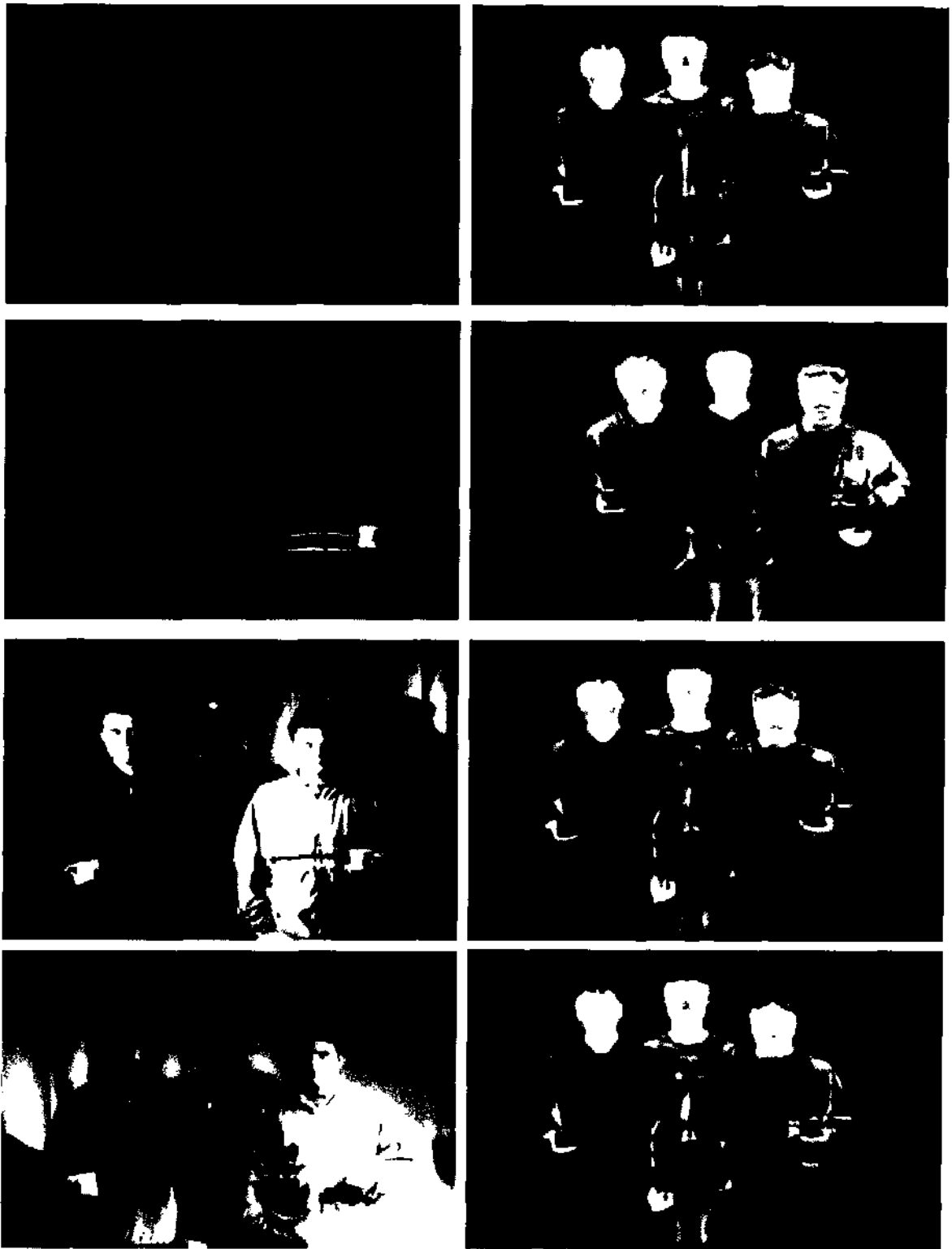


Figure 5.1. Database Images Left Column Visual Images, Right Columns IR Images (taken at the same time)

Finally, the registered IR and visual images are fused for face recognition Fig 5.2 shows the workflow of the proposed work

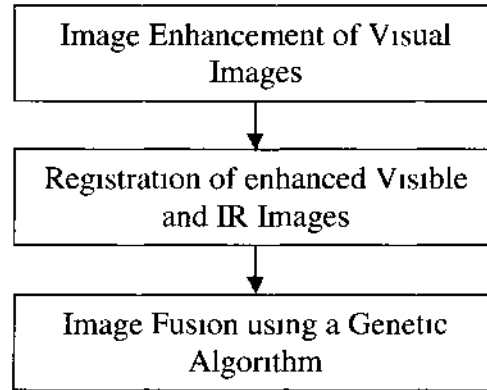


Figure 5.2. Research Approach Overview

5.2 IR Images

In this subsection, some sample IR images are shown with and their statistics such as mean, standard deviation of pixels in the images. Those statistics can give us information on the contrast of the images. Fig 5.3 shows one IR image with its statistics and Fig 5.4 shows the same image after histogram equalization with modified image statistics. From the both Images it can be said that the mean and standard deviation has been significantly increased after histogram equalization.

And then the IR images were taken from different distances and statistics of those IR images shown in Table 5.1. It is observed that from the values of Table 5.1. Those values go down while the person retreats from the IR camera.

The background, shown in Figure 5.13, is subtracted from the Figures 5.5 to 5.8. Figures 5.9 to 5.12 show the images after their background subtraction. The statistics of IR images are shown in Table 5.1. It is observed that the values go down while the person retreats from the IR camera.

Table 5.1. The Statistics of Figures 5 5-5 8

Figure	Mean	Standard Deviation	RMS	Entropy
Left Upper IR 5 5	84 68020833	32 21200643	90 59995056	6 02810125
Right Upper IR 5 6	83 36513021	27 53482620	87 79471276	5 68955721
Left Bottom IR 5 7	84 87854167	24 43418270	88 32551228	5 42193817
Right Bottom IR 5 8	83 92352865	24 60098869	87 45494443	5 50655880

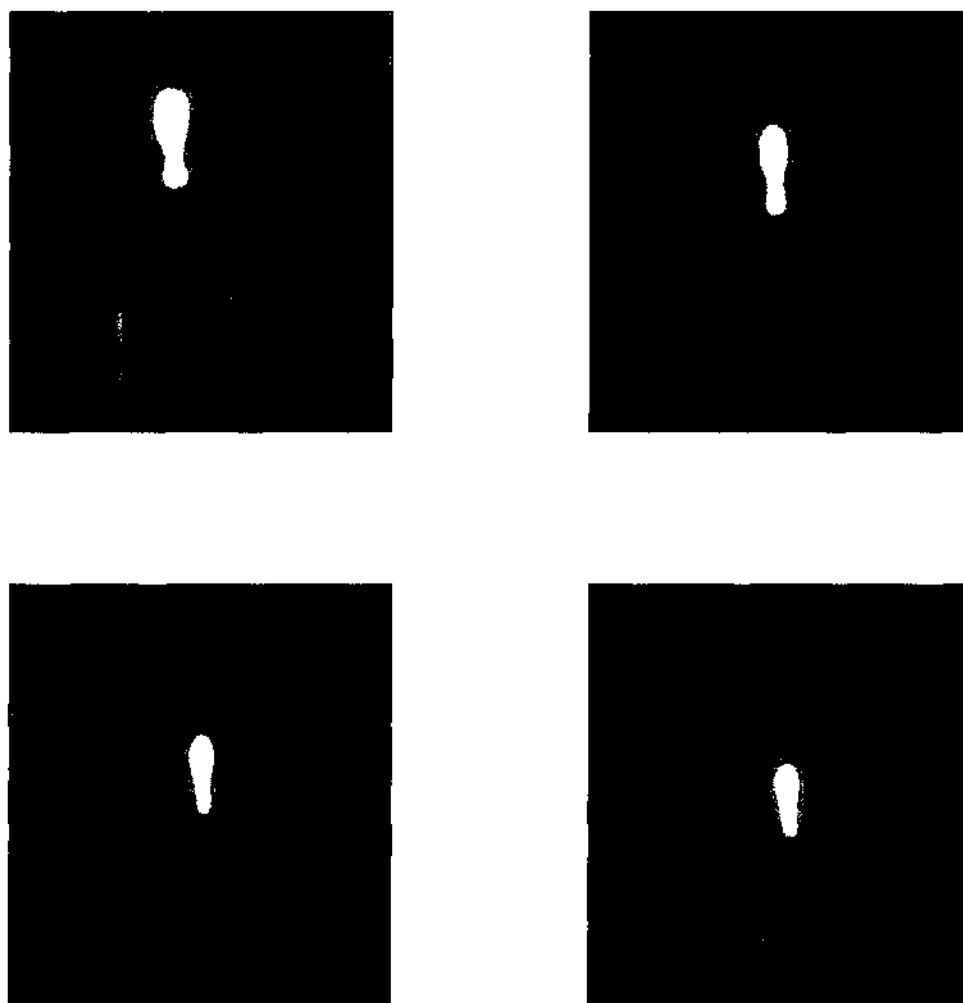
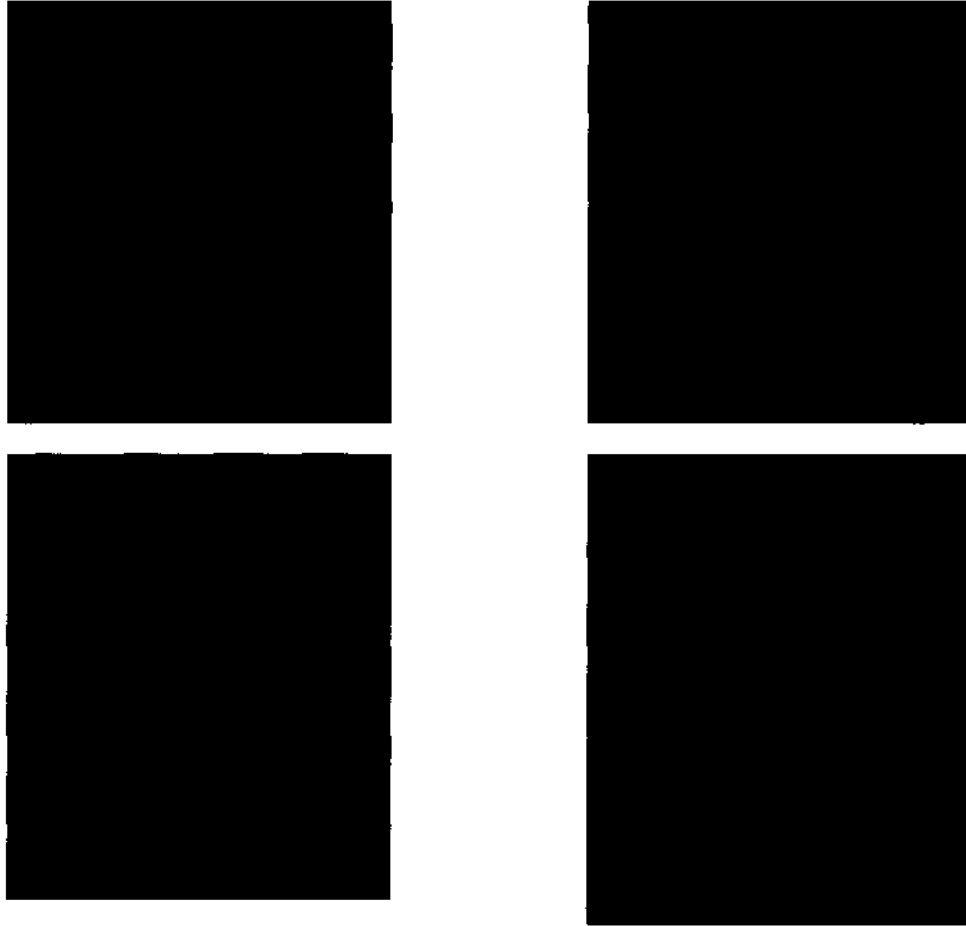
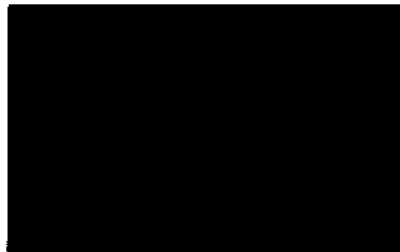
**Figure 5.5-5.8.** IR Images from Different Distances

Table 5.2. The Statistics of Figures 5 9 -5 13

Figure	Mean	Standard deviation	RMS	Entropy
Left Upper IR 5 9	9 42182292	26 74171275	28 35295307	2 12672017
Right Upper IR 5 10	7 01039063	22 87623110	23 92629361	1 76482414
Left Bottom IR 5 11	5 85242188	20 63104752	21 44506851	1 60233358
Right Bottom IR 5 12	5 39322917	20 36353732	21 06562539	1 37625036
5 13	84 54343750	9 86076578	85 11655260	4 10966349

**Figure 5.9-5.12.** IR Images without their Background from Different Distances**Figure 5.13.** The Background

5.2.1 Discussion

IR and CCD have their own advantages and limitations. For example, in IR images, the object may be highly detectable because of its sufficient temperature difference from the local background, whereas the visible images will provide more details of the background. Thermal IR and particularly Long Wave Infra-Red (LWIR) imagery is independent of illumination since thermal IR sensors operating at particular wavelength bands measuring heat energy emitted and not the light reflected from the objects. More importantly, IR energy can be viewed in any light conditions and is less subject to scattering and absorption by smoke or dust than visible light. Hence thermal imaging has great advantages in face recognition under low illumination conditions and even in total darkness, where visual face recognition techniques fail. It is well known that the detection of an object in an infrared image depends on its thermal contrast with the background. However, thermal imaging needs to solve several challenging problems. Thermal signatures can be changed significantly according to different body temperatures caused by physical exercise or ambient temperatures and the target intensity varies continuously with changing distance between the imaging device and target. A combined use of visual and thermal images face recognition system can alleviate the problems [38,39].

Here firstly, it has been tried to find out the various intensities of body depending on the distance between the imaging device and human body. The point here is to detect some parameters like standard deviation and entropy, which can give us some information on the contrast of the image [39].

The second issue is the removing the background in the image. The problem here is that some pixel levels of human body are the same as the background. The segmentation of face from background and body is too difficult which can not be done with thresholding. For these reasons, a genetic algorithm is proposed based image fusion approach to fuse the enhanced visual images with the IR Images.

5.3 Enhancement of Visual Images

The ETNUD and WBNUDE algorithms were applied to 16 visual images as shown in Figures 5.14 to 5.21 under different illumination conditions. In these figures besides the regular room lights, the four extra spot lights located in the front of the person were turned off and on for creating different illumination conditions. To enhance those visual images, the luminance is first balanced, then image contrast is enhanced and finally, the enhanced image is obtained by a linear color restoration based on chromatic information contained in the original image.

The results in the luminance enhancement part showed that the algorithms work well for dark images. All the details, which cannot be seen in the original image, become evident. The experiment results have shown that for all color images, the proposed algorithms work sufficiently well.



Figure 5.14. Visual Database Enhancement for Images 1 and 2 Left Column Visual Images Right Columns Enhanced Images



Figure 5.15. Visual Database Enhancement for Images 3 and 4 Left Column Visual Images Right Columns Enhanced Images



Figure 5.16. Visual Database Enhancement for Images 5 and 6 Left Column Visual Images Right Columns Enhanced Images



Figure 5.17. Visual Database Enhancement for Images 7 and 8 Left Column Visual Images Right Columns Enhanced Images

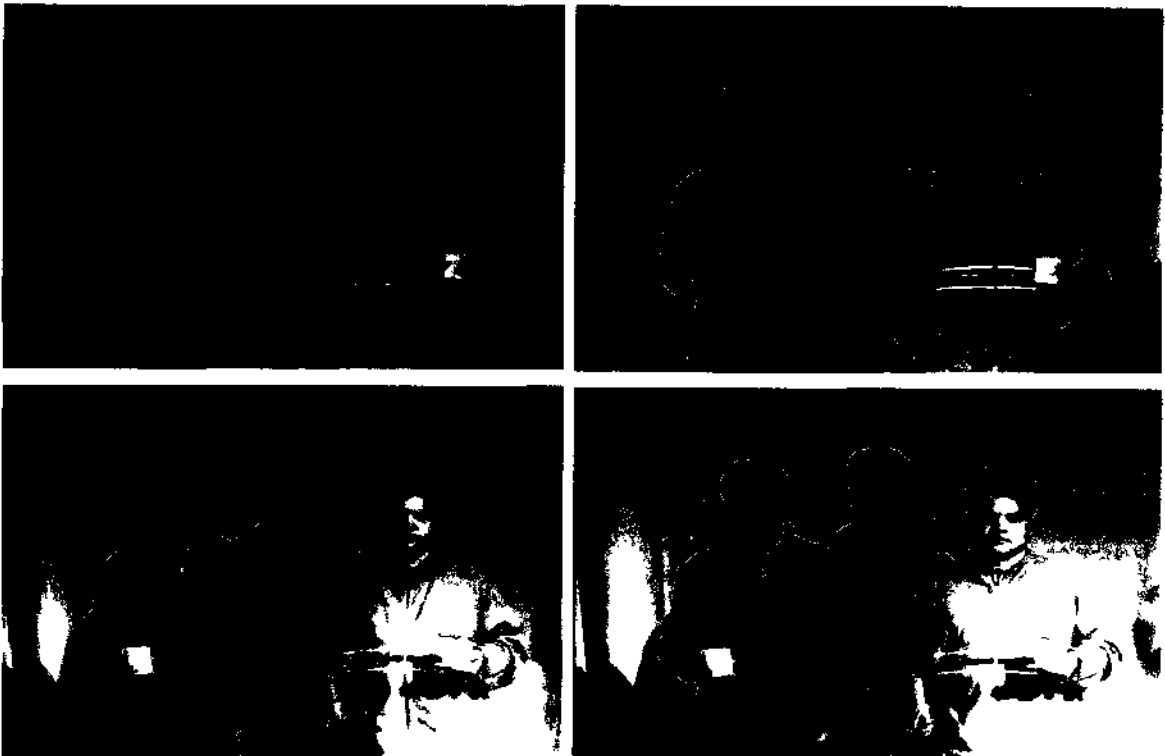


Figure 5.18. Visual Database Enhancement for Images 9 and 10 Left Column Visual Images Right Columns Enhanced Images

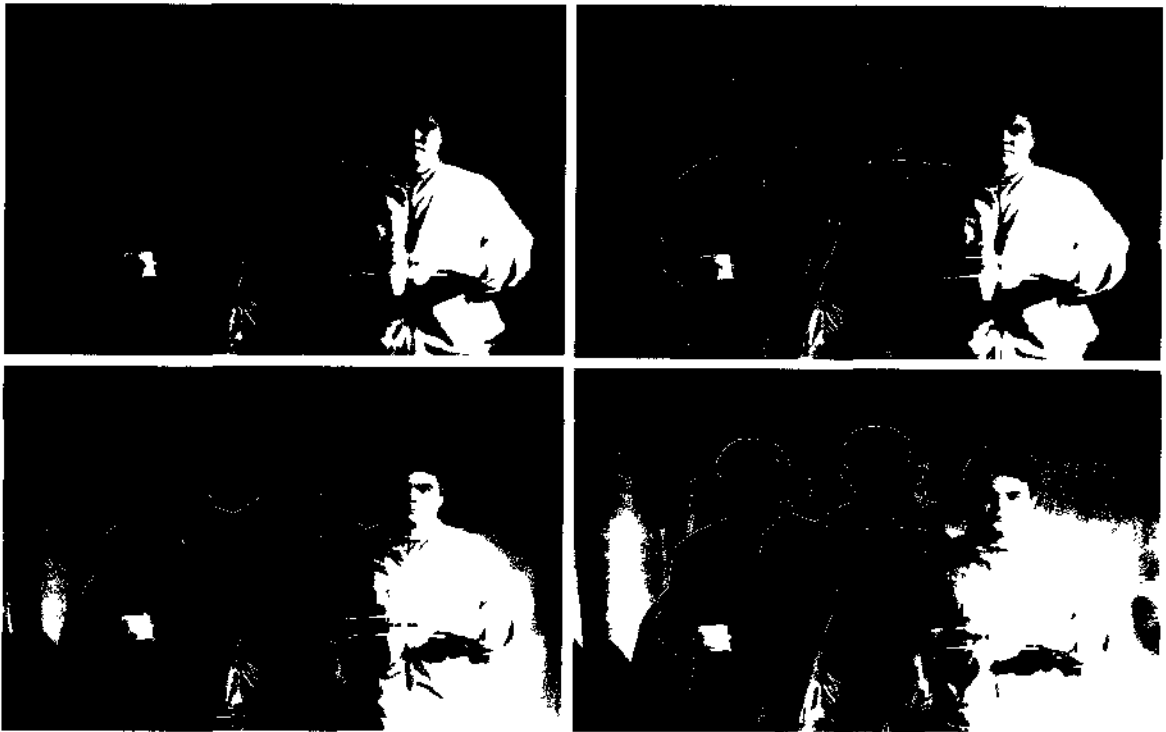


Figure 5.19. Visual Database Enhancement for Images 11 and 12 Left Column Visual Images Right Columns Enhanced Images



Figure 5.20. Visual Database Enhancement for Images 13 and 14 Left Column Visual Images Right Columns Enhanced Images



Figure 5.21. Visual Database Enhancement for Images 15 and 16 Left Column Visual Images Right Columns Enhanced Images

5.4 Harris Corner Detection

5.4.1 Introduction

In this dissertation, the corners of visual and IR images were determined by the Harris detection algorithm for registration as shown in Fig 5.22. The corners in both the visual and IR images were determined first and then a registration process was applied based on the detected corner point pairs.

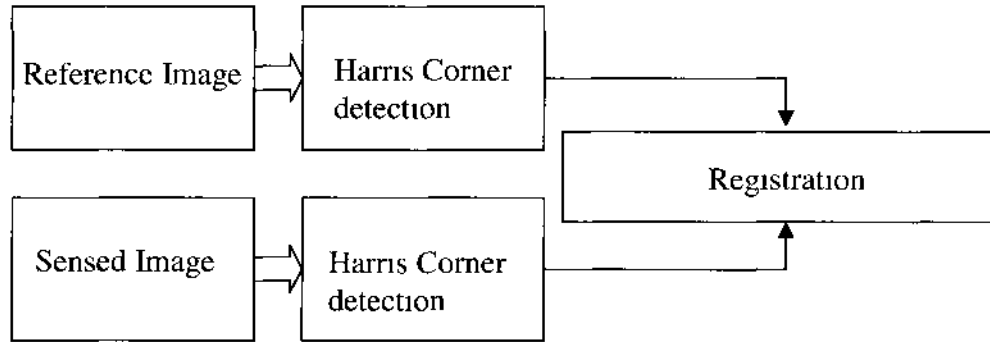


Figure 5.22. Diagram of Harris Corner Detection for Registration

5.4.2 Results

The Harris corner detector determines a matrix M that contains all differential operators and describes the geometry of the image surface at a given point (x,y) . The image intensity is denoted by I , intensity variation can be measured in any direction with Eq. 5.1 and w specifies the image window; it is unity within a specified rectangular region, and zero elsewhere.

$$A = \left(\frac{\partial I}{\partial x} \right)^2 \otimes w, B = \left(\frac{\partial I}{\partial y} \right)^2 \otimes w, C = \left(\frac{\partial I}{\partial x} \frac{\partial I}{\partial y} \right) \otimes w$$

$$M = \begin{bmatrix} A & C \\ C & B \end{bmatrix} \quad (5.1)$$

where M is the image gradient covariance matrix and measure of cornerness C at the position (x,y) is defined as

$$C(x, y) = \det(M) - k(\text{trace}(M))^2 \quad (5.2)$$

where k is constant

Local maxima of these corner “strengths” indicate potential corner positions. In the experiments, M was filtered by the maximum filter with a size of 11×11 . Then the value of each pixel in M was compared with a threshold of 100 to filter M . Figs. 5.23 and 5.24 show corner detection results for IR and visual images. Since the detection results for IR image are reasonably good, the histogram equalization technique was not applied to the IR images.

5.5 IR and Visual Images Registration

First, the IR and visual images taken from different sensors, viewpoints, times and resolution were resized for the same size. The correspondence between the features detected in the IR image and those detected in the visual image were then established. Control points were picked manually from those corners detected by the Harris corner detection algorithm from both images, where the corners were in the same positions in the two images.

In the second step, a spatial transformation was computed to map the selected corners in one image to those in another image. Once the transformation was established, the image to be registered was resampled and interpolated to match the reference image. For RGB and intensity images, the bilinear or bicubic interpolation method is

recommended since they lead to better results. In the experiments, the bicubic interpolation method was used.



Figure 5.23. The Corners of Visual and IR images. The corners have been shown with crosses.



Figure 5.24. The Corners of Visual and IR images. The corners have been shown with crosses.

The registered images were overlapped at an appropriate transparency. The pixel value in the fused image was a weighted submission of the corresponding pixels in the IR and visual images. As shown in Figure 5.25, a simple overlapping cannot improve the

image quality. In the next section, results from advanced image fusion approaches are presented.

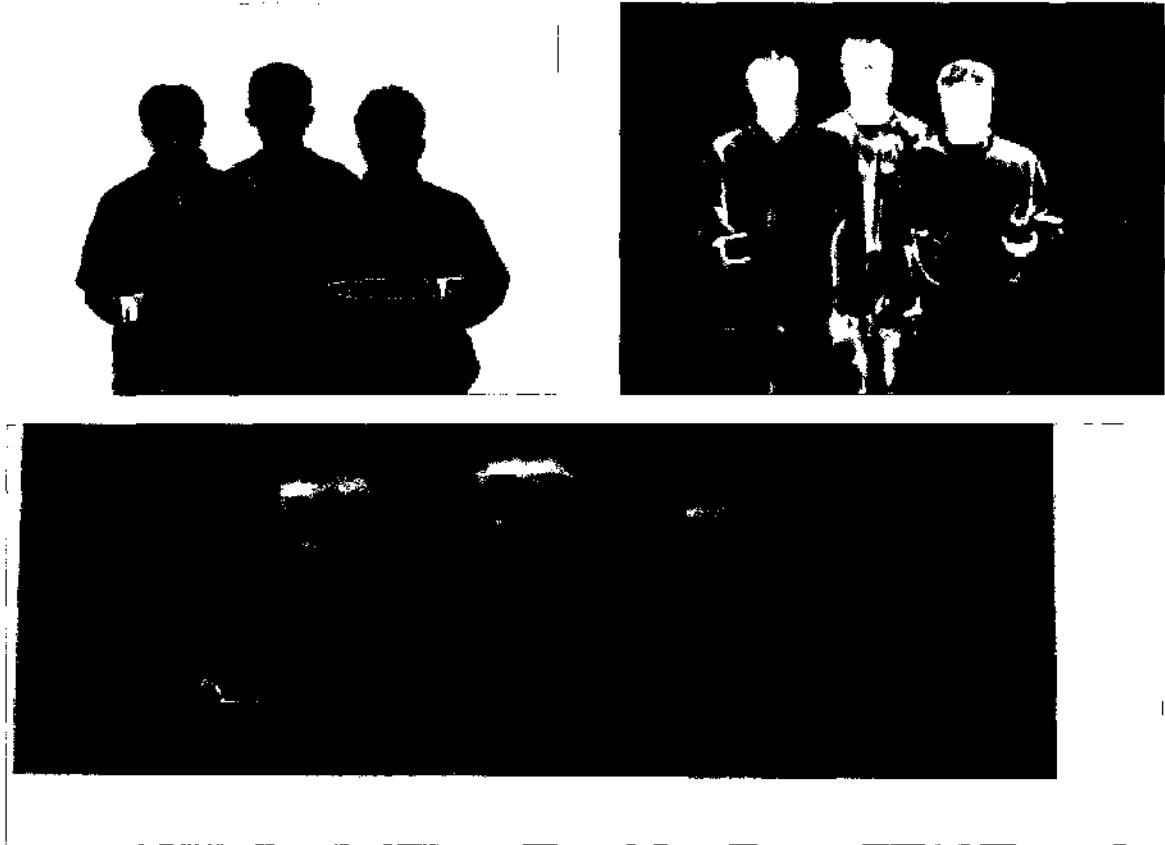


Figure 5.25. Visual, IR Image and Combined Image

5.6 Fusion of two Visual Images

In this section, image fusion results are presented for the visual images as shown in Fig. 5.26. It is obvious from the figure that the images do not need to be registered. The cost functions are very simple and defined as

$$Entropy(F = w_a A + w_b B) \quad (5.3)$$

$$Mean(F = w_a A + w_b B) \quad (5.4)$$

$$Std(F = w_a A + w_b B) \quad (5.5)$$

where A and B are the visual images, w_a and w_b are the respective associated weights, std is the standard deviation and F is the fused image. Here the three cost functions were chosen. The reason of this step is to find the best suitable cost function which gives the best result for fusion. These three cost functions will be evaluated based on the metrics which are mean, standard deviation, entropy, mutual information, information symmetry, RMSE, PSNR and image quality.

In the first step, the evaluation of the Equation 5.3, A and B images were fused four times in that the population size and number of iteration for the genetic algorithm were changed, as shown in Table 5.3. The initial population size has been selected as 10×3 , 10×3 , 100×3 , 100×3 respectively. The iteration has been selected as 10, 50, 10 and 100 respectively. The first and second columns in population matrix represent $w_a A$, and $w_b B$ and the last column represents the cost function which is the entropy of F . Then initial population has been ranked based on the chosen cost function. In each iteration of the CGA algorithm, the crossover was performed based on Equation 4.2. The mutation rate was set to 0.20, and the value of a mutated variable was replaced by the mutated value.

Figures 5.26 and 5.27 show the CGA results after 10, 50, 10 and 100 iterations of the CGA algorithm, respectively. The optimum solution was determined in the fourth trial whose population size is 100×3 after 100 iterations. It was determined that $w_a = 0.98$ and $w_b = 0.33$ provide the optimum entropy cost function for the F specified in Equation 5.3. The evaluation of these weights results is shown in Table 5.3.

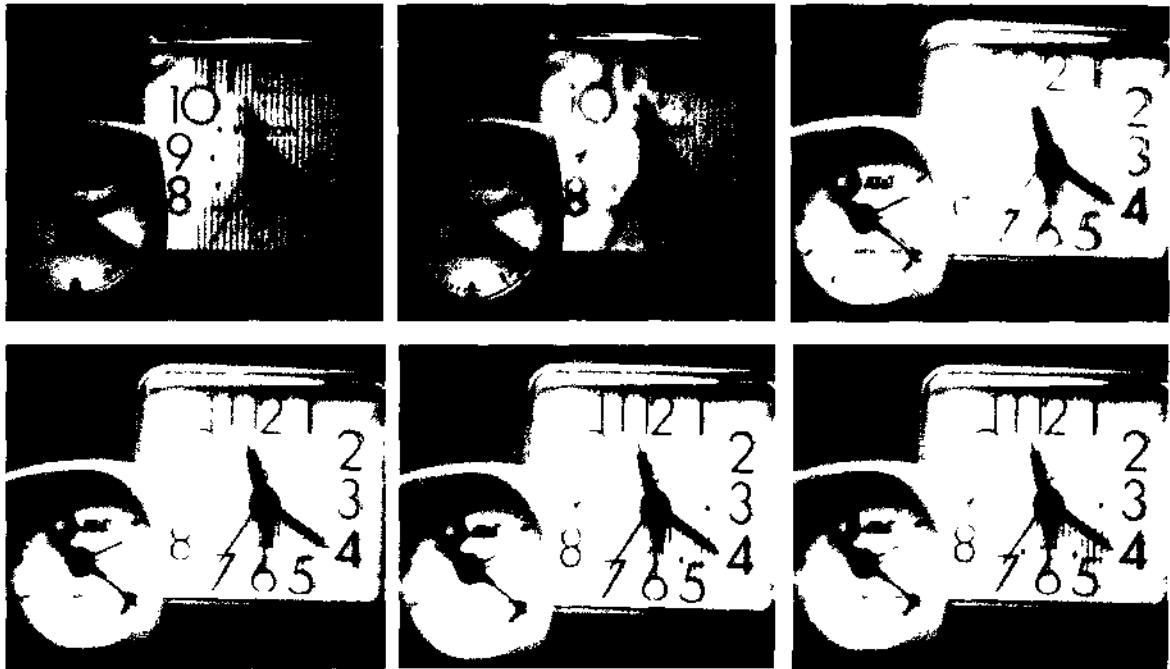


Figure 5.26. Fusion Results Left Upper Visual A Image, Middle Upper Visual B Image, Right Upper Fused Image 1, Bottom Right Fused Image 2, Bottom Middle Fused Image 3, Bottom Right Fused Image 4

To evaluate Equation 5.4, A and B images were fused three times in that the population size and number of iteration were changed, as shown in Table 5.4. The initial population sizes had been selected as 10×3 , 10×3 , 100×3 respectively. The iteration number had been selected as 10, 50, and 20 respectively. The first and second columns in population matrix represent $w_a A$, and $w_b B$ and the last column represents the cost function, which is the mean of F . Then initial population has been ranked based on the cost function. In each iteration of the CGA algorithm, the crossover has been applied based on Equation 4.2. The mutation rate was performed on the Equation 4.2. The mutation rate was set 0.20, and the value of a mutated variable was replaced by the mutated value.

Table 5.3. The Statistics of Figures 5 26

IMAGE	WEIGHTS	MEAN	STD	ENTR	MI	IS	RMSE	PSNR	IQ
A Image		102 98	8 22	7 25041					85
B Image		103 13	6 84	7 19617					87
Fused Image 1 Pop 10 Ite 10		137 33	9 34	7 5559	6 01	1 98	39 29	16 24	98
Fused Image 2 Pop 10 Ite 50	W1=0 83 W2=0 50	138 11	9 79	7 56540	6 06	1 93	40 30	16 02	98
Fused Image 3 Pop 100 Ite 10	W1=0 99 W2=0 33	137 45	9 96	7 57172	6 31	1 87	39 98	16 09	98
Fused Image 4 Pop 100 Ite 100	W1=0 98 W2=0 33	135 67	9 98	7 57458599	6 32	1 87	38 14	16 50	98

Figs 5 28 and 5 29 show the CGA results. The iteration number had been selected as 10, 50 and 20 respectively. The optimum solution was determined in the third trial whose population size is 100x3 after 20 iterations. It was determined that $w_a = 0.99$ and $w_b = 0.99$ provide the optimum values for maximizing the mean cost function for the F specified in Equation 5 3. The evaluation of these weights results is shown in Table 5 4.

To evaluate Equation 5 5, A and B images were fused three times in that the population size and number of iteration were changed, as shown in Table 5 5. The initial

population sizes had been selected as 10×3 , 50×3 , 3×3 respectively. The iteration numbers had been selected as 10, 50, and 3 respectively. The first and second columns in population matrix represent $w_a A$, and $w_b B$ and the last column represents the cost function which is the standard deviation of F . Then initial population has been ranked based on the cost function. The crossover was performed based on Equation 4.2. The mutation rate was set to 0.20, and the value of a mutated variable was replaced by the mutated value.

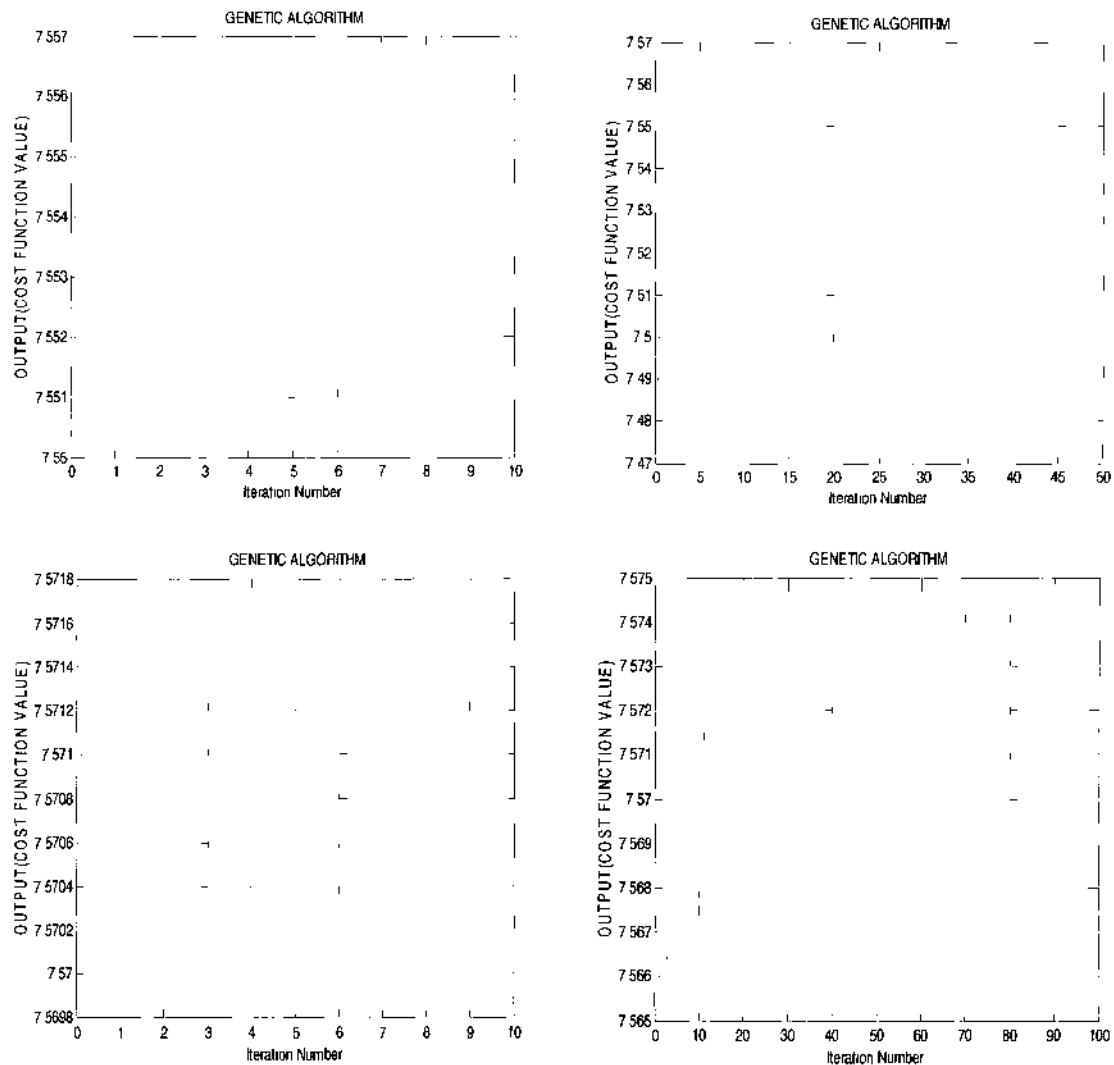


Figure 5.27. The Result of Continuous Genetic Algorithm of Table 5.3



Figure 5.28. Fusion Results Left Fused Image 1, Middle Fused Image 2, Left Fused Image 3

Table 5.4. The Statistics of Figures 5 28

IMAGE	WEIGHTS	MEAN	STD	ENTR	MI	IS	RMSE	PSNR	IQ
A Image		102.98	8.22	7.250					85
B Image		103.13	6.841	7.196					87
Fused Image 1 Pop 10 Itc 10	W 1=0.9595 W 2=0.9137	181.10	8.380	6.016	5.228	1.979	85.4	9.49	100
Fused Image 2 Pop 10 Itc 50	W 1=0.9573 W 2=0.9661	184.13	8.179	5.777	5.099	1.981	88.5	9.18	100
Fused Image 3 Pop 100 Itc 20	W 1=0.9986 W 2=0.9953	187.39	7.889	5.558	4.980	1.984	91.8	8.86	100

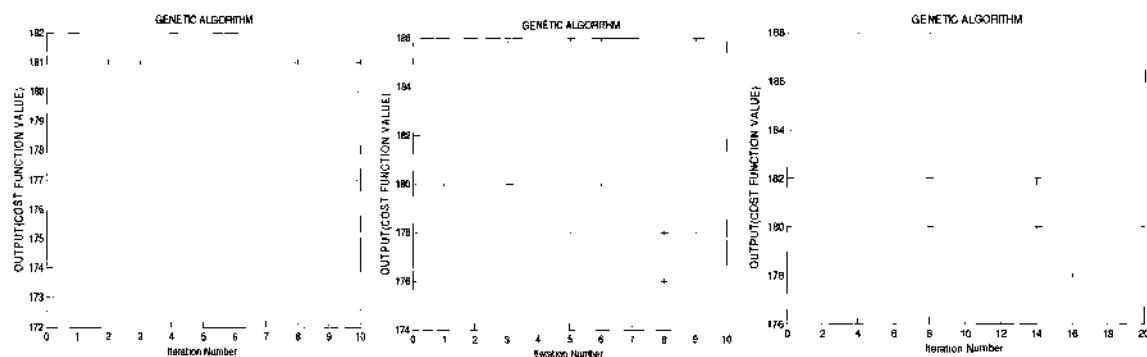


Figure 5.29. The Result of Continuous Genetic Algorithm of Table 5 4

Figures 5 30 and 5 31 shows the CGA results after 10, 50, and 3 times iterations of the GA respectively such that the CGA maximizes the cost and find optimum weights for images. The optimum solution was determined in the second trial whose population size is 100x3 after 50 iterations. It was determined that $w_a = 0.99$ and $w_b = 0.98$ provide the optimum values for maximizing the standard deviation cost function for the F specified in Equation 5 4. The evaluation of these weights results is shown in Table 5 5.

5.7 Fusion of Visual and IR Images

Figures 5 32 (f) and (g) show the result of CGA after 100 iterations. The optimum solution was determined with a population size of 100x3 after 76 iterations. It was determined that $w_a = 0.99$ and $w_b = 0.47$ are the optimum values for maximizing the entropy cost function which is 7.58 for the F specified in Equation (5 3). The evaluation of these weights results is shown in Table 5 6. By inspection, the faces and the details in the fused image are clearer as compared to either the original IR image or the visual image.

Figures 5 33 (f) and (g) show the result of CGA after 100 iterations. The optimum solution was determined with a population size of 100x3 after 12 iterations. It was determined that $w_a = 0.99$ and $w_b = 0.15$ are the optimum values for maximizing the entropy cost function which is 7.68 for the F specified in Equation (5 3). The evaluation of these weights results is shown in Table 5 7. By inspection, the faces and the details in the fused image are clearer as compared to either the original IR image or the visual image.

Table 5.5. The Statistics of Figures 5 30

IMAGE	WEIGHTS	MEAN	STD	ENTR	MI	IS	RMSE	PSNR	IQ
A Image		102 98	8 22	7 25					85
B Image		103 13	6 84	7 19					87
Fused Image 1 Pop 10 Ite 10	W 1=0 9937 W 2=0 6476	169 13	82 29	6 99	5 75	1 93	69 3	11 3	100
Fused Image 2 Pop 10 Ite 50	W 1=0 9954 W 2=0 9899	204 60	99 21	5 58	4 99	1 98	91 3	8 9	100
Fused Image 3 Pop 10 Ite 3	W 1=0 6379 W 2=0 9179	160 36	77 64	7 25	5 83	1 98	62 1	12 2	99

**Figure 5.30.** Fusion Results Left Fused Image 1, Middle Fused Image 2, Left Fused Image 3

Figures 5 34 (f) and (g) show the result of CGA after 100 iterations. The optimum solution was determined with a population size of 100x3 after 3 iterations. It was determined that $w_a = 0 58$ and $w_b = 0 59$ are the optimum values for maximizing the

entropy cost function which is 7.42 for the F specified in Equation (5.3). The evaluation of these weights results is shown in Table 5.8. By inspection, the faces and the details in the fused image are clearer as compared to either the original IR image or the visual image.

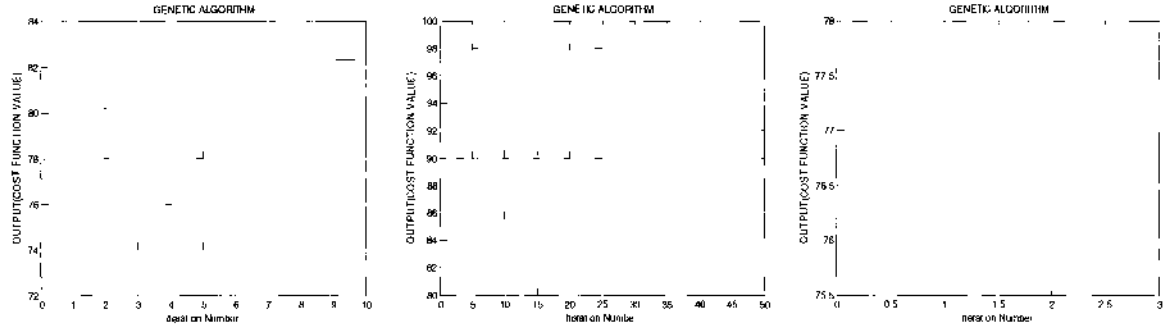


Figure 5.31. The Result of Continuous Genetic Algorithm of Table 5.5

Figures 5.35 (f) and (g) show the result of CGA after 100 iterations. The optimum solution was determined with a population size of 100x3 after 36 iterations. It was determined that $w_a = 0.73$ and $w_b = 0.36$ are the optimum values for maximizing the entropy cost function which is 7.53 for the F specified in Equation (5.3). The evaluation of these weights results is shown in Table 5.9. By inspection, the faces and the details in the fused image are clearer as compared to either the original IR image or the visual image.

Figures 5.36 (f) and (g) show the result of CGA after 100 iterations. The optimum solution was determined with a population size of 100x3 after 8 iterations. It was determined that $w_a = 0.84$ and $w_b = 0.20$ are the optimum values for maximizing the entropy cost function which is 7.82 for the F specified in Equation (5.3). The evaluation of these weights results is shown in Table 5.10. By inspection, the faces and the details in

the fused image are clearer as compared to either the original IR image or the visual image

Figures 5 37 (f) and (g) show the result of CGA after 100 iterations. The optimum solution was determined with a population size of 100x3 after 14 iterations. It was determined that $w_a = 0.89$ and $w_b = 0.09$ are the optimum values for maximizing the entropy cost function which is 7.78 for the F specified in Equation (5.3). The evaluation of these weights results is shown in Table 5.11. By inspections, the faces and the details in the fused image are clearer as compared to either the original IR image or the visual image

Figures 5 38 (f) and (g) show the result of CGA after 100 iterations. The optimum solution was determined with a population size of 100x3 after 2 iterations. It was determined that $w_a = 0.77$ and $w_b = 0.32$ are the optimum values for maximizing the entropy cost function which is 7.68 for the F specified in Equation (5.3). The evaluation of these weights results is shown in Table 5.12. By inspection, the faces and the details in the fused image are clearer as compared to either the original IR image or the visual image

Figures 5 39 (f) and (g) show the result of CGA after 100 iterations. The optimum solution was determined with a population size of 100x3 after 14 iterations. It was determined that $w_a = 0.86$ and $w_b = 0.16$ are the optimum values for maximizing the entropy cost function which is 7.83 for the F specified in Equation (5.3). The evaluation of these weights results is shown in Table 5.13. By inspection, the faces and the details in the fused image are clearer as compared to either the original IR image or the visual image

Figures 5 40 (f) and (g) show the result of CGA after 100 iterations. The optimum solution was determined with a population size of 100x3 after 76 iterations. It was determined that $w_a = 0.90$ and $w_b = 0.50$ are the optimum values for maximizing the entropy cost function which is 7.63 for the F specified in Equation (5.3). The evaluation of these weights results is shown in Table 5.14. By inspection, the faces and the details in the fused image are clearer as compared to either the original IR image or the visual image.

Figures 5 41 (f) and (g) show the result of CGA after 100 iterations. The optimum solution was determined with a population size of 100x3 after 2 iterations. It was determined that $w_a = 0.98$ and $w_b = 0.09$ are the optimum values for maximizing the entropy cost function which is 7.60 for the F specified in Equation (5.3). The evaluation of these weights results is shown in Table 5.15. By inspection, the faces and the details in the fused image are clearer as compared to either the original IR image or the visual image.

Figures 5 42 (f) and (g) show the result of CGA after 100 iterations. The optimum solution was determined with a population size of 100x3 after 17 iterations. It was determined that $w_a = 0.88$ and $w_b = 0.17$ are the optimum values for maximizing the entropy cost function which is 7.51 for the F specified in Equation (5.3). The evaluation of these weights results is shown in Table 5.16. By inspection, the faces and the details in the fused image are clearer as compared to either the original IR image or the visual image.

Figures 5 43 (f) and (g) show the result of CGA after 100 iterations. The optimum solution was determined with a population size of 100x3 after 95 iterations. It was

determined that $w_a = 0.88$ and $w_b = 0.17$ are the optimum values for maximizing the entropy cost function which is 7.66 for the F specified in Equation (5.3). The evaluation of these weights results is shown in Table 5.17. By inspection, the faces and the details in the fused image are clearer as compared to either the original IR image or the visual image.

Figures 5.44 (f) and (g) show the result of CGA after 100 iterations. The optimum solution was determined with a population size of 100x3 after 36 iterations. It was determined that $w_a = 0.83$ and $w_b = 0.27$ are the optimum values for maximizing the entropy cost function which is 7.51 for the F specified in Equation (5.3). The evaluation of these weights results is shown in Table 5.18. By inspection, the faces and the details in the fused image are clearer as compared to either the original IR image or the visual image.

Figures 5.45 (f) and (g) show the result of CGA after 100 iterations. The optimum solution was determined with a population size of 100x3 after 36 iterations. It was determined that $w_a = 0.84$ and $w_b = 0.25$ are the optimum values for maximizing the entropy cost function which is 7.60 for the F specified in Equation (5.3). The evaluation of these weights results is shown in Table 5.19. By inspection, the faces and the details in the fused image are clearer as compared to either the original IR image or the visual image.

Figures 5.46 (f) and (g) show the result of CGA after 100 iterations. The optimum solution was determined with a population size of 100x3 after 8 iterations. It was determined that $w_a = 0.64$ and $w_b = 0.46$ are the optimum values for maximizing the entropy cost function which is 7.60 for the F specified in Equation (5.3). The evaluation

of these weights results is shown in Table 5.20. By inspection, the faces and the details in the fused image are clearer as compared to either the original IR image or the visual image.

Figures 5.47 (f) and (g) show the result of CGA after 100 iterations. The optimum solution was determined with a population size of 100x3 after 4 iterations. It was determined that $w_a = 0.80$ and $w_b = 0.22$ are the optimum values for maximizing the entropy cost function which is 7.68 for the F specified in Equation (5.3). The evaluation of these weights results is shown in Table 5.11. By inspection, the faces and the details in the fused image are clearer as compared to either the IR original image or the visual image.

5.8 Discussion

Image Fusion is a powerful technique for image analysis and computer vision that can reduce errors in detection and recognition of objects by combining multisource imagery to enhance the information apparent in the images as well as to increase the reliability of interpretation. In this section, the results of an image fusion algorithm for Visual and IR Images are presented with the help of the Genetic Algorithm. Experimental results have been applied on the database, which is created by the research team. This algorithm is categorized into four steps, which are described respectively. In the first step, there is enhancement of visual images, as described in Section 5.3. The fused image should be more suitable for human visual perception and computer-processing tasks. The experience of image processing has prompted the research to consider fundamental aspects for good visual presentation of images, requiring nonlinear image enhancement techniques of visual recorded images to get a better image, which has more information

from the original images. In the second step, the corners of visual and IR images were determined with the help of Harris Detection algorithm for registration purpose to use as control points, as described in Section 5.4. In the third step, because the source images are obtained from different sensors, they present different resolution, size and spectral characteristic, the source images have to be correctly registered, as described in Section 5.5. In the last step, an image fusion process is performed, which was described in Section 5.6. Three functions were evaluated and it was decided to use the entropy cost function based with the help of the Genetic Algorithm for the fusion process of visual and IR images.

The Image fusion algorithm was applied with the help of Genetic Algorithm to the database. One of the issues is the determination of the quality of image fusion results. As part of the general theme of fusion evaluation there is a growing interest to develop methods that address the scored performance of image fusion algorithms as described in Chapter 4. Given the diversity of applications and various methods of evaluation metrics, there are still open questions concerning when to perform image fusion. There is an interest in exploring mean, standard deviation, entropy, mutual information, peak signal to noise ratio and image quality as described in Chapter 4. Because source images have different spectrum, they show quite distinct characters and have complementary information. It can be seen in Figure 5.32 (a and c) that the visual image does not have enough information to see the faces and is very dark. Figure 5.32 (b) shows that the luminance enhancement part works well for dark images and the technique adjusts itself to the image. In the contrast enhancement part it is clear that unseen or barely seen features of low contrast images were made visible. Enhancement algorithms were

developed to improve the images before the fusion process. After enhancement it was found that the corners of the enhanced image and the IR image then registered the enhanced image as shown in Figure 5.32 (d). Then, the enhanced image was fused with the IR image in Figure 5.32 (f).

The cost function defined in Equation 5.3 and the iteration selected as 100 in the experiments. The first and second columns in the population matrix represent $w_a A$, and $w_b B$ and the last column represents the cost function, which is the entropy of F . Then the initial population is ranked based on the cost function.

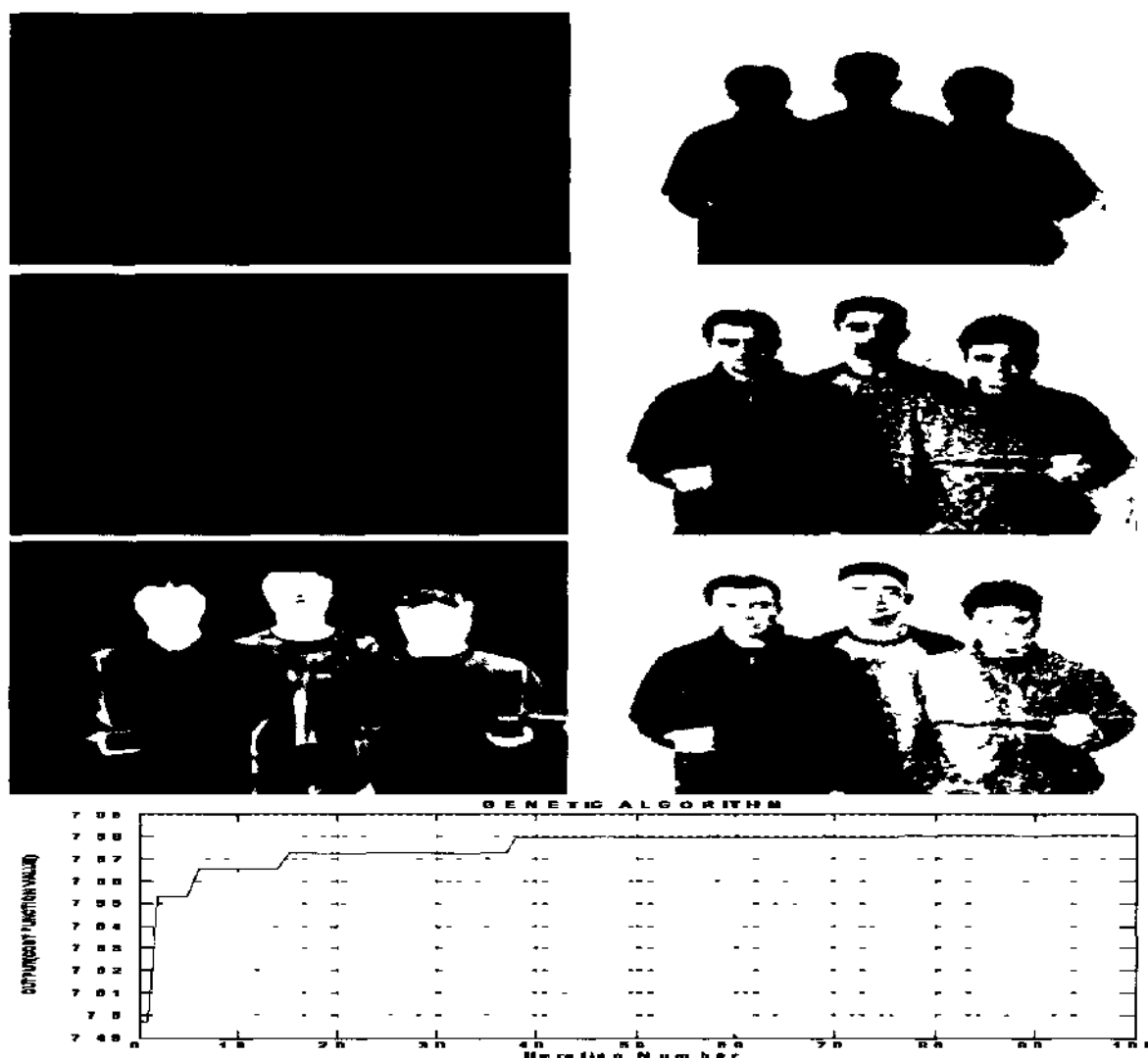


Figure 5.32. Fusion Results for Image 1 (top-left-(a)) Original, (top-right-(b)) Enhanced, (middle-left-(c)) Original, (middle-right-(d)) Enhanced, (bottom-left-(e)) IR, (bottom-right-(f)) Fused Images, Graph-Genetic Algorithm result after 100 iterations

Table 5.6. The Statistics of Figures 5 32

Figure 5 32	WEIGHTS	MEAN	STD	ENTROPY	MI	PSNR	IQ
ORIGINAL IMAGE (c)	-	36.4	6.6	6.13	-	-	16
IR IMAGE(e)	-	88.7	15.2	7.12	-	-	-
ENHANCED IMAGE(d)	-	127.5	25.2	7.48	-	-	87
FUSED IMAGE(f)	W1= 0.99 W2= 0.47	153.5	18.3	7.58	3.63	35.73	94

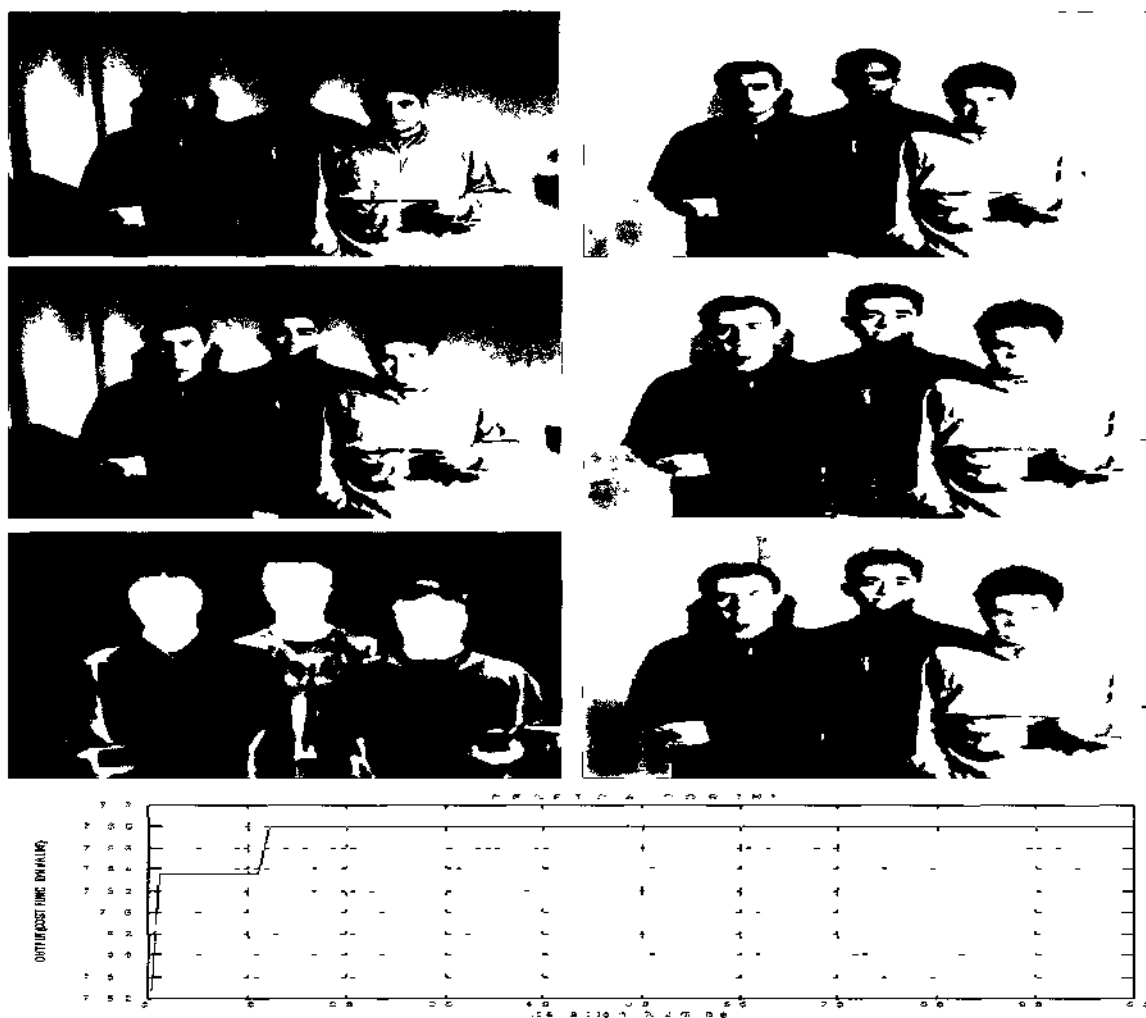


Figure 5.33. Fusion Results for Image 2 (top-left-(a)) Original, (top-right-(b)) Enhanced, (middle-left-(c)) Original, (middle-right-(d)) Enhanced, (bottom-left-(e)) IR,(bottom-right-(f)) Fused Images, Graph-Genetic Algorithm result after 100 iterations

Table 5.7. The Statistics of Figures 5 33

Figure 5 33	WEIGHTS	MEAN	STD	ENTROPY	MI	PSNR	IQ
ORIGINAL IMAGE (c)	-	109.2	11.08	7.71	-	-	86
IR IMAGE(e)	-	89.6	14.87	7.11	-	-	-
ENHANCED IMAGE(d)	-	140.17	20.75	7.60	-	-	95
FUSED IMAGE(f)	W1= 0.99 W2= 0.15	144.92	18.47	7.68	5.44	35.73	95

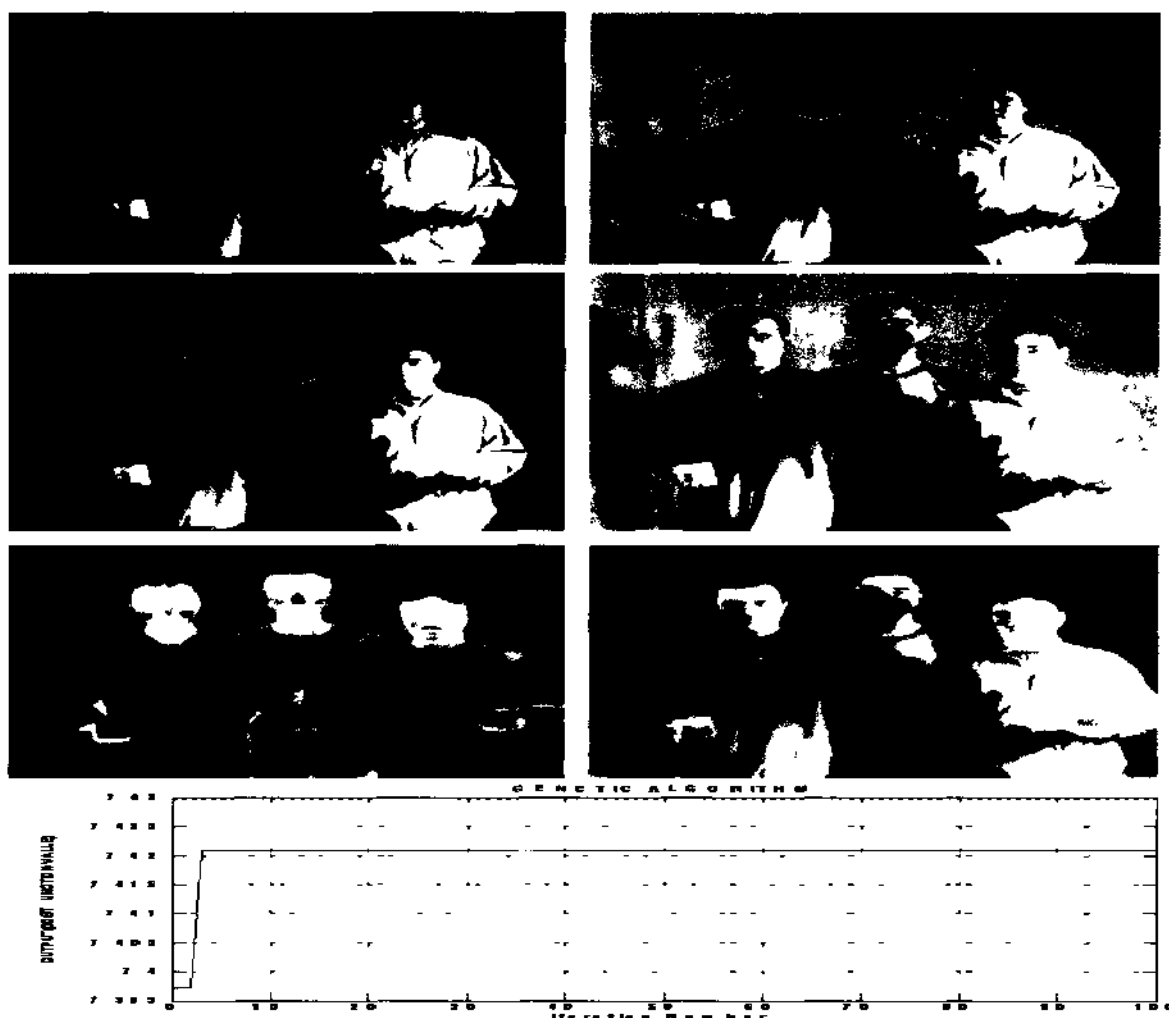


Figure 5.34. Fusion Results for Image 3 (top-left-(a)) Original, (top-right-(b)) Enhanced, (middle-left-(c)) Original, (middle-right-(d)) Enhanced, (bottom-left-(e)) IR,(bottom-right-(f)) Fused Images, Graph-Genetic Algorithm result after 100 iterations

Table 5.8. The Statistics of Figures 5 34

Figure 5 34	WEIGHTS	MEAN	STD	ENTROPY	MI	PSNR	IQ
ORIGINAL IMAGE (c)	-	89.36	23.92	7.16	-	-	84
IR IMAGE(e)	-	90.11	14.55	7.17	-	-	-
ENHANCED IMAGE(d)	-	123.98	25.60	6.96	-	-	94
FUSED IMAGE(f)	W1= 0.58 W2= 0.59	124.06	14.29	7.42	4.27	28.13	96

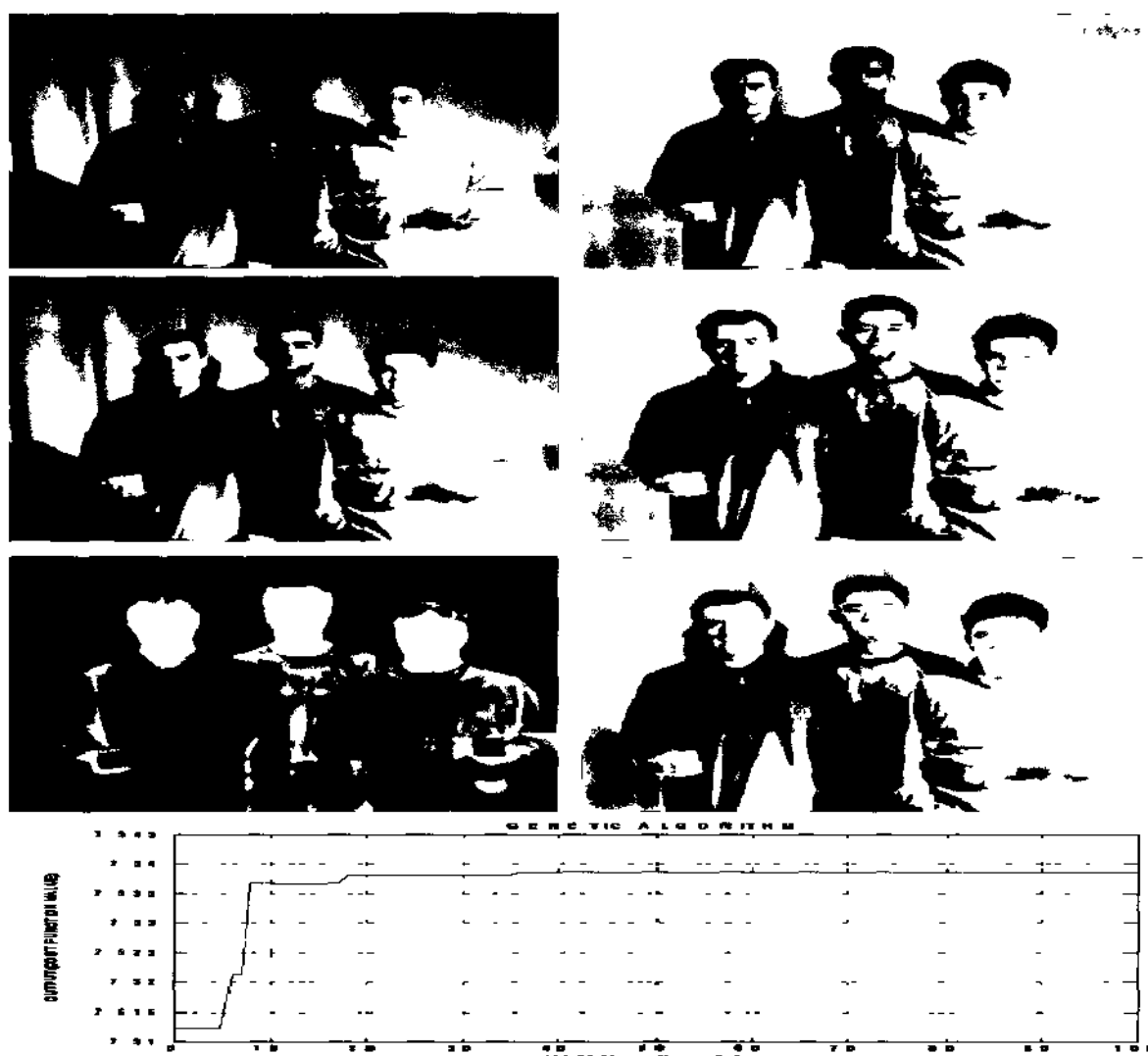


Figure 5.35. Fusion Results for Image 4 (top-left-(a)) Original, (top-right-(b)) Enhanced, (middle-left-(c)) Original, (middle-right-(d)) Enhanced, (bottom-left-(e)) IR,(bottom-right-(f)) Fused Images, Graph-Genetic Algorithm result after 100 iterations

Table 5.9. The Statistics of Figures 5 35

Figure 5 35	WEIGHTS	MEAN	STD	ENTROPY	MI	PSNR	IQ
ORIGINAL IMAGE (c)	-	122.44	14.11	7.71	-	-	95
IR IMAGE(e)	-	90.44	14.29	7.21	-	-	-
ENHANCED IMAGE(d)	-	151.51	22.04	7.51	-	-	99
FUSED IMAGE(f)	W1= 0.73 W2= 0.36	140.72	14.48	7.53	4.28	28.33	96

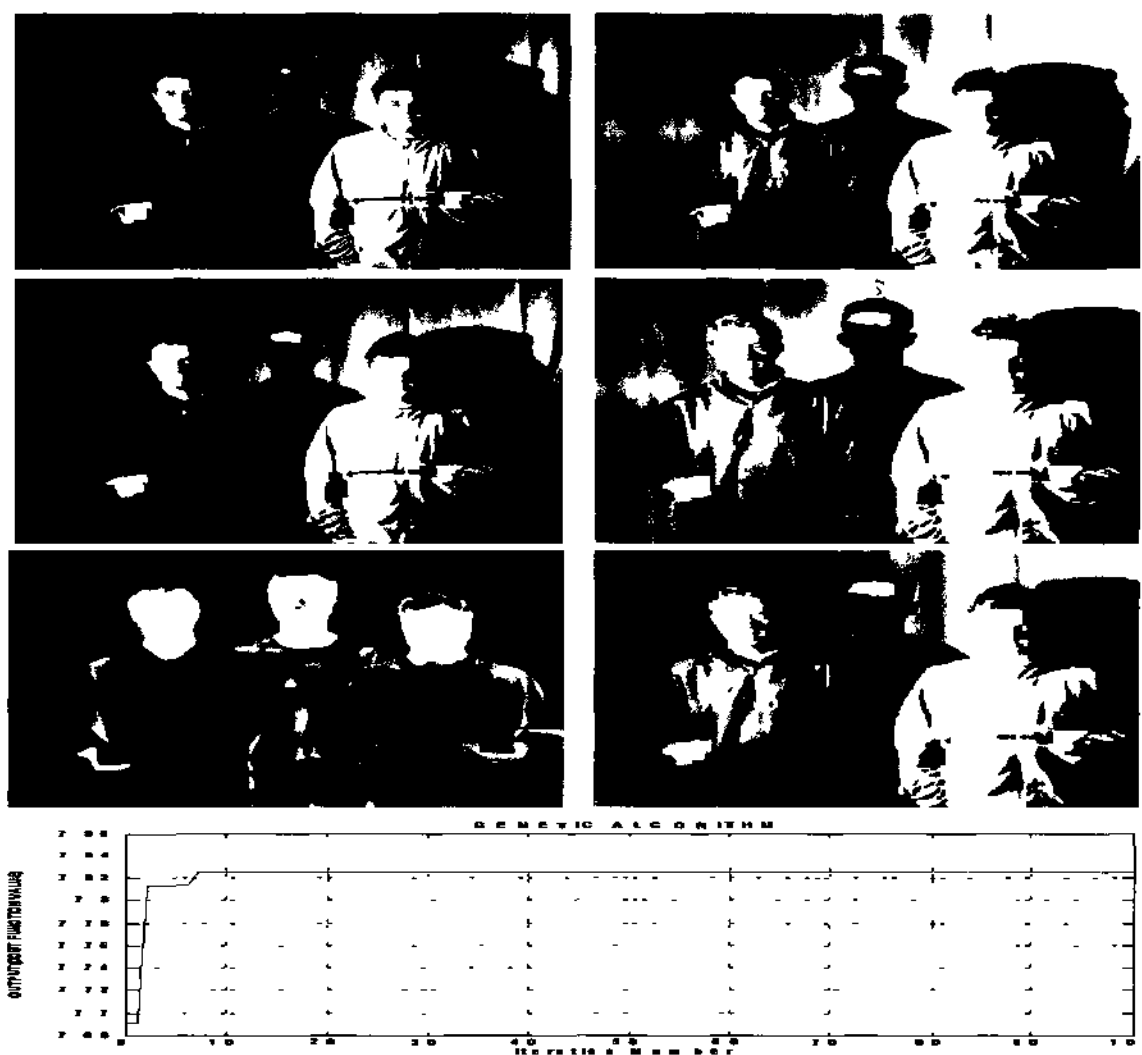


Figure 5.36. Fusion Results for Image 5 (top-left-(a)) Original, (top-right-(b)) Enhanced, (middle-left-(c)) Original, (middle-right-(d)) Enhanced, (bottom-left-(e)) IR,(bottom-right-(f)) Fused Images, Graph-Genetic Algorithm result after 100 iterations

Table 5.10. The Statistics of Figures 5 36

Figure 5 36	WEIGHTS	MEAN	STD	ENTROPY	MI	PSNR	IQ
ORIGINAL IMAGE (c)	-	87.66	20.36	7.62	-	-	74
IR IMAGE(e)	-	90.55	14.11	7.24	-	-	-
ENHANCED IMAGE(d)	-	118.41	22.23	7.57	-	-	92
FUSED IMAGE(f)	W1= 0.84 W2= 0.20	117.17	17.9	7.82	5.04	29.4	94

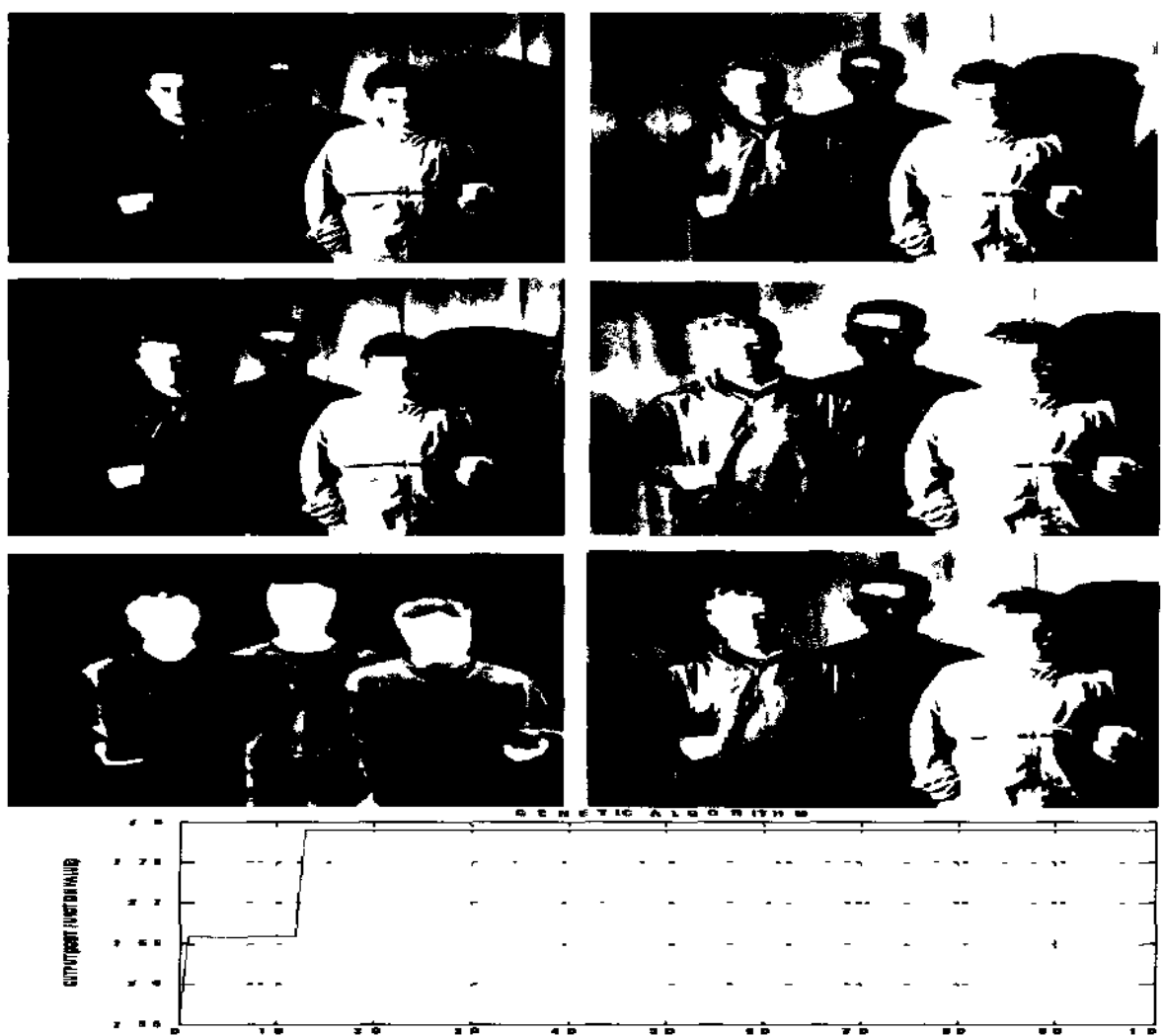


Figure 5.37. Fusion Results for Image 6 (top-left-(a)) Original, (top-right-(b)) Enhanced, (middle-left-(c)) Original, (middle-right-(d)) Enhanced, (bottom-left-(e)) IR,(bottom-right-(f)) Fused Images, Graph-Genetic Algorithm result after 100 iterations

Table 5.11. The Statistics of Figures 5 37

Figure 5 37	WEIGHTS	MEAN	STD	ENTROPY	MI	PSNR	IQ
ORIGINAL IMAGE (c)	-	92.33	20.61	7.65	-	-	80
IR IMAGE(e)	-	90.84	14.15	7.27	-	-	-
ENHANCED IMAGE(d)	-	123.07	22.59	7.61	-	-	94
FUSED IMAGE(f)	W1= 0.89 W2= 0.09	117.41	19.51	7.78	5.57	29.15	94

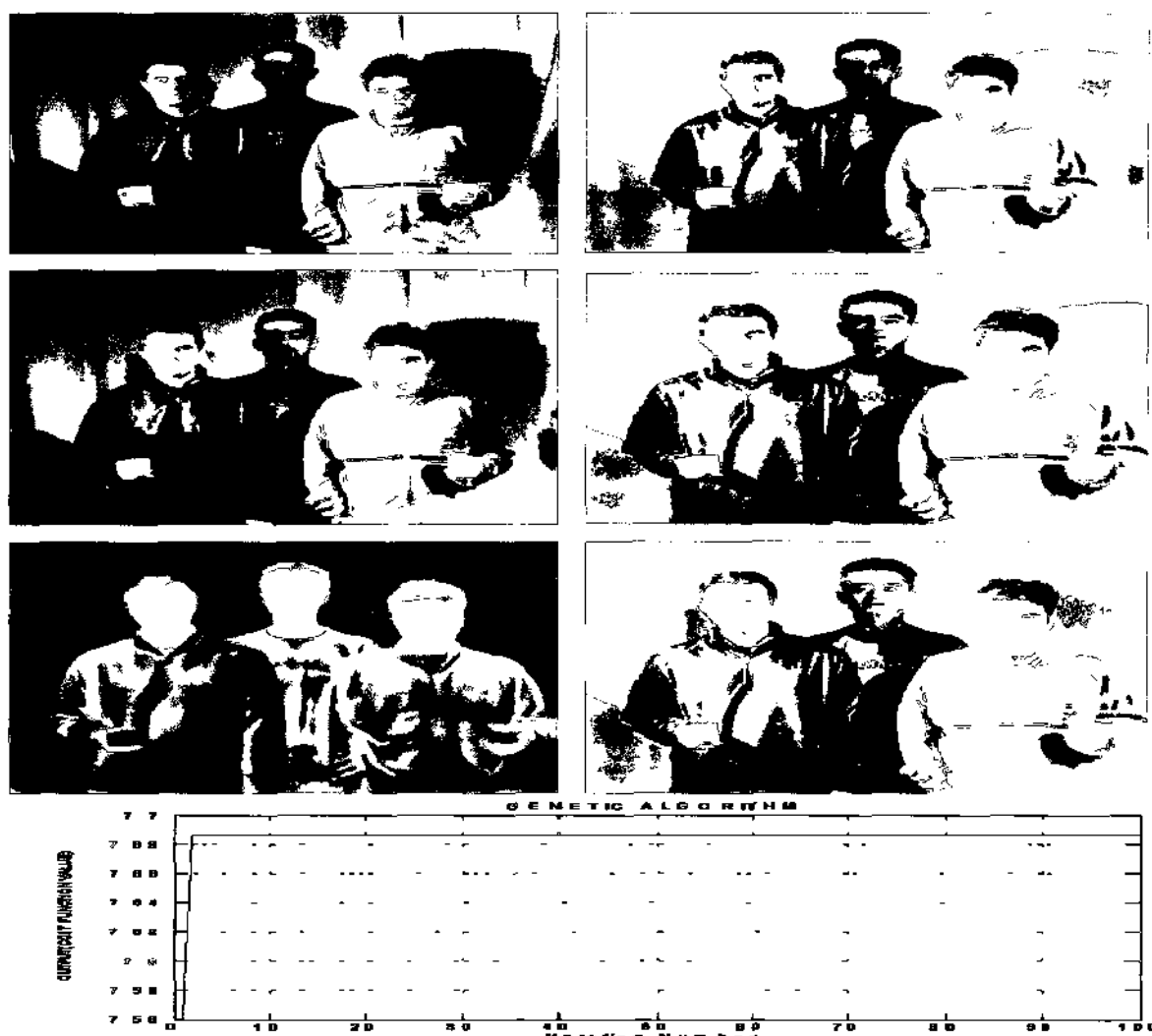


Figure 5.38. Fusion Results for Image 7 (top-left-(a)) Original, (top-right-(b)) Enhanced, (middle-left-(c)) Original, (middle-right-(d)) Enhanced, (bottom-left-(e)) IR, (bottom-right-(f)) Fused Images, Graph-Genetic Algorithm result after 100 iterations

Table 5.12. The Statistics of Figures 5 38

Figure 5 38	WEIGHTS	MEAN	STD	ENTROPY	MI	PSNR	IQ
ORIGINAL IMAGE (c)	-	107.27	16.52	7.66	-	-	93
IR IMAGE(e)	-	90.69	14.87	7.32	-	-	-
ENHANCED IMAGE(d)	-	141.67	18.47	7.71	-	-	96
FUSED IMAGE(f)	W1=0.77 W2=0.32	137.67	14.35	7.68	4.03	29.26	98

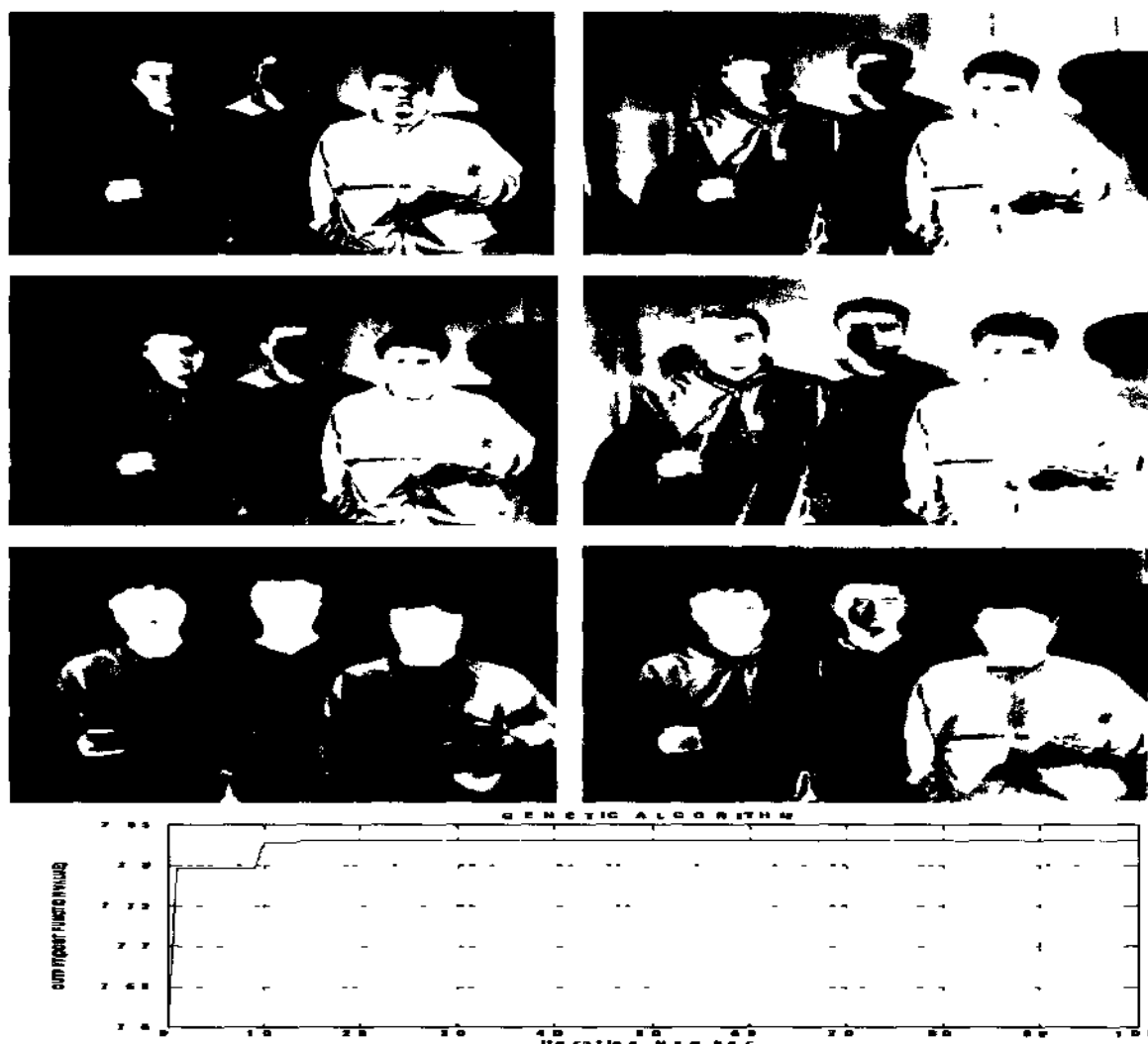


Figure 5.39. Fusion Results for Image 8 (top-left-(a)) Original, (top-right-(b)) Enhanced, (middle-left-(c)) Original, (middle-right-(d)) Enhanced, (bottom-left-(e)) IR,(bottom-right-(f)) Fused Images, Graph-Genetic Algorithm result after 100 iterations

Table 5.13. The Statistics of Figures 5 39

Figure 5 39	WEIGHTS	MEAN	STD	ENTROPY	MI	PSNR	IQ
ORIGINAL IMAGE (c)	-	107.13	19.75	7.66	-	-	89
IR IMAGE(e)	-	89.78	14.02	7.36	-	-	-
ENHANCED IMAGE(d)	-	138.82	18.75	7.67	-	-	99
FUSED IMAGE(f)	W1= 0.86 W2= 0.16	137.02	16.17	7.83	5.16	29.64	96

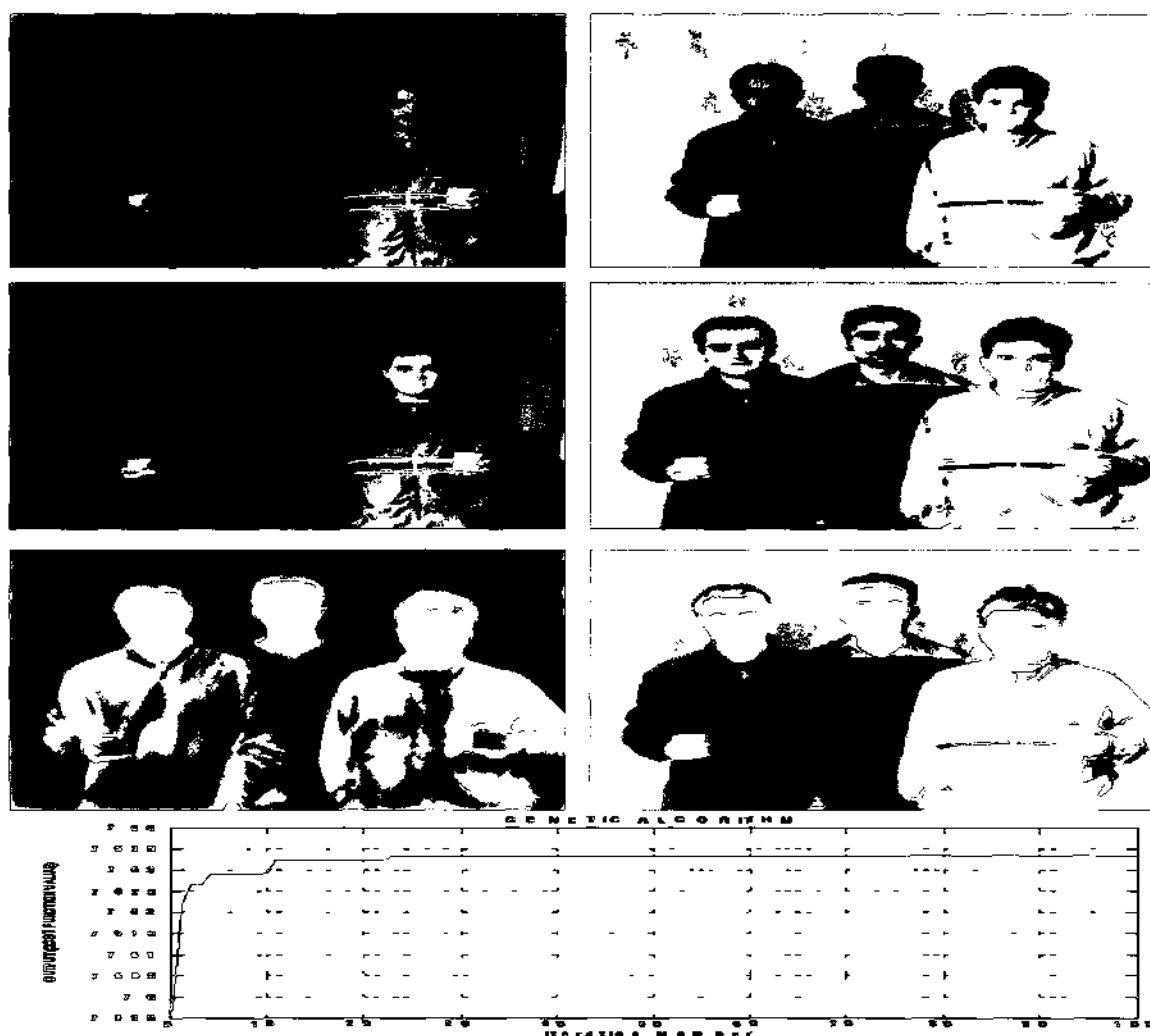


Figure 5.40. Fusion Results for Image 9 (top-left-(a)) Original, (top-right-(b)) Enhanced, (middle-left-(c)) Original, (middle-right-(d)) Enhanced, (bottom-left-(e)) IR,(bottom-right-(f)) Fused Images, Graph-Genetic Algorithm result after 100 iterations

Table 5.14. The Statistics of Figures 5 40

Figure 5 40	WEIGHTS	MEAN	STD	ENTROPY	MI	PSNR	IQ
ORIGINAL IMAGE (c)	-	57.89	9.82	6.42	-	-	54
IR IMAGE(e)	-	90.96	13.96	7.44	-	-	-
ENHANCED IMAGE(d)	-	102.23	19.15	6.25	-	-	86
FUSED IMAGE(f)	W1= 0.90 W2= 0.53	134.03	16.26	7.63	4.25	33.41	83

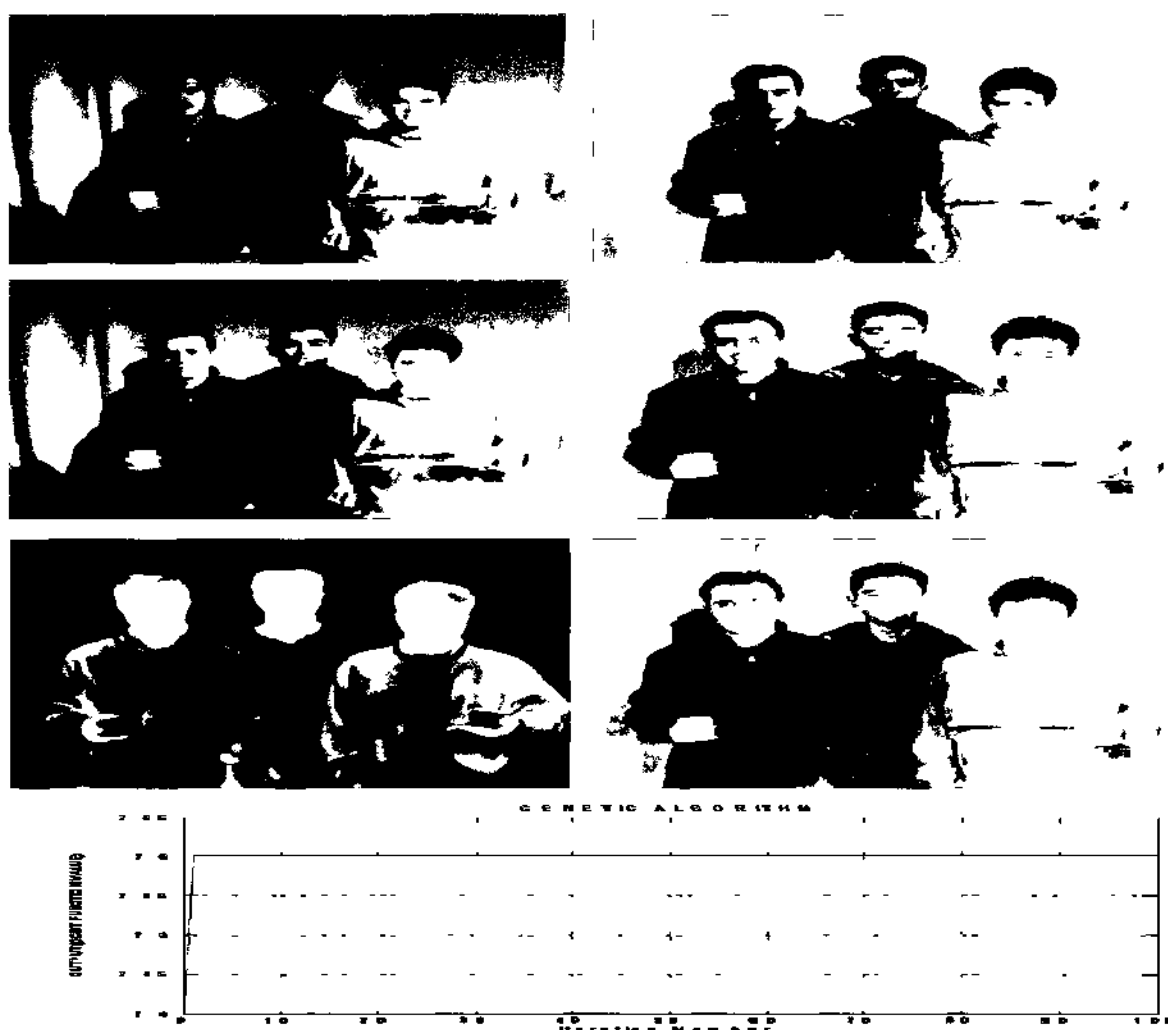


Figure 5.41. Fusion Results for Image 10 (top-left-(a)) Original, (top-right-(b)) Enhanced, (middle-left-(c)) Original, (middle-right-(d)) Enhanced, (bottom-left-(e)) IR, (bottom-right-(f)) Fused Images, Graph-Genetic Algorithm result after 100 iterations

Table 5.15. The Statistics of Figures 5 41

Figure 5 41	WEIGHTS	MEAN	STD	ENTROPY	MI	PSNR	IQ
ORIGINAL IMAGE (c)	-	119.39	12.14	7.68	-	-	84
IR IMAGE(e)	-	90.95	13.49	7.36	-	-	-
ENHANCED IMAGE(d)	-	142.34	19.89	7.35	-	-	97
FUSED IMAGE(f)	W1= 0.98 W2= 0.09	143.26	18.36	7.60	5.43	36.177	98

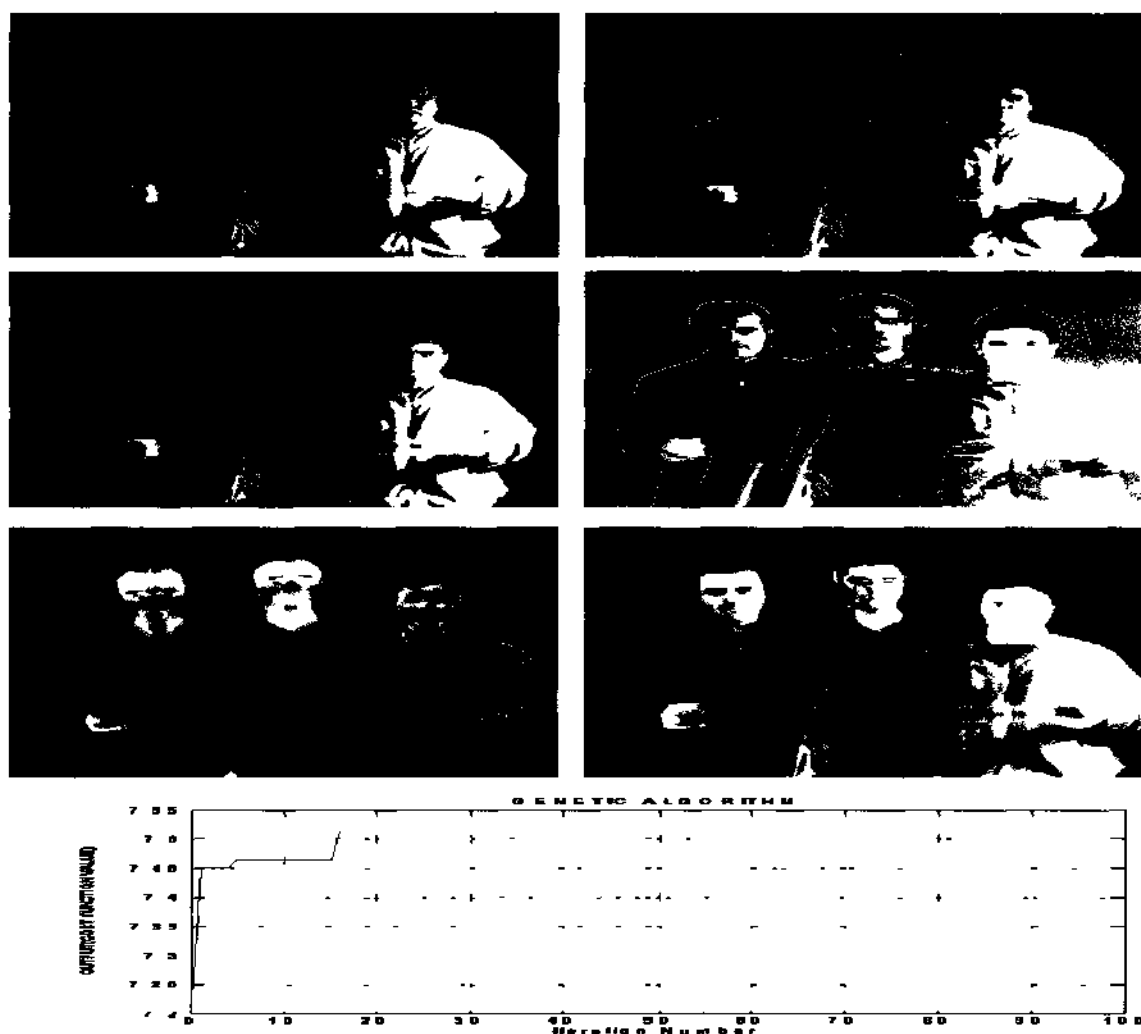


Figure 5.42. Fusion Results for Image 11 (top-left-(a)) Original, (top-right-(b)) Enhanced, (middle-left-(c)) Original, (middle-right-(d)) Enhanced, (bottom-left-(e)) IR,(bottom-right-(f)) Fused Images, Graph-Genetic Algorithm result after 100 iterations

Table 5.16. The Statistics of Figures 5 42

Figure 5 42	WEIGHTS	MEAN	STD	ENTROPY	MI	PSNR	IQ
ORIGINAL IMAGE (c)	-	99.93	21.10	7.00	-	-	89
IR IMAGE(e)	-	90.72	13.47	7.35	-	-	-
ENHANCED IMAGE(d)	-	136.43	25.87	7.34	-	-	97
FUSED IMAGE(f)	W1= 0.88 W2= 0.17	131.12	15.87	7.51	4.2	28.25	99

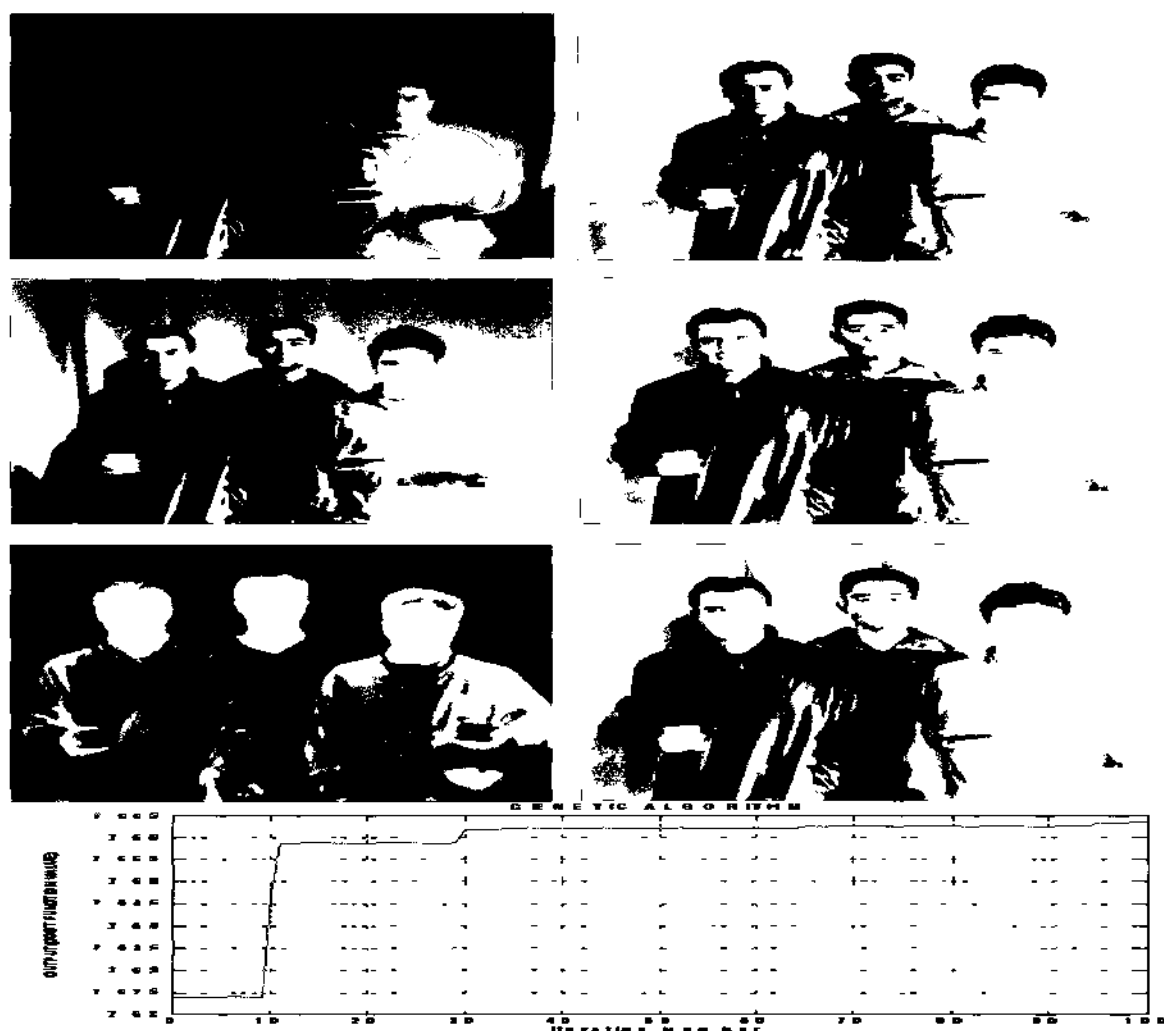


Figure 5.43. Fusion Results for Image 12 (top-left-(a)) Original, (top-right-(b)) Enhanced, (middle-left-(c)) Original, (middle-right-(d)) Enhanced, (bottom-left-(e)) IR,(bottom-right-(f)) Fused Images, Graph-Genetic Algorithm result after 100 iterations

Table 5.17. The Statistics of Figures 5 43

Figure 5 43	WEIGHTS	MEAN	STD	ENTROPY	MI	PSNR	IQ
ORIGINAL IMAGE (c)	-	120.77	14.84	7.62	-	-	92
IR IMAGE(e)	-	90.79	13.96	7.36	-	-	-
ENHANCED IMAGE(d)	-	149.24	22.43	7.41	-	-	96
FUSED IMAGE(f)	W1= 0.88 W2= 0.17	142.50	17.99	7.66	5.09	30.10	95

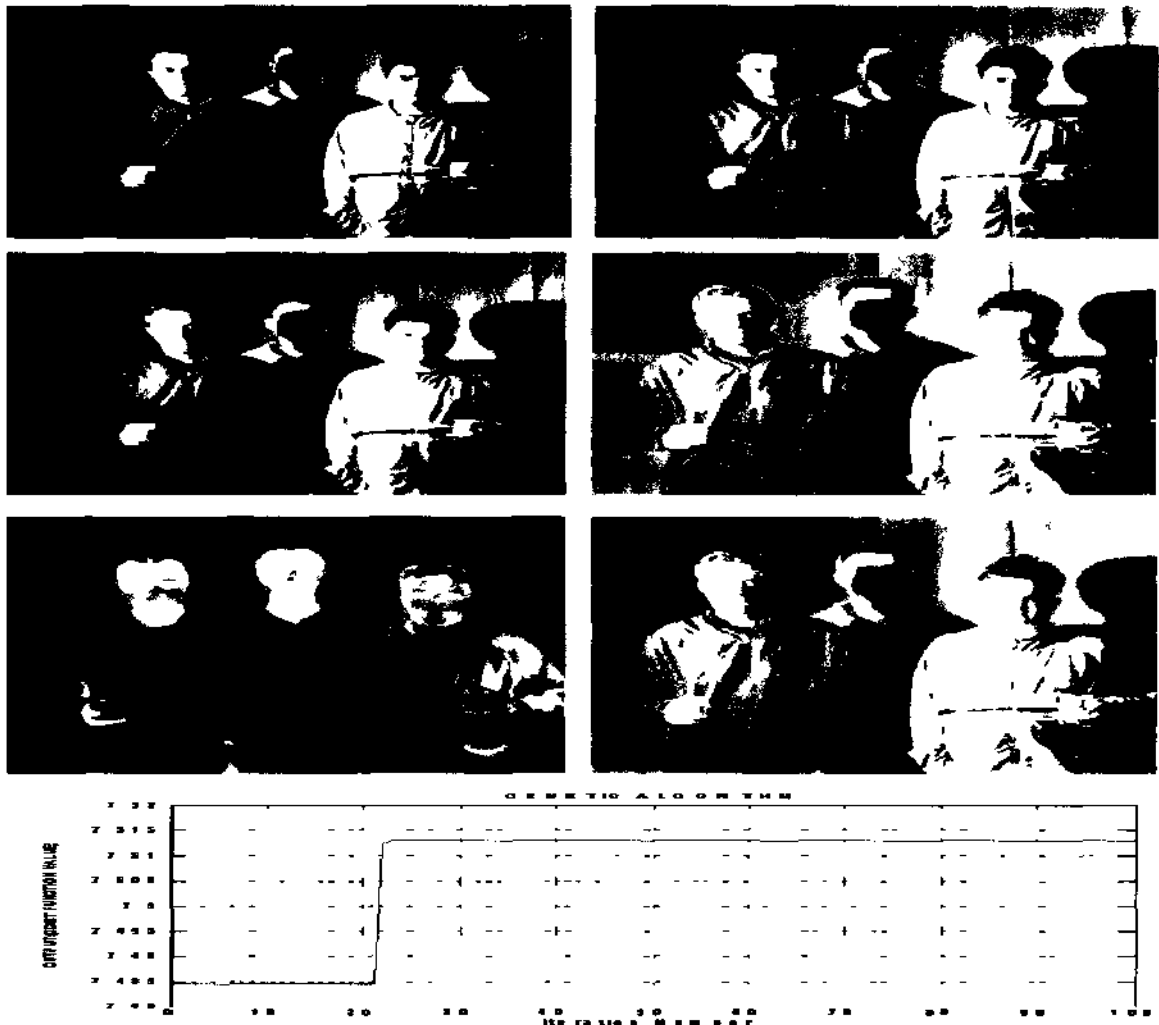


Figure 5.44. Fusion Results for Image 13 (top-left-(a)) Original, (top-right-(b)) Enhanced, (middle-left-(c)) Original, (middle-right-(d)) Enhanced, (bottom-left-(e)) IR,(bottom-right-(f)) Fused Images, Graph-Genetic Algorithm result after 100 iterations

Table 5.18. The Statistics of Figures 5 44

Figure 5 44	WEIGHTS	MEAN	STD	ENTROPY	MI	PSNR	IQ
ORIGINAL IMAGE (c)	-	102.32	21.46	7.61	-	-	87
IR IMAGE(e)	-	90.98	14.25	7.37	-	-	-
ENHANCED IMAGE(d)	-	137.41	23.87	7.38	-	-	97
FUSED IMAGE(f)	W1= 0.83 W2= 0.27	139.16	19.23	7.51	4.03	30.05	96

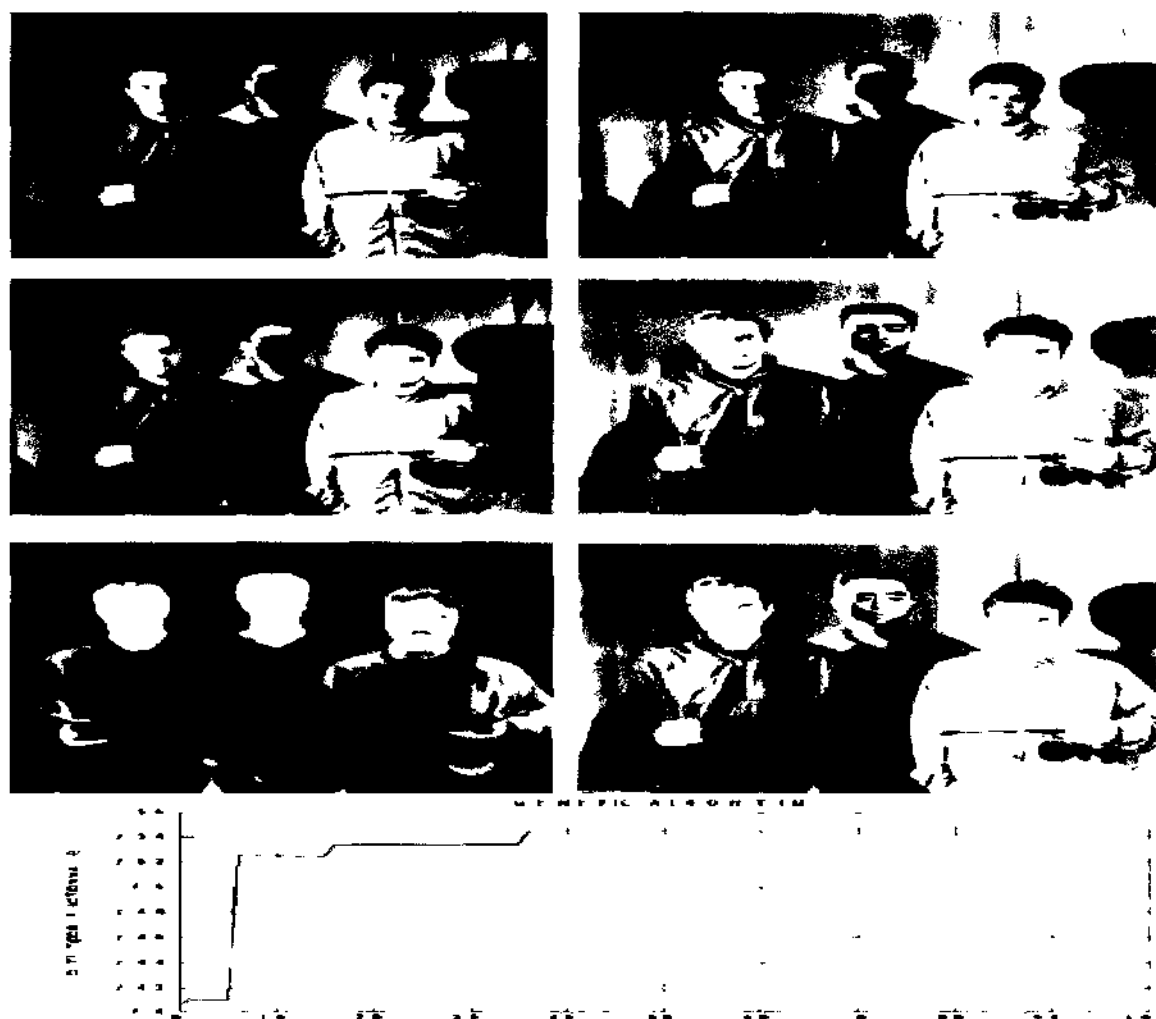


Figure 5.45. Fusion Results for Image 14 (top-left-(a)) Original, (top-right-(b)) Enhanced, (middle-left-(c)) Original, (middle-right-(d)) Enhanced, (bottom-left-(e)) IR, (bottom-right-(f)) Fused Images, Graph-Genetic Algorithm result after 100 iterations

Table 5.19. The Statistics of Figures 5 45

Figure 5 45	WEIGHTS	MEAN	STD	ENTROPY	MI	PSNR	IQ
ORIGINAL IMAGE (c)	-	112.17	17.96	7.68	-	-	92
IR IMAGE(e)	-	90.72	13.56	7.37	-	-	-
ENHANCED IMAGE(d)	-	141.40	20.34	7.40	-	-	98
FUSED IMAGE(f)	W1= 0.84 W2= 0.25	141.82	18.29	7.54	4.07	30.94	99

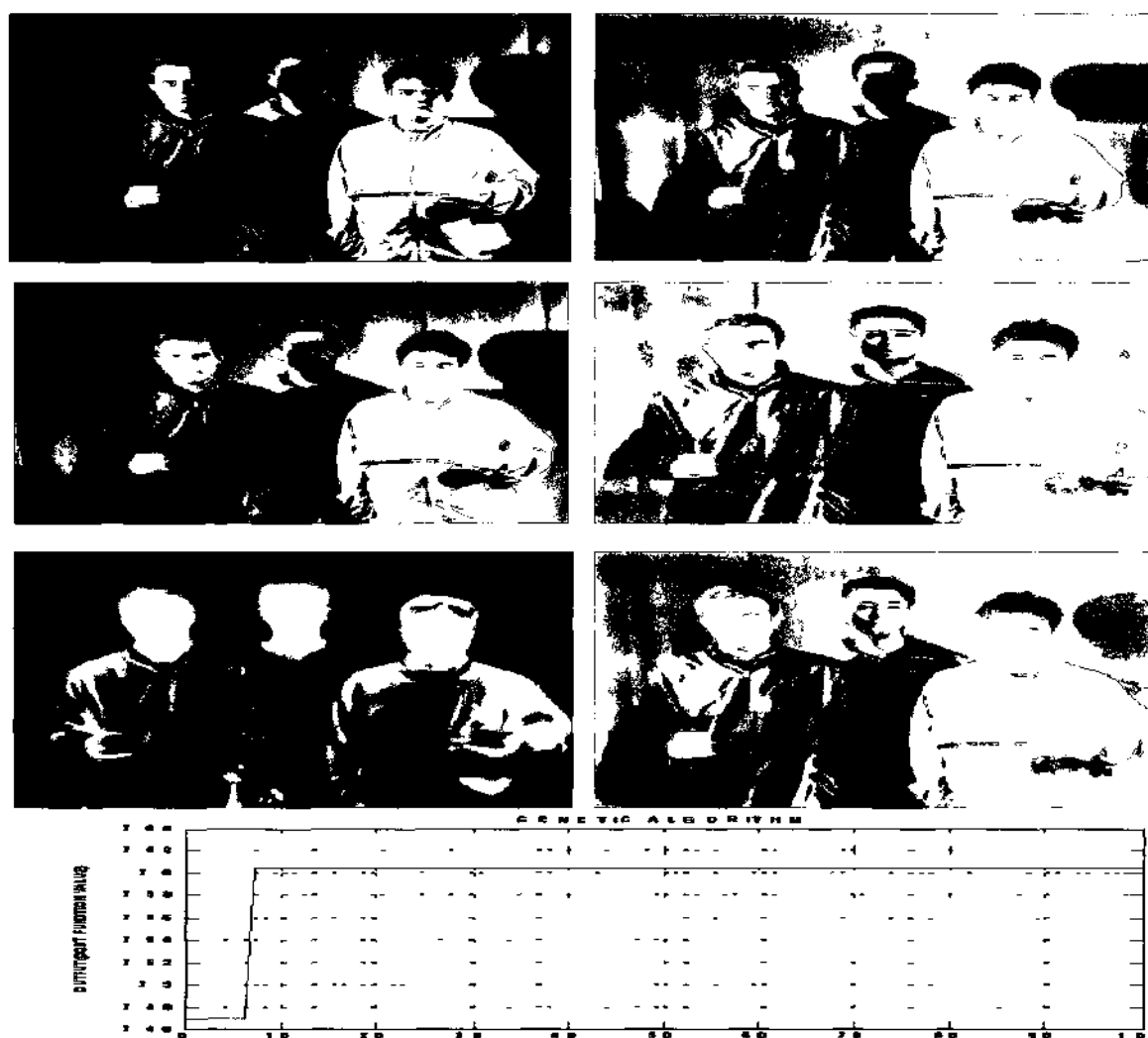


Figure 5.46. Fusion Results for Image 15 (top-left-(a)) Original, (top-right-(b)) Enhanced, (middle-left-(c)) Original, (middle-right-(d)) Enhanced, (bottom-left-(e)) IR, (bottom-right-(f)) Fused Images, Graph-Genetic Algorithm result after 100 iterations

Table 5.20. The Statistics of Figures 5 46

Figure 5 46	WEIGHTS	MEAN	STD	ENTROPY	MI	PSNR	IQ
ORIGINAL IMAGE (c)	-	102.31	23.19	7.51	-	-	85
IR IMAGE (e)	-	91.00	13.51	7.38	-	-	-
ENHANCED IMAGE (d)	-	134.33	21.41	7.54	-	-	97
FUSED IMAGE (f)	W1= 0.64 W2= 0.46	132.06	15.89	7.60	4.03	28.75	97

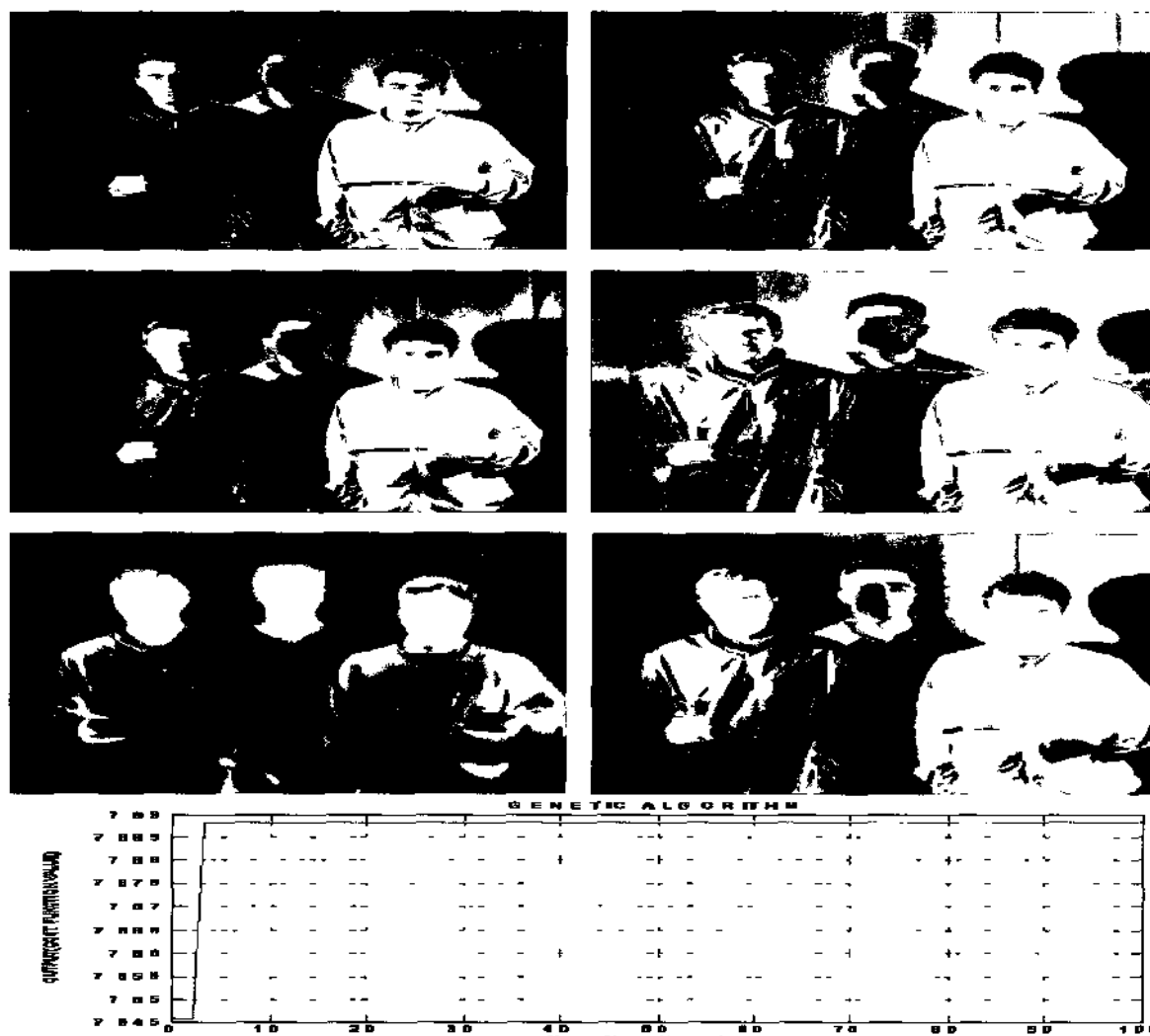


Figure 5.47. Fusion Results for Image 16 (top-left-(a)) Original, (top-right-(b)) Enhanced, (middle-left-(c)) Original, (middle-right-(d)) Enhanced, (bottom-left-(e)) IR,(bottom-right-(f)) Fused Images, Graph-Genetic Algorithm result after 100 iterations

Table 5.21. The Statistics of Figures 5 47

Figure 5 47	WEIGHTS	MEAN	STD	ENTROPY	MI	PSNR	IQ
ORIGINAL IMAGE (c)	-	111.26	19.52	7.66	-	-	94
IR IMAGE(e)	-	90.94	13.57	7.39	-	-	-
ENHANCED IMAGE(d)	-	143.79	19.79	7.51	-	-	100
FUSED IMAGE(f)	W1= 0.80 W2= 0.22	137.00	16.26	7.68	4.42	28.90	99

Table 5.22 shows the detailed comparison results of the fused images. A is the fused image by averaging the visual and IR images. B is the fused image by the proposed approach. The total images used in this experiment were from the created database. The results show that this approach is better than the averaging fusion result.

Table 5.22. The Statistics of Figures 5.32 to 5.47

Figures	MEAN		STD		ENTROPY		MI		PSNR		IQ	
	A	B	A	B	A	B	A	B	A	B	A	B
5.32	101.61	153.50	13.5	18.3	7.03	7.58	2.94	3.63	14.16	35.73	85	94
5.33	111.78	144.92	13.16	18.47	7.26	7.68	3.57	5.44	13.64	35.73	90	95
5.34	105.35	124.06	12.39	14.29	7.25	7.42	3.94	4.27	13.84	28.13	87	96
5.35	118.91	140.72	12.29	14.48	7.33	7.53	3.66	4.28	13.21	28.33	97	96
5.36	104.2	117.17	13.12	17.90	7.41	7.82	3.44	5.04	14.12	29.40	91	94
5.37	106.82	117.41	13.19	19.51	7.46	7.78	3.45	5.57	14.10	29.15	97	94
5.38	115.76	137.67	13.26	14.35	7.37	7.68	3.17	4.03	14.12	29.26	98	98
5.39	116.18	137.02	14.81	16.17	7.56	7.83	3.68	5.16	14.50	29.64	97	96
5.40	93.22	134.03	12.56	16.26	7.29	7.63	3.84	4.25	15.22	33.41	87	83
5.41	114.05	143.26	13.59	18.36	7.23	7.60	3.24	5.43	14.64	36.17	99	98
5.42	111.50	131.12	13.56	15.87	7.34	7.51	3.88	4.20	13.92	28.25	93	99
5.43	117.51	142.50	13.70	17.99	7.37	7.66	3.61	5.09	13.60	30.10	96	95
5.44	114.65	139.16	15.02	19.23	7.34	7.51	3.23	4.03	14.18	30.05	94	96
5.45	116.47	141.82	15.41	18.29	7.29	7.54	3.05	4.07	15.08	30.94	99	99
5.46	115.81	132.06	14.34	15.89	7.53	7.60	3.70	4.03	14.39	28.75	98	97
5.47	118.57	137.00	15.13	16.26	7.34	7.68	3.27	4.42	14.93	28.90	99	99

6. CONCLUSIONS AND FUTURE WORK

In this dissertation, a database for visual and thermal images was created and several techniques were developed to improve image quality as an effort to address the illumination challenge in face recognition

Firstly, two novel image enhancement algorithms were designed to improve the images' visual quality. Experimental results showed that the enhancement algorithms performed well and provided good results in terms of both luminance and contrast enhancement. In the luminance enhancement part, it has been shown that the proposed algorithms worked well for both dark and bright images. In the contrast enhancement part, it was proven that the proposed nonlinear transfer functions could make unseen or barely seen features in low contrast images clearly visible.

Secondly, the IR and enhanced visual images taken from different sensors, viewpoints, times and resolution were registered. A correspondence between an IR and a visual image was established based on a set of image features detected by the Harris Corner detection algorithm in both images. A spatial transformation matrix was determined based on some manually chosen corners and the transformation matrix was utilized for the registration.

Finally, a continuous genetic algorithm was developed for image fusion. The continuous GA has the advantage of less storage requirements than the binary GA and is inherently faster than the binary GA because the chromosomes do not have to be decoded prior to the evaluation of the cost function. In addition, three cost functions were evaluated for the fusion and decided that the entropy is a good candidate for the fusion.

Data fusion provides an integrated image from a pair of registered and enhanced visual and thermal IR images. The fused image is invariant to illumination directions and is robust under low lighting conditions. They have potentials to significantly boost the performances of face recognition systems. One of the major obstacles in face recognition using visual images is the illumination variation. This challenge can be mitigated by using infrared (IR) images. On the other hand, using IR images alone for face recognition is usually not feasible because they do not carry enough detailed information. As a remedy, a hybrid system is presented that may benefit from both visual and IR images and improve face recognition under various lighting conditions.

Future work includes further improving the quality of the fused images by finding a separate fusion weight for each of the pixels in the image pair and utilizing the fused images for face recognition. An evaluation will be presented on whether the fused images can improve face recognition especially under extreme illumination conditions.

REFERENCES

- [1] W Bowyer, K Chang and P Flynn, "A Survey Of Approaches To Three-Dimensional Face Recognition," *ICPR*, Vol 1, pp 358 – 361, 2004
- [2] S Mdhanı, J Ho, T Vetter and D J Kriegman, "Face Recognition Using 3-D Models Pose and Illumination," *Proceedings of the IEEE*, Vol 94, pp 1977 – 1999, 2006
- [3] D A Socolinsky and A Selinger, "A Comparative Analysis of Face Recognition Performance with Visible and Thermal Infrared Imagery," *IEEE International Conference of Pattern Recognition*, Vol 4, pp 217 –222, 2002
- [4] http://coolcosmos.ipac.caltech.edu/cosmic_classroom/ir_tutorial/what_is_ir.html, accessed on April 2010
- [5] FLIR Infrared Camera Systems, [[http //www flir com](http://www.flir.com)], accessed on June 2009
- [6] [http //mivim gel ulaval ca/imgs/figs/Figure_001big gif](http://mivim.gel.ulaval.ca/imgs/figs/Figure_001big.gif), accessed on July 2010
- [7] F Prokoski, "History, Current Status, and Future of Infrared Identification," *Computer Vision Beyond the Visible Spectrum Methods and Applications, Proceedings IEEE Workshop*, pp 5-14, 2000
- [8] G S Kong, J Heo, B R Abidi, J Paik and M A Abidi, "Recent Advances in Visual and Infrared Face recognition—a Review," *Computer Vision and Image Understanding*, Vol 1, pp 103-135, 2005
- [9] W F Schreiber, "Image processing for quality improvement," *Proceedings of the IEEE*, Vol 66, pp 1640–1651, 1978

- [10] E Land and J Mc Cann, "Lightness and Retinex Theory," *J Opt Soc Am*, pp 61, 1971
- [11] E Land, "Recent Advances in Retinex Theory and Some Implications for Cortical Computations," *Proc Natl Acad Sci USA*, pp 5163-5168, 1983
- [12] D J Jobson and G A Woodell, "Properties of a Center/Surround Retinex Part two Surround Design," *NASA Technical Memorandum 110188, Langley Research Center, Hampton, VA*, August 1995
- [13] D J Jobson, Z Rahman and G A Woodell, "A Multiscale Retinex for Bridging the Gap Between Color Images and the Human Observation of Scenes," *IEEE Transactions on Image Processing*, Vol 6, July 1997
- [14] D J Jobson, Z Rahman and G A Woodell, "Properties and Performance of a Center/Surround Retinex," *IEEE Transactions on Image Processing*, Vol 6, March 1997
- [15] Z Rahman, "Properties of a Center/Surround Retinex Part one Signal Processing Design," *NASA Contractor Report, Langley Research Center, Hampton, VA*, August 1995
- [16] L Tao, "An Adaptive and Integrated Neighborhood Dependent Approach for Nonlinear Enhancement of Color Images," *SPIE Journal of Electronic Imaging*, pp 11-14, 2005
- [17] L Tao, R Tompkins and V K Asari, "An Illuminance-Reflectance Model for Nonlinear Enhancement of Color Images," *Proceedings of the IEEE Computer Society Conference on Computer Vision and Pattern Recognition*, 2005

- [18] R C Gonzalez, R E Woods and S L Eddins, "Digital Image Processing," *Pearson Education, Inc Prentice Hall*, 2004
- [19] L M G Fonseca and B S Manjunath, "Registration Techniques for Multisensor Remotely Sensed Imagery," *Photogrammetric Engineering & Remote Sensing*, Vol 62, pp 1049-1056, 1996
- [20] [http //www fas hcmut edu vn/webh10/Baocao/PDF/TDLinh-MIRegistration pdf](http://www.fas.hcmut.edu.vn/webh10/Baocao/PDF/TDLinh-MIRegistration.pdf), accessed on March 2010
- [21] J B A Maintz and M A Viergever, "A Survey of Medical Image Registration," *Medical Image Analysis*, Vol 2, pp 1–37, 1998
- [22] B Zitova and J Flusser, "Image Registration Methods A Survey," *Image and Vision Computing* 21, pp 977–1000, 2003
- [23] Yan H and Liu J, "Robust Phase Correlation Based Feature Matching for Image Co-Registration and Dem Generation," *The Xxi Congress Of International Society For Photogrammetry And Remote Sensing, Beijing, The Organizing Committee Of The Xxi Congress Of International Society For Photogrammetry And Remote Sensing*, pp 1751-1756, 2008
- [24] H S Ranganath and S G Shiva, "Correlation Of Adjacent Pixels For Multiple Image Registration," *IEEE Transactions on Computers*, Vol C-34, July 1985
- [25] [Http //Web Uvic Ca/~Dsorrent/Projects/Optregistration Pdf](Http://Web.Uvic.Ca/~Dsorrent/Projects/Optregistration.Pdf)
- [26] K B Kim, J S Kim and J S Choi, "Fourier Based Image Registration for Sub-Pixel using Pyramid Edge Detection and Line Fitting," *First International Conference on Intelligent Networks and Intelligent Systems*, pp 535 – 538, 2008
- [27] [Http //Www Ie Itecr Ac Cr/Rpereira/Mat_Ant/Genetic%20algorithms/Ch1 Pdf](Http://Www.Ie.Itecr.Ac.Cr/Rpereira/Mat_Ant/Genetic%20algorithms/Ch1.Pdf),

accessed on May 2009

- [28] J H Holland, "Adaptation In Natural and Artificial Systems," *University of Michigan Press*, 1975
- [29] G Karkavitsas, And M Rangoussi,
"Http //Www Waset Org/Journals/Waset/V2/V2-2 Pdf"
- [30] S K Mitra, C A Murthy and M K Kundu, "Technique for Fractal Image Compression using Genetic Algorithm," *IEEE Trans Image Process* pp 586-93, 1998
- [31] M Srinivas and L M Patnaik, "Genetic Algorithms a Survey," pp 17 – 26, Vol 27, Jun 1994
- [32] J Zhang, X Feng, B Song, M Li and Y Lu, "Multi-Focus Image Fusion using Quality Assessment of Spatial Domain And Genetic Algorithm," *Human System Interactions*, pp 71 – 75, 25-27 May 2008
- [33] L Yu, T Yung, K Chan, Y Ho and Y Ping Chu, "Image Hiding with an improved Genetic Algorithm and an Optimal Pixel Adjustment Process," *Eighth International Conference On Intelligent Systems Design And Applications*, 2008
- [34] C Rongyuan, L Shuang, Y Ran and Q Qianqing, "Multi-Focus Images Fusion Based on Data Assimilation and Genetic Algorithm," *International Conference On Computer Science and Software Engineering*, 2008
- [35] Http //Www Ie Itcr Ac Cr/Rpereira/Mat_Ant/Genetic%20algorithms/Ch3 Pdf,
accessed on February 2009

- [36] D Patnaik, "Biomedical Image Fusion using Wavelet Transforms and Neural Network," *IEEE International Conference on Industrial Technology*, pp 1189 – 1194, 2006
- [37] Z Wang, D Ziou, C Armenakis, D Li and Q Li, "A Comparative Analysis of Image Fusion Methods," *IEEE Transactions On Geosciences And Remote Sensing*, Vol 43, pp 1391 – 1402, June 2005
- [38] F Sun, S Li and B Yang, "A New Color Image Fusion Method for Visible and Infrared Images," *International Conference On Robotics And Biomimetic*, December 15 -18, 2007,
- [39] Z Xue and R S Blum, "Fusion Of Visual And IR Images For Concealed Weapon Detection," In *Proc 5th Int Conf Information Fusion*, Jul 2002, pp 1198–1205
- [40] H Wang, "Multisensory Image Fusion by using Discrete Multiwavelet Transform," *The Third International Conference on Machine Learning and Cybernetics, Shanghai*, 26-29 August 2004
- [41] A Mumtaz and A Majid, "Genetic Algorithms and its application to Image Fusion," *International Conference On Emerging Technologies ICET*, 2008
- [42] S Erkanlı and Zia-Ur Rahman, "Entropy Based Image Fusion With the help of Continuous Genetic Algorithm," *IEEE ISDA Conference, December 2010*
- [43] Dasarthy, "Decision Fusion," IEEE Computer Society Press, 2004
- [44] K Kannan and S Perumal, "Optimal Decomposition Level of Discrete Wavelet Transform for Pixel Based Fusion of Multi-Focused Images," *International Conference On Computational Intelligence And Multimedia Applications*, 2007

- [45] A Wang, H Sun and Y Guan, "The Application of Wavelet Transform to Multi-Modality Medical Image Fusion," *Networking, Sensing and Control, ICNSC Proceedings Of The 2006 IEEE International Conference*, pp 270-274, 2006
- [46] S Erkanlı and Zia-Ur Rahman, "Enhancement Technique for Uniformly and Non-Uniformly Illuminated Dark Images," *ISDA 2010, Cairo, Egypt*, 2010
- [47] H Kolb, "How the Retina works," *American Scientist*, Vol 91, 2003
- [48] S Erkanlı and Zia-Ur Rahman, "Wavelet Based Enhancement for Uniformly and Non-Uniformly Illuminated Dark Images," *ISDA 2010, Cairo, Egypt*, 2010
- [49] L Tao, R C Tompkins, and K V Asari, "An Illuminance Reflectance Model For Nonlinear Enhancement Of Video Stream For Homeland Security Applications," *IEEE International Workshop on Applied Imagery and Pattern Recognition, AIPR*, October 19 -21, 2005
- [50] D J Jobson, Z Rahman and G A Woodell, "Properties and Performance of a Center/Surround Retinex," *IEEE Trans Image Processing*, Vol 6, pp 451-462, 1997
- [51] Z Rahman, D Jobson and G A Woodell, "Multiscale Retinex For Color Image Enhancement," *In Proceedings of the IEEE International Conference On Image Processing*, 1996
- [52] Z Rahman, D Jobson and G A Woodell, "Multiscale Retinex For Color Rendition And Dynamic Range Compression," *In Applications Of Digital Image Processing XIX, A G Tescher, Ed , Proc SPIE 2847*, 1996
- [53] D Jobson, Z Rahman and G A Woodell, "Retinex Image Processing Improved Fidelity for Direct Visual Observation," *In Proceedings Of The IS&T Fourth*

- Color Imaging Conference Color Science, Systems, and Applications*, pp 124-126, 1996
- [54] D J Jobson, Z Rahman and G A Woodell, "A Multi-Scale Retinex for Bridging the Gap Between Color Images and The Human Observation of Scenes," *IEEE Transactions on Image Processing Special Issue On Color Processing* 6, pp 965-976, July 1997
 - [55] Z Rahman, G A Woodell and D Jobson, "A Comparison of The Multiscale Retinex with other Image Enhancement Techniques," *In Proceedings Of The IS&T 50th Anniversary Conference*, pp 426-431, 1997
 - [56] Z Rahman, D Jobson and G A Woodell, "Resiliency of The Multiscale Retinex Image Enhancement Algorithm," *In Proceedings of The IS&T Sixth Color Imaging Conference Color Science, Systems, and Applications*, pp 129-134, 1998
 - [57] D Jobson, Z Rahman and G A Woodell, "Spatial Aspect of Color and Scientific Implications of Retinex Image Processing," *In Visual Information Processing X, S K Park, Z Rahman, And R A Schowengerdt, Eds*, pp 117-128, 2001
 - [58] G D Hines, Z Rahman D J Jobson, and G A Wodell, "Single-Scale Retinex Using Digital Signal Processors" *In Proceedings Of The GSPX*, 2004
 - [59] E Land, "An Alternative Technique For The Computation of The Designator in The Retinex Theory of Color Vision," *Proc Of The National Academy Of Science USA*, Vol 83, pp 2078-3080, 1986

- [60] L. Tao, "An Adaptive And Integrated Neighborhood Dependent Approach For Nonlinear Enhancement Of Color Images," *SPIE Journal of Electronic Imaging*, pp 11-114, 2005
- [61] A. C. Hulbert, "The Computation of Color," *Ph D Dissertaion, Mass Inst Techol, Cambridge, MA*, Sept 1989
- [62] Z. Rahman, "The Lectures Notes Of Image Processing," *Old Dominion University*, 2009
- [63] K. V. Velde, "Multi-Scale Color Image Enhancement," *In Proc Int Conf Image Processing*, pp 584-587, 1999
- [64] T. Reeves and M. Jernigan, "Multiscale-Based Image Enhancement," *Canadian Conf On Elect And Comp Engineering*, pp 500-505, 1997
- [65] B. Peng, W. Fu, And C. Yang, "Contrast Enhancement Of Radiographs Using Shift Invariant Wavelet Transform," *Wuhan Uni J Of Nat Sciences*, Pp 59-62, 2000
- [66] K. P. Ramesh, S. Gupta, E. P. Blasch,
[Http //Www Isif Org/Fusion/Proceedings/Fusion07cd/Fusion07/Pdfs/Fusion2007_1428 Pdf](http://www.isif.org/Fusion/Proceedings/Fusion07cd/Fusion07/Pdfs/Fusion2007_1428.pdf), accessed on January 2010
- [67] T. A. Wilson, and S. K. Rogers, "Perceptual-Based Image Fusion for Hyperspectral Data," *IEEE Trans Ge Remote Sensing*, Vol 35, pp 1007–1017, July 1997
- [68] G. Simone and A. Farina, "Image Fusion Techniques for Remote Sensing Applications," *Inform Fusion*, Vol 3, pp 3–15, 2002
- [69] C. S. Pattichis and M. S. Pattichis, "Medical Imaging Fusion Applications— An Overview," *In Conf Rec Asilomar Conf Signals, Systems Computers*, Vol 2, pp 1263–1267, 2001

- [70] S G Nikolov, And D R Bull, "Image Fusion Using A 3-D Wavelet Transform,"
In Inst Elect Eng Conf Pub , Vol 1, Pp 235–239, 1999
- [71] A Das and M Bhattacharya, "Evolutionary Algorithm based Automated Medical
Image Fusion Technique Comparative Study With Fuzzy Fusion Approach,"
*Proceedings of The World Congress on Nature & Biologically Inspired
Computing*, pp 269-274, 2009
- [72] B V Dasarathy, "Image Fusion in the Context Of Aerospace Applications,"
Inform Fusion, Vol 3, 2002
- [73] D M Jasiunas, A D Kearney, John Hopf, and Grant B Wigley,
"Http //Www Cis Unisa Edu Au/~Cisjph/31_Jasiunas Pdf", accessed on January
2010
- [74] H Singh, J Raj, G Kaur, and T Meitzler, "Image Fusion using Fuzzy Logic
and Applications," *Fuzzy Systems, Proceedings IEEE International Conference*,
Vol 1, pp 337 – 340, 2004
- [75] J J Lewis, R J O'callaghan, S G Nikolov, D R Bull, and C N
Canagarajah, "Http //Www Google Com Tr/Search?Hl=Tr&Source=Hp&Q=Regi
on+Based+Image+Fusion+Using+Complex+Wavelets&Aq=F&AqI=&AqI=&Oq
=&Gs_Rfal" accessed on January 2011

VITA

NAME	Sertan Erkanlı
DATE OF BIRTH	May 5, 1973
DEGREES	Bachelor of Science (Electrical and Electronics Engineering), Turkish Air Force Academy, Istanbul, Turkey, August 1995 Master of Science (Electrical and Electronics Engineering), Turkish Air Force Academy, Istanbul, Turkey, August 2003 Doctor of Philosophy (Electrical and Computer Engineering), Old Dominion University, Norfolk, Virginia, May 2011
EMPLOYMENT	Officer in Turkish Air Force, August 1995 to present